

Technische Universität München
Institut für Energietechnik

Lehrstuhl für Thermodynamik

Influence of Burner-Burner Interactions on the Flame Dynamics in an Annular Combustor

Dan Fanaca

Vollständiger Abdruck der von der Fakultät für Maschinenwesen der
Technischen Universität München zur Erlangung des akademischen Grades
eines

DOKTOR – INGENIEURS

genehmigten Dissertation.

Vorsitzende:

Univ.-Prof. Kristina Shea, Ph.D.

Prüfer der Dissertation:

1. Univ.-Prof. Dr.-Ing. Thomas Sattelmayer
2. Univ.-Prof. Dr.-Ing., Dr.-Ing. habil., Dr. h.c. Rudolf Schilling

Die Dissertation wurde am 16.11.2009 bei der Technischen Universität München eingereicht
und durch die Fakultät für Maschinenwesen am 15.03.2010 angenommen.

Acknowledgement

The research work presented in this thesis was accomplished at Lehrstuhl für Thermodynamik of Technische Universität München in the framework of the KW21 Project (Phase I).

First of all, I am especially thankful to my Ph.D. supervisor, Prof. Dr.-Ing. Thomas Sattelmayer, for giving me the opportunity to work and study at Lehrstuhl für Thermodynamik. His close support represented a guideline throughout the course of my work and his valuable experience in the complex field of combustion, combined with an open and at the same time critical attitude with respect to my research activities, stimulated me to learn and to develop my knowledge continuously.

I would like to thank Prof. Dr.-Ing. habil. Rudolf Schilling for his interest in my work and for assuming the position of co-examiner of the thesis. Furthermore, I would like to thank Prof. Dr. Kristina Shea for organising the examination process and accepting the invitation to take the chair of the examination committee.

My sincere thanks go to Dr.-Ing. Christoph Hirsch. His dedication and extensive know-how on technical matters have represented a valuable support and the friendly discussions were a constant encouragement and motivation in times of difficulty.

Hereby, I would like to mention especially my office and project colleague Reddy Alemela. Together we have experienced the ups and downs of our project, from the experimental activity in the lab to the yearly project workshops and conferences. I remain thankful to him for the friendly and warm atmosphere with interesting discussions on professional as well as non-professional subjects. The time at the chair remains a precious memory for me which I recall time and time again with pleasure. For this I would like to

thank all my actual and former colleagues for the interesting moments spent together at the daily lunch breaks, sport activities and on many other occasions.

Special thanks to Mrs. Bassett and Mrs. Schulz-Reichwald for their support on administrative and financial issues. I would also like to express my sincere thanks to the mechanical and electrical workshops under the coordination of Erich Sieber and Bernhard Strobl. Without their help and especially without the help of Claus Wimmer and Gerhard Giel, this experimental work would have been much more difficult. The activity in the lab was sustained also by highly motivated and hard-working students to whom I am very grateful.

Finally, I wish to thank my parents. All this wouldn't have been possible at all without their moral and financial support. You have sustained me unconditionally during my studies in Romania and Germany. For this I thank you with all my heart and I dedicate this work to you.

München, in March 2010

Dan Fanaca

Abstract

This thesis compares the dynamic characteristics of lean premixed turbulent swirl flames as found in single burner test configurations with those of the typical multi-burner configurations used in industrial gas turbines. For this, the burner transfer matrix (BTM) and the flame transfer function (FTF) of a lean premixed swirl burner are determined in an annular combustor chamber using a newly developed methodology called the model based regression method.

In this method an acoustic network model is used to represent the acoustic behaviour of the annular combustor test rig. This model provides solutions of the acoustic pressure field which are functions of a restricted set of physically motivated, albeit initially unknown parameters. The actual parameter values are determined from regression analysis of the experimental acoustic pressure data. In the model the elements of the annular combustor test rig, like the flames, the burners and the annular combustion chamber are represented acoustically with their transfer matrices. In particular, the burner is modelled with a global compact element with acoustic losses and an effective length and the flame is represented with a time-lag model which assumes an axial distribution of the heat release. The acoustic losses at the system boundaries are considered in the acoustic network model such that for the downstream acoustic boundary the measured reflection coefficient of the exit nozzle is implemented. A sensitivity study shows that the chosen parameters have a strong influence on the quality function of the regression, i.e. the calculated acoustic pressure field, which indicates the robustness of the method.

The results show that the network model can calculate the acoustic behaviour of the annular combustor test rig for all oscillation modes. It is found that the

classical time-lag model represents well the dynamic behaviour of the flame in the annular combustor where both, axial and azimuthal modes oscillate.

The direct comparison with the data obtained in the single burner combustion chamber shows that the BTM is very similar in the two combustor configurations. It is found that the FTF is different having longer convective time delays in the annular combustor than in the single burner case, which is consistent with the static flame characteristics observed in both systems. The cause for these differences is found in the strong deviations in the flow fields: in the single burner combustor the expanding swirl flow attaches to the walls whereas this effect does not occur in the annular combustion chamber. Based on these results, a new theory for the design of the single burner experiments is proposed, such that the flow field resembles that of the annular combustion chamber and thereby, the FTF is similar in the two combustor configurations.

Zusammenfassung

Diese Arbeit untersucht, wie sich die dynamischen Eigenschaften von gasturbinentypischen turbulenten Drallvormischflammen in Testkonfigurationen (Einzelbrenner) von denen in maschinentypischen Mehrbrennerkonfigurationen unterscheiden. Dazu werden die Brennertransfermatrix (BTM) und die Flammentransferfunktion (FTF) eines vorgemischten Drallbrenners in einer Ringbrennkammer mit einer neu entwickelten Methodik bestimmt, die als Modellbasierte Regression bezeichnet wird.

Bei dieser Methode wird ein Netzwerkmodell entwickelt und angewendet, um das akustische Verhalten des Ringbrennkammerversuchsstandes zu simulieren. Dieses Modell berechnet das akustische Feld im Prüfstand als Funktion einer kleinen Anzahl physikalisch motivierter Parameter, die zunächst unbekannt sind. Die Parameterwerte werden durch Regression der Modelldaten auf die experimentell gemessenen Druckdaten bestimmt. Im Modell werden die verschiedenen Elemente des Ringbrennkammerversuchsstandes, wie die Brenner, die Flammen und die Ringbrennkammer mittels ihrer Transfermatrix dargestellt. Die Brenner werden hierbei durch ein globales Druckverlust-Element mit effektiver Länge modelliert. Die Flammen werden mit einem Zeitverzugsmodell abgebildet, bei welchem eine axiale Verteilung der Wärmefreisetzung angenommen wird. Um die akustischen Verluste über die Systemgrenze zu berücksichtigen, wird für die Randbedingung stromab der Brennkammer der gemessene Reflektionsfaktor der Austrittsdüse implementiert. Eine Sensitivitätsstudie zeigt den starken Einfluss der gewählten Parameter auf die Qualitätsfunktion der Regression, das heißt die berechneten dynamischen Drücke, wodurch die Robustheit des Verfahrens belegt wird.

Die Ergebnisse zeigen, dass das Netzwerkmodell in der Lage ist das akustische Verhalten der Ringbrennkammer für alle Modalkomponenten zu simulieren. Es zeigt sich, dass das klassische Zeitverzugsmodell das dynamische Flammenverhalten auch im Fall der axial und azimuthal schwingenden Ringbrennkammer darstellen kann.

Der direkte Vergleich mit den Ergebnissen aus der Einzelbrennerkonfiguration zeigt, dass die BTM in den beiden Einbausituationen sehr ähnlich ist. Es ergibt sich, dass die FTF der Ringbrennkammer sich mit längeren konvektiven Zeitverzügen von den Werten der Einzelbrennkammer unterscheidet, was auch mit den statischen Eigenschaften der Flamme übereinstimmt. Der Grund für diese Unterschiede liegt in den großen Abweichungen der beiden Strömungsfelder: In der Einzelbrennkammer legt sich der aufplatzende Drallstrahl an die Brennkammerwände an, während dieser Effekt in der Ringbrennkammer nicht auftritt. Anhand dieser Ergebnisse wird eine neue Theorie für die Gestaltung der Einzelbrennerversuche vorgeschlagen, damit das Strömungsfeld im Einzelbrennertest dem in der Ringbrennkammer ähnlich ist und somit die FTF in den beiden Brennerkonfigurationen gleich ist.

Contents

1	Introduction	1
2	Combustion Instabilities	3
3	Goal and Outline	10
4	Experimental Set-up and Measurement Techniques	12
4.1	Annular Combustion Chamber	14
4.2	Air Preheater Unit	16
4.3	Measurement Techniques	18
4.3.1	Acoustic Pressure	18
4.3.2	Optical Measurements	24
5	Acoustics Theory	26
5.1	Linearised Euler Equations	26
5.2	Acoustic Wave Equation	28
5.3	Harmonic Oscillations	30
5.3.1	Helmholtz Equation	30
5.3.2	Acoustic Waves in Longitudinal 1D Ducts	31
5.3.3	Acoustic Intensity, Energy, Impedance, Admittance and Reflection	32
5.3.4	Acoustic Waves in Thin Annular Ducts	34
5.3.5	Eigenfrequencies of Thin Annular Ducts	43
5.4	Acoustic Damping	44
5.4.1	Visco-Thermal Damping in Boundary Layers	44
5.4.2	Flow Induced Damping	46

6	Acoustic Two Port Elements	48
6.1	Equivalent Forms of Acoustic Two Port Matrices	50
6.2	Direct Experimental Evaluation	52
6.3	Analytical Transfer Matrices	54
6.3.1	Duct with Constant Cross-Section	54
6.3.2	Compact Element with Losses	56
6.3.3	Premixed Flames	57
6.3.4	Acoustic Uncoupling Element	61
6.3.5	Acoustic Junction Element	64
7	Method Development	66
7.1	Modal Decomposition Method	67
7.2	Acoustic Network Model of the Annular Combustor	72
8	Determination of the BTM and FTF	79
8.1	Acoustic Measurements with the Isothermal Flow	79
8.2	Model Based Analysis of the Cold Acoustic Measurements	88
8.3	Determination of the FTF	94
8.3.1	Perfectly Premixed Mode Operation (PPM)	95
8.3.2	Injector Premixed Mode Operation (IPM)	102
8.3.3	Conclusions and Discussions	108
8.3.4	Comparison of the BTM and FTF between SCC and ACC	113
8.4	Sensitivity Analysis of the Acoustic Network Model	116
9	Flow Field Investigations and Critical Confinement Theory	121
9.1	Experimental Set-up	121
9.2	Results	123
9.3	Critical Confinement Theory	127
9.4	Conclusions	134
10	Summary	135

List of Figures

4.1	Schematic representation of the annular combustor test rig . . .	13
4.2	Annular combustion chamber	14
4.3	Measurement ports for the acoustic pressure in the ACC	15
4.4	Air preheater unit	16
4.5	Cross section through the air preheater unit	17
4.6	Dynamic pressure transducer Type 106B. a) Sensor and cooling adapter. b) Sensor, cooling and mounting adapter	19
4.7	Dynamic pressure sensor mounted on the combustor wall: a) actual configuration and b) schematic representation	20
4.8	Schematic representation of the calibration set-up for the dynamic pressure transducers	21
4.9	Calibration curves from one sensor with respect to the reference for different design configurations of the mounting adapter . . .	22
4.10	Schematic representation of the Helmholtz resonator in the mounting adapter	22
4.11	Transmission spectrum of the UV band pass filter UG11	24
4.12	Schematic representation of the averaging procedure for the determination of the OH*-Chemiluminescence distribution	25
5.1	1D wave propagation in the presence of a mean axial flow (\bar{u}) . .	31
5.2	2D acoustic field in an annular duct	35
5.3	Schematic representation of the wave propagation in a 2D acoustic field, the global wavenumber k is perpendicular on the wave front. a) triangle of wavenumbers; b) triangle of acoustic velocities	36
5.4	Modal components as a function of the azimuthal mode index m and the axial wavenumber k_x	37

5.5	Schematic representation of a 1 st order standing azimuthal mode ($m=1$) at phase 0 (a), $\pi/2$ (b), π (c) and $3\pi/2$ (d). Notation: + and - are antinodes in π phase delay and 0 the nodes	40
5.6	Schematic representation of a 1 st order spinning azimuthal mode ($m=1$) at phase 0 (a), $\pi/2$ (b), π (c) and $3\pi/2$ (d). Notation: + and - are antinodes in π phase delay and 0 the nodes	41
5.7	Flow induced acoustic dissipation in the regions of vorticity generation at an area expansion	46
6.1	Schematic representation of a two port element	49
6.2	Schematic representation of an acoustic two port of an 1D duct. Indices u and d denote the upstream and downstream sides of the duct respectively	50
6.3	Schematic representation of an acoustic two port of a thin annular duct. Indices u and d denote the upstream and downstream sides of the duct respectively	50
6.4	Schematic representation of the experimental set-up of the <i>two source location method</i> for a 1D duct with a mean flow of velocity \bar{u} . Superscripts a and b denote the two acoustic states generated by switching the position of the sound source between the upstream and downstream sides of the test element	53
6.5	Schematic representation of a generic duct of length L and constant cross-section; u and d denote the axial positions of the upstream and downstream reference planes respectively	55
6.6	Schematic representation of a flame as a flow discontinuity with heat input Q	57
6.7	The uncoupling element describes the transition from the 2D acoustic field of the annular plenum chamber to 1D acoustic field of the burner and the transition from the 1D acoustic field of the burner section to the 2D acoustic field of the annular combustion chamber	62
6.8	Schematic representation of the acoustic junction element; u denotes the upstream side and $d1, d2$ the downstream branches	64

7.1	Schematic representation of the experimental set-up for the acoustic pressure measurement: dynamic pressure transducers mounted on the outer combustor wall at one axial position x_0 and different circumferential coordinates y	70
7.2	Schematic representation of the acoustic network model of the ACC	74
7.3	Measured reflection coefficient of the exit nozzle	78
8.1	Frequency response function of the measured acoustic response under axial excitation	81
8.2	Frequency response function of the measured acoustic response under 1 st order standing azimuthal excitation	82
8.3	Weighted spin-ratios Δ_{sp}^1 , Δ_{sp}^2 and Δ_{sp}^3 for axial (a,c,e) and 1 st order standing azimuthal (b,d,f) excitation	83
8.4	Error of the modal analysis procedure for axial (left) and 1 st order standing azimuthal (right) excitation	84
8.5	Υ_0 for axial (left) and 1 st order azimuthal (right) excitation	85
8.6	Υ_1 for axial (left) and 1 st order azimuthal excitation (right)	86
8.7	Υ_2 for axial (left) and 1 st order azimuthal excitation (right)	87
8.8	Relative amplitude of the measured (Dec.) and simulated (Sim.) axial (left) and 1 st order azimuthal (right) components in the plenum with respect to the combustion chamber	91
8.9	Azimuthal distribution of \hat{p} for the decomposed (Dec. a_0) and simulated (Sim. $m = 0$) axial modes in the combustion chamber (left) and plenum (right) at 130 Hz. Additionally, data (Exp.) measured at 130 Hz is plotted	93
8.10	Azimuthal distribution of \hat{p} for the decomposed (Dec. a_1) and simulated (Sim. $m = 1$) 1 st order azimuthal modes in the combustion chamber (left) and plenum (right) at 260 Hz. Additionally, data (Exp.) measured at 260 Hz is plotted	94
8.11	Frequency response function of the measured acoustic pressure \hat{p} in the combustion chamber and plenum in the PPM under axial excitation	96
8.12	Modal decomposition in the combustion chamber for the PPM	97

8.13	Relative amplitude of the measured (Dec.) and simulated (Sim.) axial (left) and 1 st order azimuthal (right) components in the plenum with respect to the combustion chamber for the PPM	100
8.14	Azimuthal distribution of \hat{p} for the decomposed (Dec. a_0) and simulated (Sim. $m = 0$) axial modes in the combustion chamber (left) and plenum (right) at the frequency of 150 Hz. Additionally, data (Exp.) measured at 150 Hz is plotted	101
8.15	Azimuthal distribution of \hat{p} for the decomposed (Dec. a_1) and simulated (Sim. $m = 1$) 1 st order azimuthal modes in the combustion chamber (left) and plenum (right) at the frequency of 570 Hz. Additionally, data (Exp.) measured at 570 Hz is plotted	102
8.16	Frequency response function of the measured \hat{p} in the combustion chamber and plenum in the IPM under axial excitation	103
8.17	Modal decomposition in the combustion chamber for the IPM	104
8.18	Relative amplitude of the measured (Dec.) and simulated (Sim.) axial (left) and 1 st order azimuthal (right) components in the plenum with respect to the combustion chamber for the IPM	106
8.19	Azimuthal distribution of \hat{p} for the decomposed (Dec. a_0) and simulated (Sim. $m = 0$) axial modes in the combustion chamber (left) and plenum (right) at the frequency of 300 Hz. Additionally, data (Exp.) measured at 300 Hz is plotted	107
8.20	Azimuthal distribution of \hat{p} for the decomposed (Dec. a_1) and simulated 1 st order azimuthal (Sim. $m = 1$) modes in the combustion chamber (left) and plenum (right) at the frequency of 570 Hz. Additionally, data (Exp.) measured at 570 Hz is plotted	108
8.21	Left: time averaged distribution of the OH*-Chemiluminescence in the PPM. Right: PDF of the OH*-Chemiluminescence distribution and of the normal distribution σ in the PPM	110
8.22	Left: time averaged distribution of the OH*-Chemiluminescence in the PPM. Right: time averaged distribution of the OH*-Chemiluminescence in the IPM	111
8.23	Time averaged OH*-Chemiluminescence in the ACC (left) and SCC (right) without forcing in the PPM	115

8.24	Simulation results for the axial (left) and 1 st order azimuthal (right) components for the variation of the pressure loss coefficient ζ	117
8.25	Simulation results for the axial (left) and 1 st order azimuthal (right) components for the variation of the effective length l_{eff} .	118
8.26	Simulation results for the axial (left) and 1 st order azimuthal (right) components for the variation of the mean convective time delay τ	119
8.27	Simulation results for the axial (left) and 1 st order azimuthal (right) components for the variation of the normal distribution σ	120
9.1	Schematic representation of the PIV set-up in the ACC	122
9.2	Schematic representation of the PIV set-up in the SCC	123
9.3	Time averaged absolute (arrows) and axial (colour) velocities in the ACC (left) for the isothermal flow. Right: contour plot of the axial velocity u with the isoline corresponding to the value zero	124
9.4	Time averaged absolute (arrows) and axial (colour) velocities in the SCC (left) for the isothermal flow. Right: contour plot of the axial velocity u with the isoline corresponding to the value zero	125
9.5	Time averaged absolute (arrows) and axial (colour) velocities in the ACC (left) for the case with combustion. Right: contour plot of the axial velocity u with the isoline corresponding to the value zero	126
9.6	Schematic of jet swirl balance	130
9.7	Comparison of confinement theory with experimental data from various burner configurations in the SCC and ACC	132
9.8	Time averaged OH*-Chemiluminescence distribution with the TD1-321608 burner in the PPM in the ACC (left) and SCC (right)	133

List of Tables

4.1	Technical characteristics of the dynamic pressure transducer Type 106B (PCB Piezotronics)	18
5.1	Eigenfrequencies of the isothermal annular duct	43
8.1	Operating parameters and excitation modes for the cold acoustic measurements	80
8.2	Simulation parameters for the cold acoustic measurements . . .	89
8.3	Operating parameters of the annular combustor in the PPM . .	95
8.4	Simulation parameters for the PPM	99
8.5	Operating parameters of the annular combustor in the IPM . . .	103
8.6	Simulation parameters for the IPM	105
8.7	Burner and flame parameters for PPM and IPM	109
8.8	Flame parameters and X_{OHmax} in the SCC and ACC for PPM . .	113

Nomenclature

Latin letters

A	Cross-sectional area [m ²]
A_b	Nominal cross-sectional area of the burner [m ²]
A_{cc}	Cross-sectional area of the annular combustion chamber [m ²]
A_{pl}	Cross-sectional area of the annular plenum chamber [m ²]
a_0	Complex amplitude of the axial component [Pa]
a_k	Complex amplitude of the k th order standing azimuthal mode [Pa]
$a_{k\pm}$	Complex amplitude of the k th order spinning azimuthal mode [Pa]
C_{crit}	Model constant of the critical confinement theory [-]
c	Speed of sound [m/s]
D, d	Diameter [mm]
D_{cc}	Mean diameter of the annular combustion chamber [mm]
D_{pl}	Mean diameter of the annular plenum chamber [mm]
d_0	Nominal burner diameter [mm]
d_h	Hydraulic diameter [mm]
e	Error factor of the modal decomposition method [%]
e_{ac}	Specific acoustic energy [J/m ³]
F	Wave propagating downstream in a thin annular duct [m/s]
f_c	Cut-off frequency [Hz]
f	Frequency [Hz]
f	Riemann invariant propagating in the downstream direction [m/s]
G	Waves propagating upstream in a thin annular duct [m/s]
g	Riemann invariant propagating in the upstream direction [m/s]
H	Two port transfer function
h	Width of an annular duct [mm]

h_{cc}	Width of the annular combustion chamber [mm]
h_{pl}	Width of the annular plenum chamber [mm]
i	Imaginary unit $i^2=-1$ [-]
i_{ac}	Acoustic intensity [W/m^2]
k	Global wavenumber [$1/m$]
k_x^\pm	Axial wavenumber [$1/m$]
k_y^\pm	Circumferential wavenumber [$1/m$]
L	Length [mm]
L_{cc}	Length of the annular combustion chamber [mm]
L_{pl}	Length of the annular plenum chamber [mm]
L_f	Flame length [mm]
l	Axial mode index [-]
l_{red}	Reduced length [m]
l_{eff}	Effective length [m]
M	Mach number [-]
m	Azimuthal mode index [-]
\dot{m}	Mass flow rate [kg/s]
n	Interaction index [-]
n_c	Correction factor for the interaction index [-]
P_{th}	Thermal power [kW]
p	Pressure [Pa]
Pr	Prandtl number [-]
Q	Heat release [W]
q	Specific heat release [W/m^2]
R	Radius [mm]
$R_{\pm\pm}$	Complex modal amplitudes of the helical waves $r_{\pm\pm}$ [m/s]
R_i	Inner radius of the annulus [mm]
R_o	Outer radius of the annulus [mm]
R_m	Mean radius of the annulus [mm]
r	Acoustic reflection coefficient [-]
$r_{\pm\pm}$	Helical waves in a thin annular duct [m/s]
Sh	Shear number [-]
s_i	Specific angular momentum of flux i [m^2/s]
S_{eff}	Swirl number of the burner flow [-]

NOMENCLATURE

S_r	Swirl number of the recirculated flow [-]
T	Temperature [K]
T_{ad}	Adiabatic flame temperature [K]
T_c	Temperature upstream of the flame [K]
T_h	Temperature downstream of the flame [K]
T_{pl}	Preheating temperature in the plenum [K]
T_{fg}	Transfer matrix in fg notation
T_{pu}	Transfer matrix in pu notation
t	Time coordinate [s]
u	Axial velocity [m/s]
u_0	Nominal burner velocity [m/s]
v	Azimuthal velocity [m/s]
X_{OHmax}	Axial coordinate of the OH*-Chemiluminescence maximum [mm]
x	Cartesian axial coordinate [mm]
y	Cartesian circumferential coordinate [mm]
y_0	Radial burner coordinate [mm]
Z	Acoustic impedance [kg/(m ² s)]

Greek letters

α	Damping coefficient [1/m]
β	Ratio of specific impedances [-]
γ	Ratio of specific heats [-]
Δ_{sp}^k	Spin ratio of the azimuthal mode k [-]
ζ	Pressure loss coefficient [-]
θ	Azimuthal angle [deg]
θ_k	Azimuthal angle of the standing azimuthal mode k [deg]
κ_u	Inclination of the wavefront with respect to the x-axis [-]
κ_v	Inclination of the wavefront with respect to the y-axis [-]
λ	Air excess ratio [-]
ν	Kinematic viscosity [m ² /s]
ρ	Density [kg/m ³]
σ	Normal distribution of the mean convective time delay τ [ms]
σ_ϕ	Normal distribution of the mean convective time delay τ_ϕ [ms]

τ	Mean convective time delay of the flow rate fluctuations [ms]
τ_ϕ	Mean conv. time delay of the equivalence ratio fluctuations [ms]
Y_k	Relative contribution of the mode k to the total signal power [-]
ϕ	Equivalence ratio [-]
ω	Angular frequency [rad/s]

Abbreviations

<i>1D</i>	One dimensional
<i>2D</i>	Two dimensional
<i>3D</i>	Three dimensional
<i>ACC</i>	Annular combustion chamber
<i>AMF</i>	Combustion air mass flow rate
<i>BC</i>	Acoustic boundary condition
<i>BFTM</i>	Burner and flame transfer matrix
<i>BTM</i>	Burner transfer matrix
<i>CCS</i>	Carbon capture and storage
<i>CFD</i>	Computational fluid dynamics
<i>CTA</i>	Constant temperature anemometer
<i>FRF</i>	Frequency response function
<i>FTF</i>	Flame transfer function
<i>FTM</i>	Flame transfer matrix
<i>IPM</i>	Injector premixed mode
<i>IRZ</i>	Inner recirculation zone
<i>LBO</i>	Lean blow out limit
<i>MMM</i>	Multi microphone method
<i>ORZ</i>	Outer recirculation zone
<i>PDF</i>	Probability density function
<i>PPM</i>	Perfectly premixed mode
<i>SCC</i>	Single burner combustion chamber

Subscripts

0	Nominal burner quantity
b	Burner
c	Upstream of the flame
cc	Combustion chamber
d	Downstream
eff	Effective
h	Downstream of the flame
pl	Plenum
r	Recirc. mass flow, specific angular mom. of the entrained flow
ref	Reference
s	Annular side mass flow and specific angular momentum
sp	Spinning component
u	Upstream
x	Mass flow and spec. angular mom. transferred to the ORZ
$+$	Downstream and clockwise directions of propagation
$-$	Upstream and anticlockwise directions of propagation

Superscripts

'	Acoustic fluctuation in time domain
-	Mean quantity
^	Complex amplitude

1 Introduction

The environmental pollution of the fossil fuel based energy production sector has become a serious concern since the 1970s. As a result central governments have introduced regulations which impose limits on the levels of pollutant emissions elements like NO_x and CO. These regulations have become more restrictive with time. In the USA for example, in 1977 the limits for NO_x were at 75 ppmv at 15% O_2 . Today, NETL (National Energy Technology Laboratory) has proposed as environmental target for NO_x a limit of 2.5 ppmv at 15% O_2 in combination with a SCR technique (selective catalytic reduction). To comply with this, the gas turbine was subjected to a continuous development whose outcome was the DRY LOW NOX combustion technology. One typical configuration used today is the annular combustion chamber with lean premixed swirl stabilized burners. A detailed development path which leads to this is presented in [15].

Unfortunately, industrial practice has shown that this technology is sensitive to self sustained combustion instabilities. These disturb the normal operation of the gas turbine by exposing the hardware components to additional unsteady mechanical and thermal loads. An additional effect is the decrease in efficiency and increase in the pollutant emissions, which represents a great cause of concern for the power plant operators and gas turbine manufacturers. Combustion instabilities are complex phenomena appearing as a result of the interaction between the flame providing the energy for sustaining the instabilities and the complex acoustics of modern gas turbine combustion systems. In order to understand and overcome these undesired phenomena, a more detailed look into the dynamic characteristics of lean premixed turbulent flames is necessary.

The dynamic characteristics of lean premixed flames are determined by measuring the FTF and FTM. The standard approach used today is to measure the

FTF and FTM on scaled down single burner combustor test rigs in order to reduce costs as well as measurement effort. Then, the results are transferred to multi burner configurations and used in simulation codes to analyse the stability of complex industrial combustion systems. Hereby, the transfer of results from the single to the multi burner combustor is made with the assumption of similarity between the two burner configurations. A major drawback of this approach is that important effects, which are specific for a multi burner configuration, like the 3D acoustic field and the burner-burner interaction cannot be reproduced in a single burner combustion chamber. Therefore, more insight in the dynamic characteristics of flames in multi burner configurations like an annular combustion chamber is needed. In particular, the direct comparison between the single and the multi burner annular configurations would allow a quantitative assessment of the differences and similarities and hence address the assumption of similarity.

2 Combustion Instabilities

Lean premixed combustion has been employed in the past 30 years as standard technology for fossil fuel based energy production due to its high potential in reducing the NO_x pollutant emissions. Unfortunately, in industrial practice this has proven less reliable than non-premixed combustion because of its high sensitive to self sustained combustion instabilities, which disturb the normal operation and can, in worst cases, produce extensive hardware damage to the system. Even though the basic physical mechanism was described as early as in the 19th century by Lord Rayleigh [51], the phenomenon of combustion instabilities occurring in lean premixed gas turbine combustion system is still lacking in knowledge and understanding. The triggering effect consists mainly in the complex interaction between the combustion process and the 3D acoustic system of the gas turbine. The presence of combustion instabilities in industrial gas turbine was reported frequently in literature.

Krüger et al. [32] report on unstable azimuthal modes in an annular combustor from the SIEMENS 3A Series of gas turbines equipped with 24 lean premixed hybrid burners. The frequencies measured in the engine lie at 170-180 Hz and 350 Hz. In [10] and [11] Bellucci et al. also write on combustion driven pulsations in a GT11N2 silo combustor from ALSTOM equipped with the EV17i lean premixed burners. Furthermore, they report in [9] on combustion instabilities in an ALSTOM silo combustor with a single partially lean premixed burner (LEV).

From the reports presented above it can be concluded clearly that combustion instabilities represent a major limitation factor for the operation of lean premixed industrial gas turbines and are therefore a great cause of concern for the gas turbine manufacturers. As a consequence a series of research and development programs dedicated to investigate the fundamental mechanisms which govern the development of self sustained combustion instabilities were

initiated in order to find solutions for improving the reliability of the engines. In the early stages of these efforts, the technical solutions consisted in modifying physically the actual combustors or in the on-line modulation of the fuel flow in order to suppress the acoustic oscillations. These solutions can be classified as passive and active means, respectively.

Bellucci et al. [10] have reported on using Helmholtz resonators as a passive mean for damping the combustion driven pressure pulsations in an ALSTOM GT11N2 silo gas turbine. An analytical non-linear thermo-acoustic model was proposed and used to determine the damper impedance. This was then implemented in a finite element model of the combustor as a frequency dependent boundary condition. Hence, the dynamic behaviour of the combustor-resonator system was investigated and the damping effect was optimised by tuning the Helmholtz resonator to the frequency of the instability. The improvement in the stability behaviour predicted by the finite element simulations was confirmed in the field tests.

Later, in a similar work, Bellucci et al. [11] have presented a different approach to investigate the dynamic behaviour of an industrial combustion system. They employed the acoustic network modelling method for optimising the damping effect of the combustor equipped with Helmholtz resonators. In the acoustic network, the burner was modelled as compact element with losses and the flame as an acoustic discontinuity with a classical time-lag model. The free parameters of the burner and flame were determined with help of numerical and experimental investigations. For the flame, the experimental data was measured on a single burner combustion chamber under atmospheric conditions and the transfer of the results to the multi burner configuration was made with the assumption of similarity between the two burner configurations.

The change to the acoustic network modelling method in [11] was motivated by a series of advantages which this approach offers over the finite element method. The acoustic network modelling consists in discretising the combustion system in a network of interconnected elements; every element describes the dynamic behaviour of single hardware components like plenum, combustion chamber, burner and flame. The modular character allows using

different modelling techniques for the individual network components, which enhances the flexibility and promotes this approach as a more time efficient method than the finite element solution. For the acoustic network modelling, the focus point lies in the low frequency domain, where the geometrical dimensions of the hardware components are much smaller than the acoustical wavelengths. Thereby, the assumption of plane waves propagating through acoustically compact elements can be made and thus, the dynamic behaviour of every element can be modelled based on the acoustic two port theory and represented by 2x2 transfer matrices.

In earlier work Krüger et al. [32] have reported also on using the acoustic network modelling supported by numerical and experimental methods to investigate the dynamic behaviour of a heavy duty annular combustor gas turbine from the SIEMENS 3A Series. His model describes the acoustic perturbations based on the linear acoustic theory and includes the elements combustion chamber, flame, burner and the fuel supply system. The acoustic influence of the plenum was not taken in consideration; nevertheless, the upstream boundary condition was represented by the frequency dependent burner impedance. This had been previously measured on a single burner test rig. As a particularity, the model took in consideration the 2D character of the acoustic field in the annular combustor with the axial and azimuthal directions of propagation. Each modal component is represented by a separate array of network elements reflecting in detail the axial and circumferential configuration of the engine. These are fitted with the respective components of the flame response determined numerically with a CFD method.

In a work related closely to this, Krebs et al. [31] have derived a stability criterion based on the well known Rayleigh Criterion to study the dynamic behaviour of the same type of industrial gas turbine from SIEMENS. The relevant parameters were the mean convective time delay τ and frequency f and were combined in the formula $(\tau \cdot f)$. With f being the measured frequency of the instability, their efforts concentrated on modifying the convective time delay, i.e. the FTF, in order to satisfy the conditions for system stability. To determine the FTF, a finite element model of the combustion chamber was developed and validated with the experimentally measured FTF. Like in the case of [11],

the experimental determination of the FTF was made on a single burner combustion chamber [8] and the results were transferred to the annular combustion chamber with the assumption of similarity between the two burner configurations. The outcome of the study was the necessity to increase the time delay τ of the flame by a quarter of the period of oscillation in order to shift the operation of the gas turbine to a stable regime. Practically, this was achieved by mounting a cylindrical extension (CBO) on the burner nozzle. An additional modification was the tilting of the burner axis to the side by an angle of 10° to suppress the formation of coherent flow structures. These hardware modifications together with burner grouping were described in detail by Berenbrink et al. [12] and had the positive effect of damping the self sustained combustion instabilities such that these were not any more a limiting factor for the operation of the gas turbine. The optimal burner arrangement was on the contrary to what expected a non-symmetrical set-up. This solution was discovered, as the authors mentioned, based on experience and after extensive testing, as no theoretical tool for designing the burner arrangement was available.

Following these results, Evesque et al. [18] have developed a theoretical tool based on the acoustic network modelling method for studying the effect of a non-symmetrical burner arrangement on the dynamic behaviour of annular combustors. The acoustic network model of a generic annular combustor considered the 2D character of the acoustic field in a different way as in [32]. Thereby, the circumferential direction of propagation was described analytically under the assumption of standing azimuthal modes as in Stow et al. [58]. Thus, the model consisted of a 1D array of elements reflecting only the axial configuration of the combustion system. Although at this early stage the model did not include the flame response, the outcome of the study was encouraging regarding the potential of the method to predict the impact of non-symmetrical burner arrangements on the overall system stability. In the later stages of the work, presented in [17], the model included also the flame behaviour. This was modelled as a axially distributed reaction zone with a multi pole expansion technique after Lieuwen et al. [35]. As a difference with respect to the approach chosen in [32], the axial and azimuthal acoustic modal components were calculated only with the axial flame response.

In a more recent publication, Kopitz et al. [30] reported also on making stability analysis of an annular combustion chamber using the acoustic network modelling method. This work was backed up and validated against experimental results. The acoustic network model included the measured FTF. The results of the stability analysis computations were compared against the experimentally determined stability maps. The FTF was measured at one operating point for the lean premixed swirl stabilised TD1 burner in the annular combustor test rig at Lehrstuhl für Thermodynamic of TU München. The results were presented in detail in [34], [33] and [22]. For assessing the FTF at different operating points, scaling rules taken from Lohrmann et al. [36] were used. The success of the approach was limited as the acoustic network model reproduced only partially the experimentally determined stability maps. A reason for this outcome was thought to be the modelling of the dynamic behaviour of the flame. The FTF implemented was measured in the annular combustor test rig for an axial excitation. The authors argued that beside this, also the FTF under azimuthal forcing had to be experimentally determined and then implemented in the model in order to have a consistent modelling of all physical phenomena in a multi burner annular combustor.

In one of the most recent publications, Bellucci et al. [9] reported the successful application of the acoustic network modelling method in the so called *predictive mode*. Hereby, TA3 - the acoustic network modelling package from ALSTOM - was used in the design phase to analyse the stability behaviour of an existing silo combustor retrofitted with a single partially premixed burner (LEV) for reducing NO_x . For the model development, the BTM and FTF were determined solely by means of numerical simulations and no experimental investigations were made. The stability behaviour investigated with the acoustic network model agreed with the field tests made on the real engine. The convective time delay could be identified as tuning parameter with a great influence on the stability of the system. Hence, an optimal value was determined to ensure quiet operation and the system was designed accordingly. In practice, the optimal value for the convective time delay was implemented by moving axially the central lance of the burner to the desired position.

Even though the theoretical tools for investigating the dynamic behaviour of

multi burner combustion systems have evolved significantly in the last years, no general, universally applicable solution for designing acoustically stable lean premixed combustion systems is currently available. A major gap in the understanding concerns the static and dynamic characteristics of premixed flames in complex multi burner combustion systems. One important aspect to be addressed here is the influence of the 3D acoustic field on the dynamic flame behaviour since it is not clear whether the FTF has indeed a more complex character with axial and azimuthal components as postulated in [32]. This issue was also raised by Kopitz et al. [30] as a prerequisite for a better understanding of the dynamic behaviour of an annular combustor. A particularly important aspect is the assumption of similarity between the results from the single and the annular burner configuration made in [11] and [31]. To address this issue a qualitative and quantitative assessment of the differences and similarities between the flame characteristics in the single and the annular burner configurations is of great interest.

A direct comparison of the dynamic characteristics of a lean premixed flame in a single and an annular combustor was made by Kunze et al. [34]. They measured the FTF of the lean premixed swirl stabilised TD1 burner in the single and the annular combustor test rigs available at Lehrstuhl für Thermodynamik of TU München. Significant differences between the two burner configurations were observed and these were explained as a result of two major effects. The first effect was the influence of azimuthal modes on the flame dynamics and the second was the lower effective swirl number of the burner flow in the annular configuration. The azimuthal modes had a direct influence on the flame shape and therefore on the FTF. This was most obvious around the eigenfrequencies of the plenum chamber, where the FTF showed a clear peak. Thus, it was concluded that the FTF is influenced by the azimuthal modes and therefore, the assumption of similarity between the dynamic flame characteristics from the single and the annular burner configurations was not supported. The lower effective swirl number in the annular combustor was a result of the burner-burner interactions. The shear layers between the swirling flows of the neighbouring burners dissipate the angular momentum. As a result of this, the flames in the annular combustor were much longer than in the single burner test rig. This effect was amplified also because both combustors

were operated in cold non-preheated mode. The longer flames in the annular combustor were untypical for industrial gas turbines and therefore unsuitable for acoustic measurements for the determination of the FTF.

The results published in [34], [33] and [22] represented the starting point for the work presented in this thesis. The focus lay on the determination of the static and dynamic characteristics of a lean premixed swirl stabilised burner in preheated operation in an annular combustor test rig and the comparison with the results obtained, for the same operating conditions, in the single burner configuration. Further, a qualitative and quantitative assessment of the differences and similarities between the two combustor configurations could be made and the assumption of similarity addressed. These results are of great interest for industrial gas turbine manufacturers who determine the FTF of lean premixed flames in single burner combustor test rigs and then, based on the assumption of similarity, transfer the results to multi burner configurations for performing dynamic analysis.

3 Goal and Outline

The purpose of the work is the determination of the BTM and FTF of a lean premixed swirl stabilised burner in preheated operation in the ACC. An important aspect is here the comparison with the results obtained for the same operating conditions in the SCC in order to check the transferability of the dynamic flame characteristics between the two combustor configurations.

The annular combustor test rig available at Lehrstuhl für Thermodynamic of TU München is going to be presented in the following chapter. Then, a short introduction in the linear acoustic theory and in the acoustic network modelling follows. Chapter 7 presents the *model based method* used for the determination of the BTM and FTF in the ACC. Here is explained why this method was chosen and its advantages over the classical approaches are discussed.

The results of the experimental investigations for the determination of the BTM and FTF in the ACC are presented together with the respective analysis and comments in Chapter 8. In the Section 8.3.4 these are compared with the BTM and FTF obtained at the same operating conditions in the SCC. It was found that the FTF differs between the two combustor configurations mainly in the mean convective time delay, which are longer in the ACC. These results were confirmed by the optical flame characterisations which showed that the flame structures are different in the two combustor configurations with the zones of highest reactivity being in the ACC more downstream than in the SCC.

Chapter 9 presents the results of the flow field investigations. These were made to search for the aerodynamic characteristics of the flow in the two combustion chambers which produce the different FTF. The results show that the velocity profiles downstream of the burner are very different in the ACC and SCC, such that in the ACC a free jet regime and in the SCC a wall jet regime devel-

ops. These discrepancies are the main cause for the deviations in the FTF and consequently do not provide, in this particular case, a solid basis for the transferability of the FTF between the ACC and SCC. Furthermore, in Chapter 9 the physical mechanism behind these discrepancies is explained. Based on this and on earlier findings, a new theory is developed which proposes general design rules for single burner experiments such that the aerodynamic similarity to the annular multi burner configuration and thus the transferability of the FTF are improved.

4 Experimental Set-up and Measurement Techniques

The schematic representation of the annular combustor test rig is shown in Fig. 4.1. The air is supplied from the main supply line of the lab (12bar) which can provide a maximum mass flow of 4kg/s. After filtering, the main air mass flow is separated in the combustion air, the air directed to the sirens and the air used for the wall cooling. The combustion air is regulated by a calibrated thermal air mass flow controller before entering the preheater unit, which is described in detail in the Chapter 4.2. After being preheated at the desired temperature, the combustion air is equally distributed to the 12 premixers. The fuel (natural gas) is supplied from the main gas supply line of the lab (13bar) and is controlled by a thermal mass flow controller IN FLOW from BRONKHORST. Then, the fuel is equally distributed to the 12 premixers as well. Here, the reactant mixture is generated through high turbulence [54] for the perfectly premixed mode operation (PPM). Afterwards, the air-fuel mixture is provided to the annular combustion chamber. The annular combustion chamber is presented in detail in Chapter 4.1.

As seen in Fig. 4.1, the air-fuel mixture is generated in the PPM upstream of the combustor. The high efficiency of the 12 premixers ensures a homogeneous air-fuel mixture in the burner. The second operational mode of the EV5 burner is the injector premixed mode (IPM). Here, the fuel is supplied directly in the burner and the mixing process takes place in the swirl generator. The IPM resembles the real mixing conditions found in industrial gas turbines. Due to the short mixing distance, the IPM is characterised by fluctuations of the equivalence ratio, which are transported downstream to the flame with the mean flow velocity.

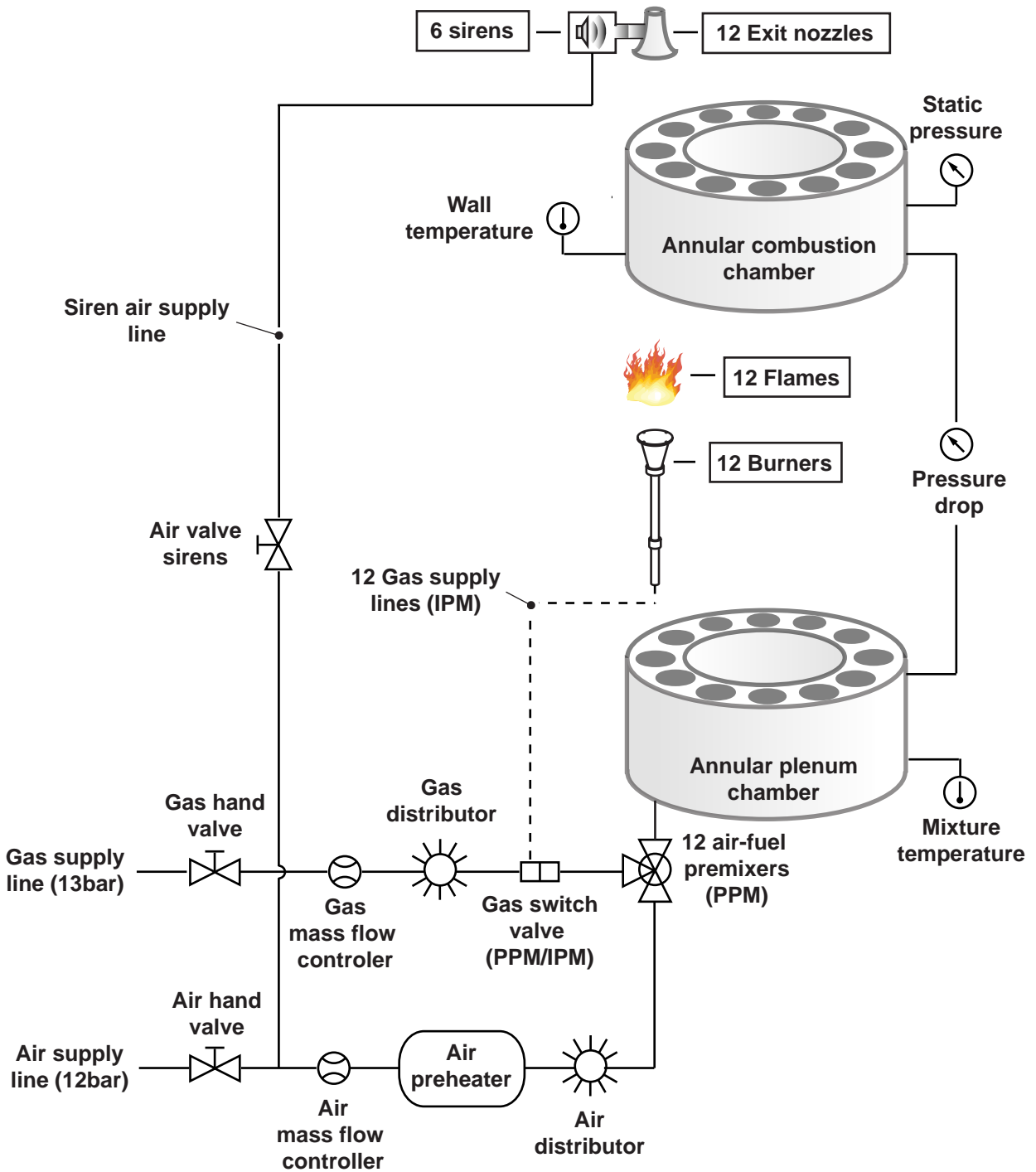


Figure 4.1: Schematic representation of the annular combustor test rig

4.1 Annular Combustion Chamber

The annular combustion chamber is shown in Fig. 4.2. The annular plenum has a width of $h_{pl} = 136\text{mm}$ and a mean diameter of $D_{pl} = 437\text{mm}$ at a length of $L_{pl} = 223\text{mm}$. The large area ratio between the plenum and the inlet pipes together with the large pressure drop over the premixers provide an acoustically hard boundary and thus constant equivalence ratio of the externally premixed flow. The annular combustion chamber can be seen above the plenum chamber. It has the dimensions $h_{cc}/D_{cc}/L_{cc} = 77\text{mm}/437\text{mm}/279\text{mm}$ and is equipped with two quartz glass windows which provide optical access for flame observations as well as for PIV measurements (see Chapter 9).

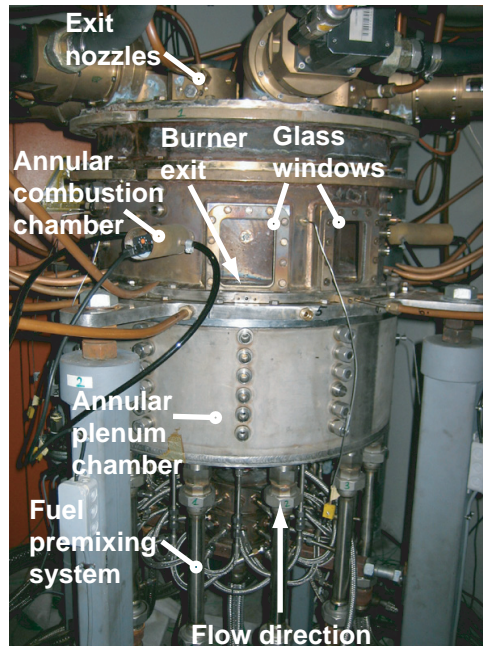


Figure 4.2: Annular combustion chamber

To protect the walls of the combustion chamber and the quartz glass windows against overheating, an external air purging system has been designed. This is supplied from the main air supply line. The walls of the plenum and combustion chamber are fitted with measurement ports for the dynamic pressure. These are distributed in both axial and circumferential directions as presented schematically in Fig. 4.3.

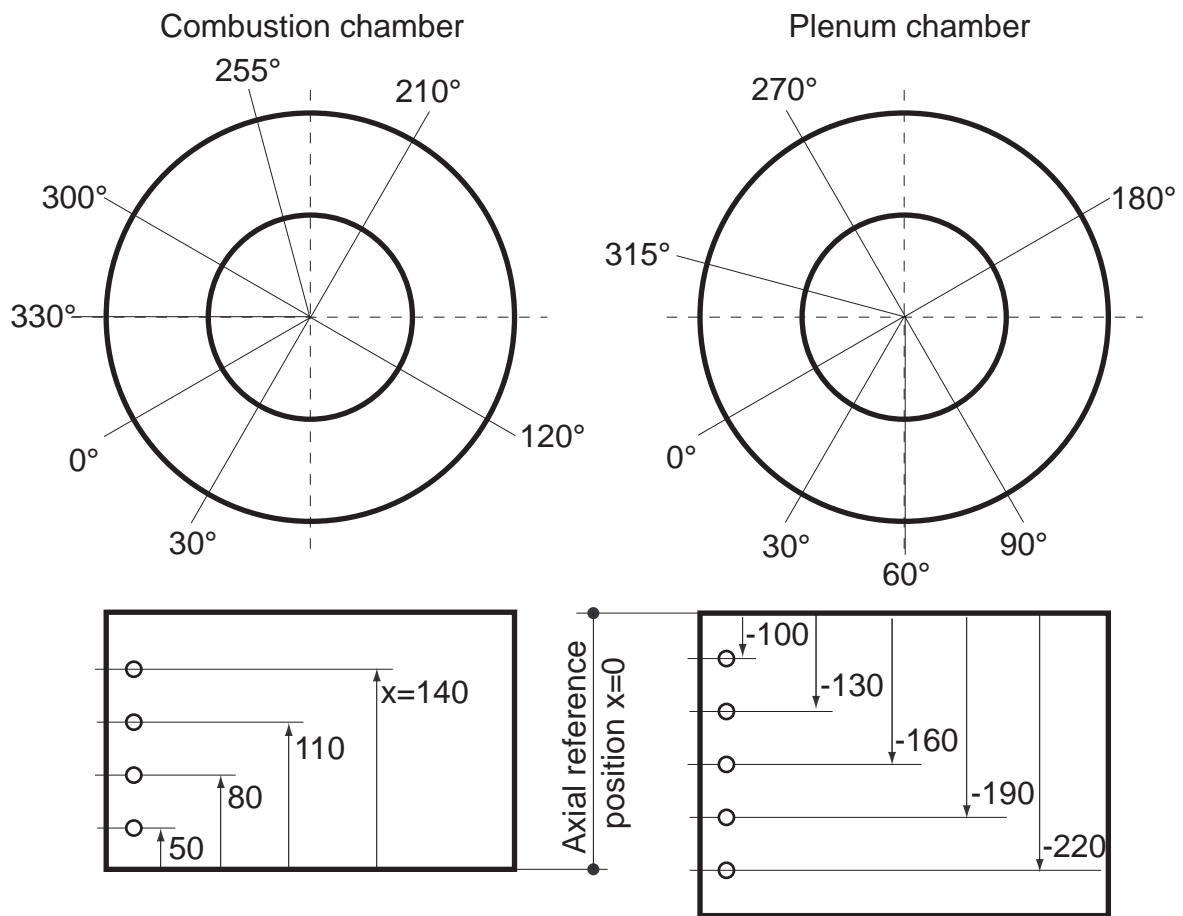


Figure 4.3: Measurement ports for the acoustic pressure in the ACC

The 12 lean premixed EV5 burners are mounted between the plenum and the combustion chamber. The end of the annular combustor is equipped with 12 water cooled convergent nozzles with an area contraction similar of that found in industrial gas turbines. The diameter of the exit nozzles can be further reduced by fitting them with special adapters. These are used in the cold isothermal flow operation in order to generate a high Mach number exit flow and thereby an acoustic exit boundary similar to the case with combustion. On the exit nozzles six step-motor driven sirens are mounted which are equally distributed on the circumference. The phase of every siren can be adjusted individually allowing the excitation of both axial and as well as azimuthal modes [33].

For monitoring and controlling the experiment, the annular combustion chamber test rig is provided with a series of thermocouples which measure the temperature of the air-fuel mixture as well the wall temperature. The measurement points for the temperature of the air-fuel mixture are placed inside the plenum and are equally distributed along the circumference. Two sensors measure the static pressure in the combustion chamber and plenum. These provide information on the flow conditions in the exit nozzles as well as the static pressure drop over the burner. In the actual configuration, the annular combustion chamber can be operated at thermal powers ranging from 500 to 1600kW and preheating temperatures up to 400°C. At nominal operation the exit nozzles are close to or at sonic conditions and the static pressure in the combustion chamber raises to almost 1bar above the ambient level.

4.2 Air Preheater Unit

The air preheater unit is shown in Fig.4.4.

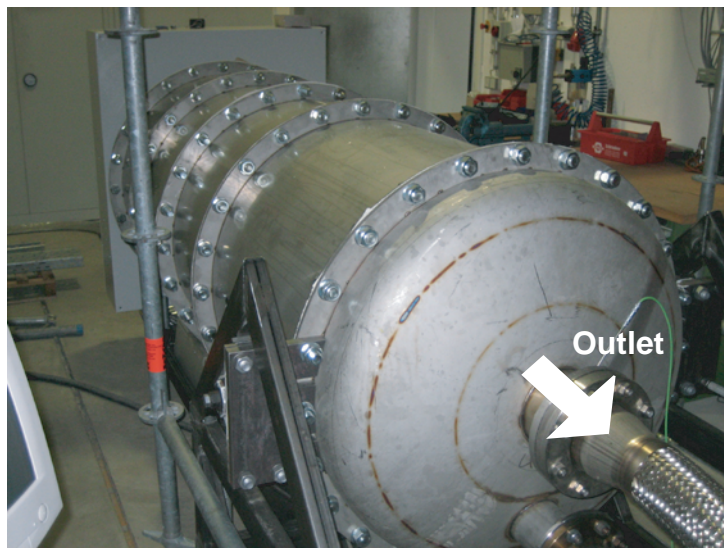


Figure 4.4: Air preheater unit

It contains 16 electrical heating elements organised in 4 independently controlled heating stages. Each element has an electrical power of 32kW@400V

and the total electrical power available is 512kW. The preheater unit was designed as a doubled-shell (see Fig. 4.5) design in order to minimise the heat losses. The 16 electrical heating elements are located in the inner shell which is forming together with the outer shell an annular duct. The air enters the annulus at the front end, is distributed equally along the circumference and flows around the thermally isolated inner liner thus absorbing the heat losses and cooling the power lines. At the back end the air flow turns and enters the inner liner and flows through the electrical heaters. After reaching the desired temperature, the combustion air exits the preheater at the front end and flows to the combustor (see Fig. 4.1). In this configuration, an air mass flow of 1kg/s can be preheated at a maximum temperature of 500°C at the outlet of the preheater unit. Due to heat losses however, the air flow reaches the annular combustor with temperatures of not much more than 400°C maximum.

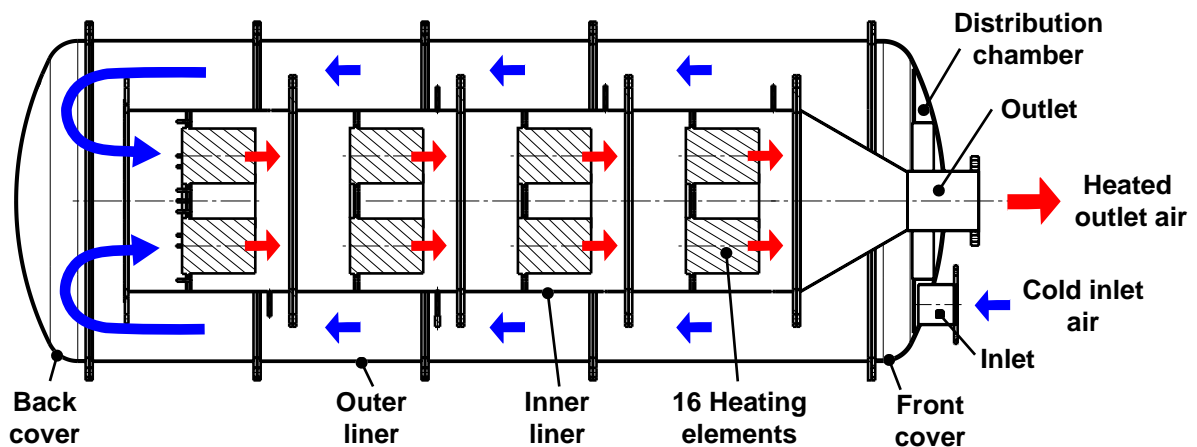


Figure 4.5: Cross section through the air preheater unit

4.3 Measurement Techniques

4.3.1 Acoustic Pressure

The dynamic pressure transducers used for the acoustic characterisation of the annular combustor were of type 106B (PCB Piezotronics). The relevant technical characteristics of the sensor are presented in Tab. 4.1.

Table 4.1: Technical characteristics of the dynamic pressure transducer Type 106B (PCB Piezotronics)

Performance	
Measurement range	57.2 kPa
Sensitivity (sensor dependent)	43.5 mV/kPa
Maximum pressure (static)	13790 kPa
Resolution	0.00069 kPa
Resonant frequency	≥ 60 kHz
Low frequency response (-5%)	0.5 Hz
Temperature range (operating)	-54 to $+121^\circ\text{C}$

For the measurements with flame, when the temperatures of the combustor wall raised over the maximum temperature allowed, the sensors have been protected against overheating by means of a specially designed cooling adaptor of Model 064B06 (see Fig. 4.6 a). During operation, this was connected to an external water cooling circuit in order to maintain the temperature of the sensor constant. A further protection feature consisted of a nitrogen purging system which deflected the hot exhaust gases away from sensitive membrane of the sensor. An additional positive effect of this was the elimination of water condensation on the walls of the adapter, which would have had a negative influence on the measurements. The configuration sensor-cooling adaptor (see Fig. 4.6 a) was fitted on the combustor wall by means of an additional mounting adaptor presented in Fig. 4.6 b.

Due to the protective design solutions - the cooling and mounting adapters - the sensitive membrane lies a certain distance away from the inner surface

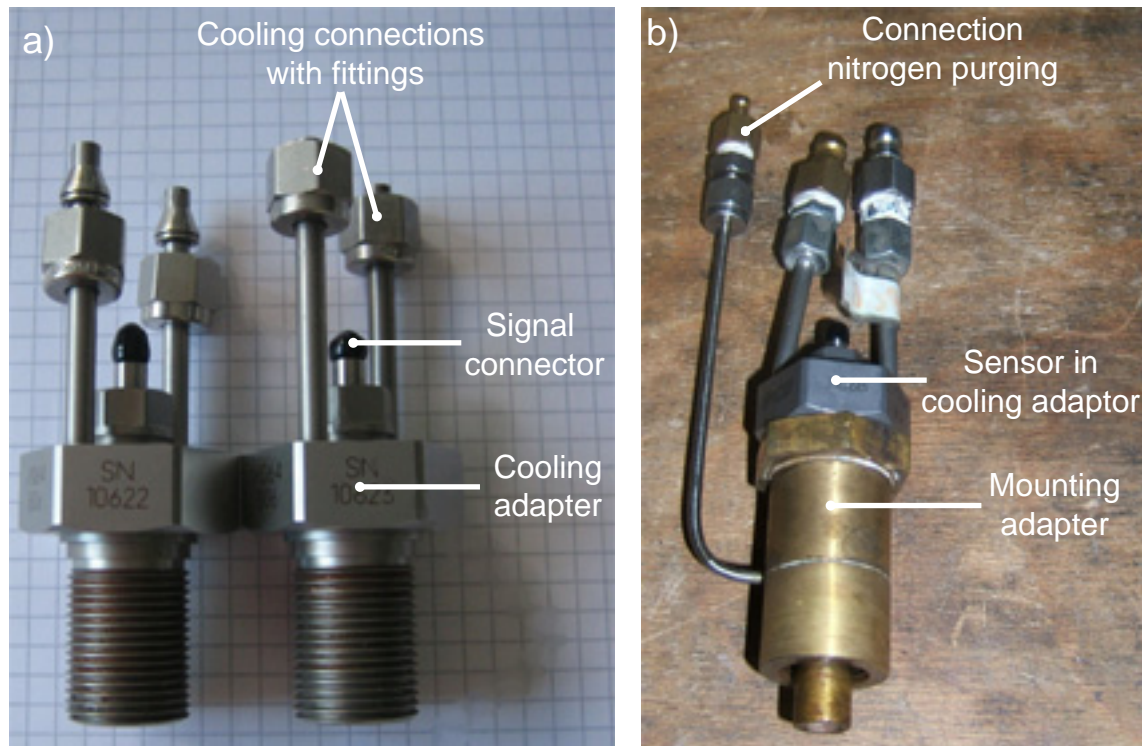


Figure 4.6: Dynamic pressure transducer Type 106B. a) Sensor and cooling adapter. b) Sensor, cooling and mounting adapter

of the combustor wall. Thus, the sensor does not measure the acoustic field directly but through a measurement channel (see Fig. 4.7 b). To evaluate the effect of this on the measurement performances and to account for the differences in the sensor sensitivities, every sensor was subjected to a calibration procedure.

The calibration arrangement is presented schematically in Fig. 4.8. This consists of a pipe with a sound source (speaker) mounted at one end. The speaker is connected to a signal generator which provides a sound wave with a defined amplitude and frequency. At the opposite end, the sensor to be calibrated and the reference sensor are mounted at the same axial position. The two sensors are connected directly to the DAQ card (National Instruments Model PCI-4472) in the measurement PC. This was used as data acquisition system as well as a current supply source for the piezo-electric sensors.

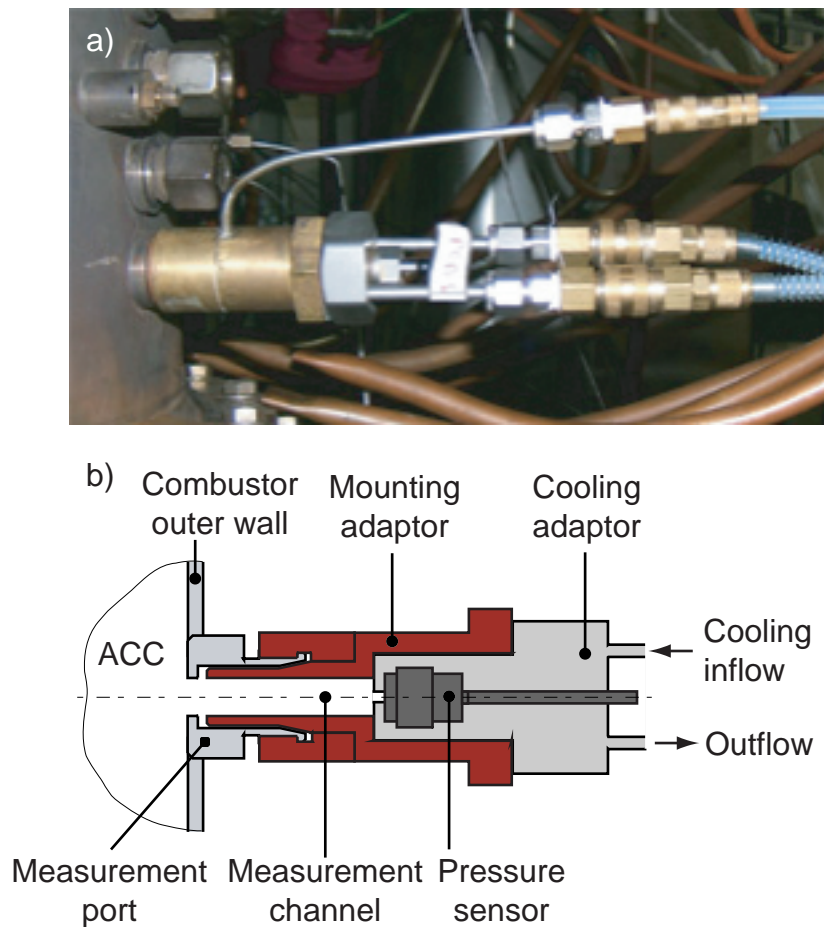


Figure 4.7: Dynamic pressure sensor mounted on the combustor wall: a) actual configuration and b) schematic representation

By cross correlating the signals from the calibrated sensors with the reference, the acoustic influence of the cooling and mounting adaptors was evaluated. Further, by relating the sensor units between themselves, a frequency dependent correction function was calculated in order to compensate for the differences in the sensor sensitivities. Afterwards, the correction function was applied to the measured data. The calibration result for one sensor with respect to the reference is presented in Fig. 4.9.

Here, it can be seen that the amplitude of the calibrated sensor (blue line) raises steadily with frequency and is at 800 Hz by a factor 1.3 larger than the reference. This behaviour is generated by a Helmholtz resonance effect of the

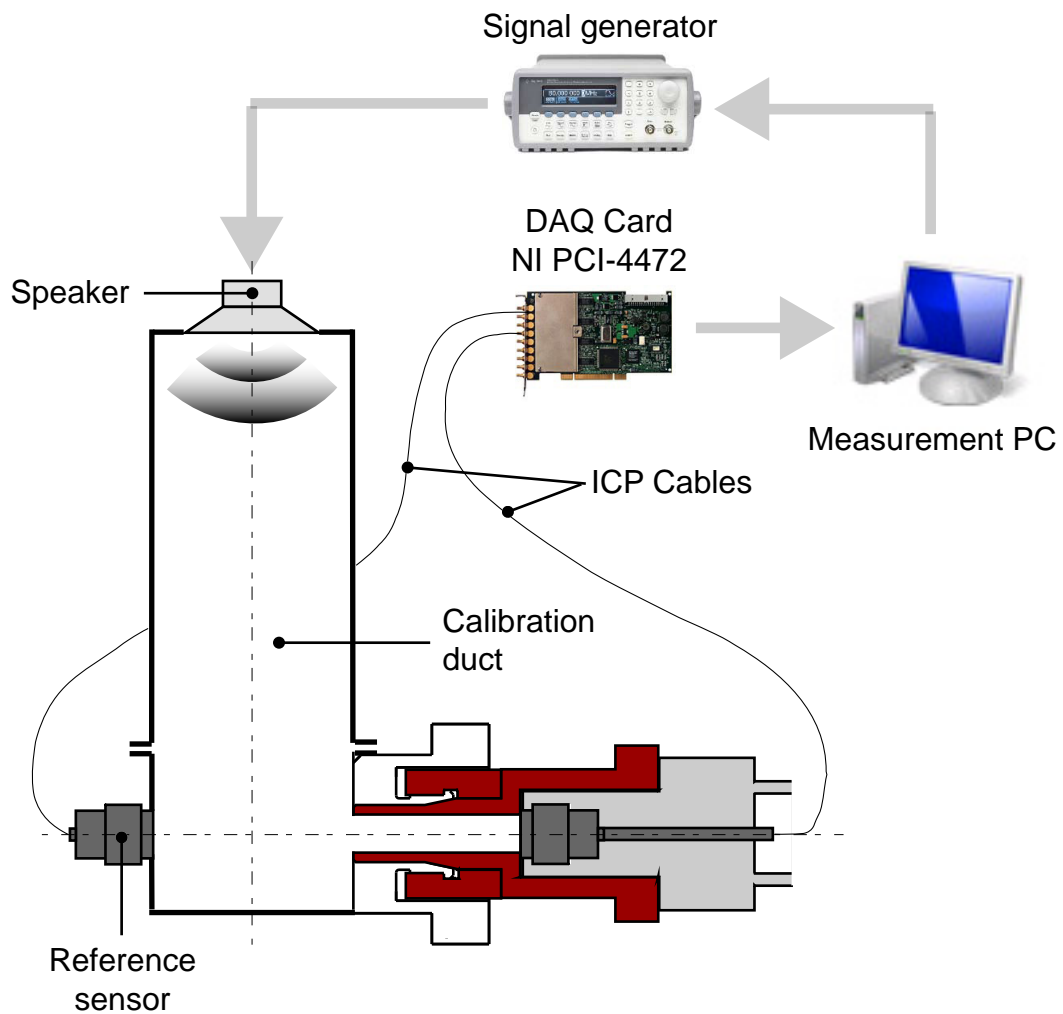


Figure 4.8: Schematic representation of the calibration set-up for the dynamic pressure transducers

mounting adapter. The vibrating element of the resonator is represented by the mass of gas enclosed in the measurement channel of the length L and diameter d (neck of the resonator). Further, the spring effect is produced by the volume of gas enclosed between the cooling and the mounting adapters (see Fig. 4.10).

During the design phase, the Helmholtz effect was minimised by shifting the

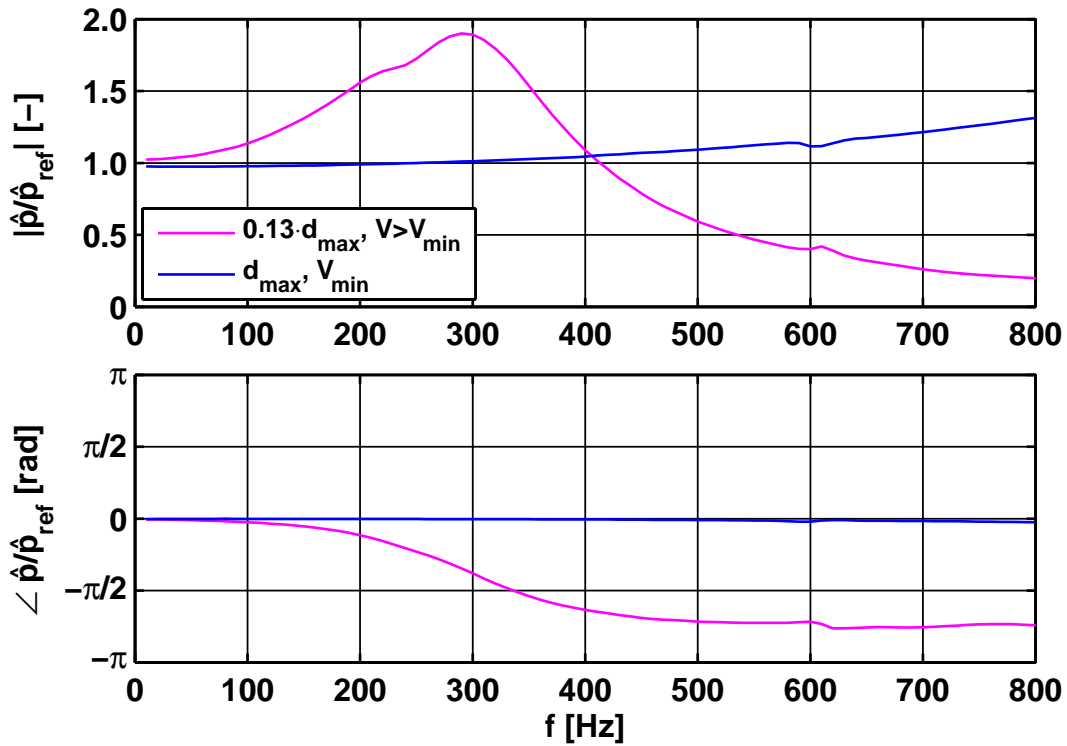


Figure 4.9: Calibration curves from one sensor with respect to the reference for different design configurations of the mounting adapter

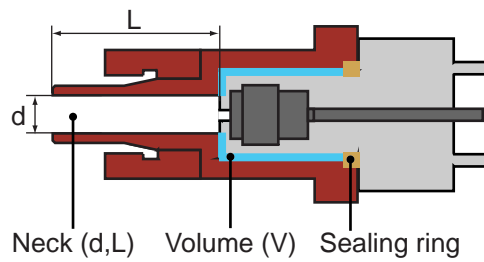


Figure 4.10: Schematic representation of the Helmholtz resonator in the mounting adapter

resonance domain towards higher frequencies. The diameter d of the measurement channel was increased as much as possible and the volume V between the sensor and the mounting adapter was reduced by inserting additional sealing material. Because of geometrical constraints, the length L could not be further decreased and was kept constant. The optimal configuration

is defined by the dimensions d_{max} , L and V_{min} and corresponds to the calibration curve presented in Fig. 4.9 (blue line). Here, the frequency of the Helmholtz resonator lies close to 3000 Hz, well over the frequency domain of interest (0-800 Hz). As a comparison, Fig. 4.9 shows also the calibration curve of a much worse design of the mounting adapter (magenta line). For this the diameter of the measurement channel d was smaller than the maximal value ($d = 0.13 \cdot d_{max}$) and the volume V was maximum. It can be clearly seen that for this design the dynamic behaviour of the resonator has the peak frequency at 300 Hz and stretches on the entire frequency domain of interest. This influences significantly the measurement performances of the sensor in both amplitude and phase. The amplitude raises steadily with frequency and reaches a maximum being almost twice as large as the reference. Then, by further increasing the frequency it drops significantly below the reference level. The phase shows also large deviations especially in the upper half of the frequency domain. Here, the difference with respect to the reference is -2.4 rad.

The calibration procedure of one sensor was taking approximately three quarters of an hour including here the mounting preparations for the sensor itself and for the additional cooling arrangement. Hence, the calibration of all 13 sensors together with the data post processing and analysis procedure was stretching over almost two days.

For the acoustic measurements on the test rig, the sensors were fixed on the outer wall of the combustion chamber and plenum as presented in Fig. 4.6 b. The acoustic field was recorded in time series sampled at rates of 16384 samples/second and measurement time stretching between one and ten seconds. To transfer the rough time domain data in the frequency space, the post processing procedure of the measured time domain signals consisted in the first step of a Fourier transformation and the computation of a Frequency Response Function (FRF). The reference input for the computation of the FRF was the dynamic signal measured from one sensor. To obtain representative results for every frequency, a large number of loops of time domain series were stored and post processed for every frequency and channel. The final result was the average of the complex acoustic pressure.

4.3.2 Optical Measurements

In natural gas premixed combustion the chemiluminescence of the OH* radicals can be used as an indicator for the heat release rate density ([42], [26]). The OH*-chemiluminescence from the flame was acquired with the high speed camera Fastcam Ultima APX from Photron. The camera head was positioned and focused to capture the flame from one burner through the quartz glass windows of the combustion chamber (Chapter 4). The lens of the camera was fitted with an UV band pass filter of the model UG11 which captures most of the OH*-radiation.

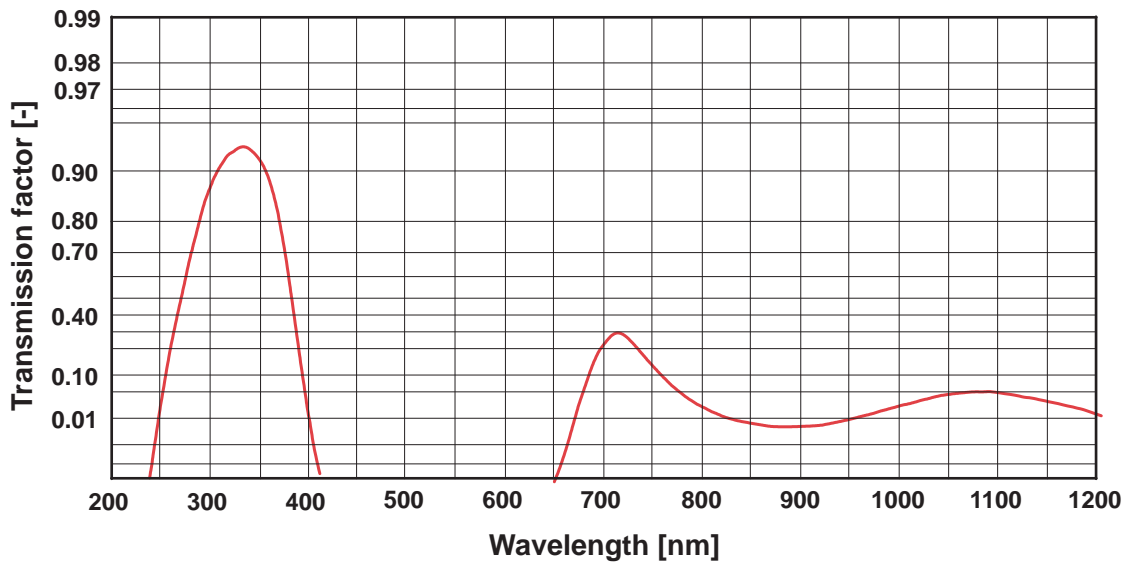


Figure 4.11: Transmission spectrum of the UV band pass filter UG11

The optical measurements were made at a sampling frequency of 2000 frames/second and a number of 2048 single shots with a resolution of 512x1024 pixel were saved. The main goal of post processing procedure was to obtain the time averaged OH*-chemiluminescence distribution (see Fig. 4.12). As the turbulent integral time scales in premixed flames are in the frequency range of 200-500 Hz, the averaging procedure was made on 500 instantaneous pictures. Because of the low number of samples, low frequency phenomenons like the fluctuation of the ORZ could not be resolved correctly. For this reason, the optical measurements for the determination of the BTM and FTM were

made at operating points where the flame was burning stable and no dominant low frequency fluctuations of the reaction zone were encountered. Thus, the 500 single shots were sufficient for getting a good average distribution. This was also confirmed by the convergence analysis of the averaging procedure. The low frequency fluctuation of the ORZ appeared especially at operating regions close to the LBO limit, which in this phase of the work was not a subject of the investigations.

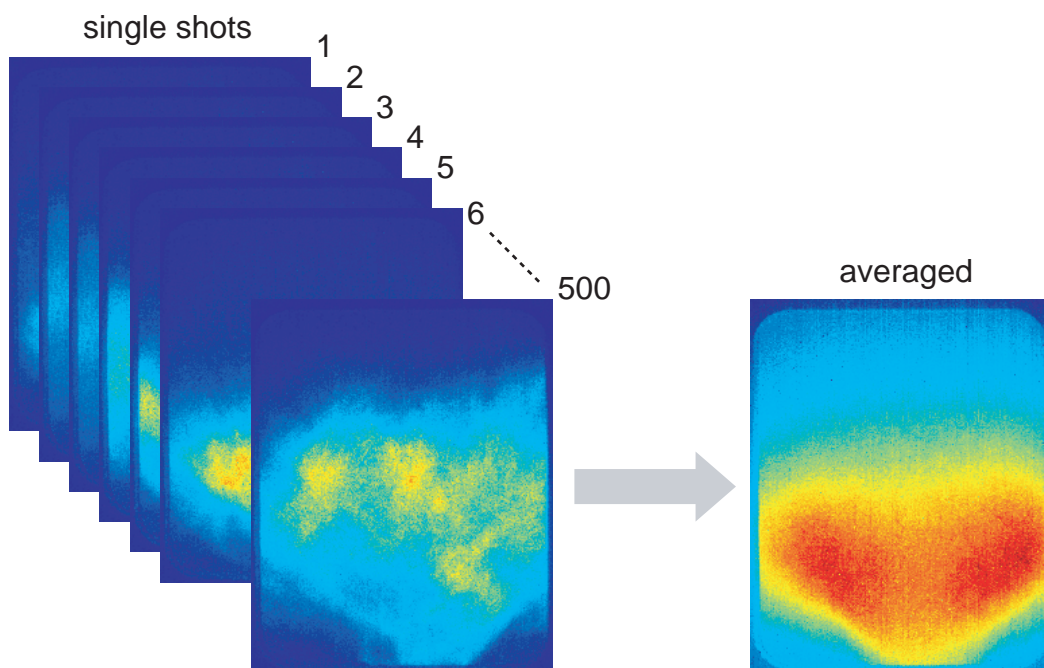


Figure 4.12: Schematic representation of the averaging procedure for the determination of the OH*-Chemiluminescence distribution

5 Acoustics Theory

The acoustic field of an annular combustor has a complex multi dimensional character. This raises the complexity of the problem considerably when analysing the combustion instabilities observed in real engines (see Chapter 2) due to the large number of degrees of freedom, which may contribute to the oscillation. As seen in Chapter 2, axial, azimuthal and even radial modes were encountered unstable in industrial gas turbines. The annular combustor test rig at Lehrstuhl für Thermodynamik of TU München, described in detail in Chapter 4, has shown as well unstable axial and azimuthal modes. Therefore, a comprehensive and fundamental understanding of the complex acoustic field of an annular combustor is a necessary prerequisite for further analysis.

In the following, the homogeneous convective wave equation which describes the propagation of acoustic perturbations will be introduced. Then, the solution of the convective wave equation for simple annular ducts is presented. The damping effects which influence the propagation of the sound waves are summarized at the end of the theory chapter. Hereby, only the flow induced dissipation of the acoustic waves and the visco-thermal damping in boundary layers are considered.

5.1 Linearised Euler Equations

The derivation of the linearised Euler equations for acoustic perturbations starts with the conservation equations of mass, momentum and energy presented in Eqns. 5.1, 5.2 and 5.3, respectively. Here, it is assumed that the fluid is inviscid and no volume forces act on the fluid element.

$$\frac{D\rho}{Dt} + \rho \nabla \cdot \mathbf{u} = 0 \quad (5.1)$$

$$\frac{D\mathbf{u}}{Dt} + \frac{1}{\rho} \nabla p = 0 \quad (5.2)$$

$$\frac{1}{c^2} \frac{Dp}{Dt} + \rho \nabla \cdot \mathbf{u} = 0 \quad (5.3)$$

In Eqns. 5.1, 5.2 and 5.3

$$\frac{D}{Dt} = \frac{\partial}{\partial t} + \mathbf{u} \cdot \nabla \quad (5.4)$$

is the material derivative and ∇ the gradient operator. Regarding the acoustic perturbations, it is assumed further that the relative change in the density due to pressure fluctuations is small which implies that the linearised theory may be used as a first order approximation in describing the unsteady pressure field. The flow variables are expressed in the time domain in terms of a mean value ($\bar{\quad}$) and the fluctuating component (\prime) as

$$p = \bar{p} + p'(x, t) \quad (5.5)$$

$$\mathbf{u} = \bar{\mathbf{u}} + \mathbf{u}'(x, t) \quad (5.6)$$

$$\rho = \bar{\rho} + \rho'(x, t) \quad (5.7)$$

where x is the axial coordinate and t the time. When expanding the mass, momentum and energy equations after having introduced Eqns. 5.5, 5.6 and 5.7, a series of terms containing mean flow quantities and acoustic fluctuations at the first and higher orders are obtained. The terms containing exclusively mean quantities represent the stationary solution. They satisfy the conservation equations and can be subtracted. From the remaining terms only those of first order in the acoustic fluctuations are of interest. The second and higher order terms are very small and can be neglected. With these assumptions, the

homogeneous linearised Euler equations for acoustic perturbations are obtained and are given in Eqns. 5.8, 5.9 and 5.10. A detailed derivation can be found in [43].

$$\frac{\partial \rho'}{\partial t} + \bar{\mathbf{u}} \cdot \nabla \rho' + \mathbf{u}' \cdot \nabla \bar{\rho} + \bar{\rho} \nabla \cdot \mathbf{u}' + \rho' \nabla \cdot \bar{\mathbf{u}} = 0 \quad (5.8)$$

$$\frac{\partial \mathbf{u}'}{\partial t} + (\bar{\mathbf{u}} \cdot \nabla) \mathbf{u}' + (\mathbf{u}' \cdot \nabla) \bar{\mathbf{u}} + \frac{\nabla p'}{\bar{\rho}} - \frac{(\nabla \bar{p}) \rho'}{\bar{\rho}^2} = 0 \quad (5.9)$$

$$\frac{\partial p'}{\partial t} + \bar{\mathbf{u}} \cdot \nabla p' + \mathbf{u}' \cdot \nabla \bar{p} + \gamma \bar{p} \nabla \cdot \mathbf{u}' + \gamma p' \nabla \cdot \bar{\mathbf{u}} = 0 \quad (5.10)$$

5.2 Acoustic Wave Equation

For the derivation of the acoustic wave equation, the mass (Eqn. 5.8) and momentum (Eqn. 5.9) conservation equations for a fluid at rest ($\bar{\mathbf{u}} = 0$) are considered. After expressing the isentropic density fluctuations ρ' in terms of the acoustic pressure p' and the speed of sound c as

$$c^2 = \frac{p'}{\rho'}, \quad (5.11)$$

these become:

$$\frac{1}{c^2} \frac{\partial p'}{\partial t} + \bar{\rho} \nabla \cdot \mathbf{u}' = 0 \quad (5.12)$$

$$\bar{\rho} \frac{\partial \mathbf{u}'}{\partial t} + \nabla p' = 0 \quad (5.13)$$

Taking now the temporal derivative ($\partial/\partial t$) of Eqn. 5.12 and the spatial derivative (∇) of Eqn. 5.13 and combining both by eliminating the term contain-

ing \mathbf{u}' , the homogeneous 3D wave equation for the acoustic pressure p' is obtained:

$$\frac{\partial^2 p'}{\partial t^2} - c^2 \nabla^2 p' = 0 \quad (5.14)$$

When considering a mean flow with the absolute velocity $\bar{\mathbf{u}}$, the partial differential $\partial/\partial t$ is replaced with the material derivative from Eqn. 5.4 and thus, the 3D convective wave equation results:

$$\left(\frac{\partial}{\partial t} + \bar{\mathbf{u}} \cdot \nabla \right)^2 p' - c^2 \nabla^2 p' = 0 \quad (5.15)$$

In the framework presented here, only the 1D and 2D forms of the convective wave equation are of interest. The typical design of an annular combustion chamber has a small width compared with its axial and circumferential dimensions and with the wavelengths of the frequencies where pressure pulsations normally occur. For this reason, the radial dimension, which corresponds to the width of the annulus, is neglected in many studies ([18], [58], [16]) and thus, the acoustic wave propagation in annular combustion chambers is assumed to be 2D. The model of the annular duct simplified in this way is referred to as *thin annular duct*. Furthermore, the absolute mean velocity $\bar{\mathbf{u}}$ has only an axial component \bar{u} . Hence, the acoustic wave equation writes for a thin annular duct

$$\left(\frac{\partial}{\partial t} + \bar{u} \frac{\partial}{\partial x} \right)^2 p' - c^2 \left(\frac{\partial^2 p'}{\partial x^2} + \frac{\partial^2 p'}{\partial y^2} \right) = 0 \quad (5.16)$$

and for a 1D case

$$\left(\frac{\partial}{\partial t} + \bar{u} \frac{\partial}{\partial x} \right)^2 p' - c^2 \frac{\partial^2 p'}{\partial x^2} = 0. \quad (5.17)$$

In Eqns. 5.16 and 5.17, x and y are the axial and the circumferential directions of propagation, respectively.

5.3 Harmonic Oscillations

A convenient description of the acoustics in an industrial gas turbine is obtained if it can be assumed that pressure pulsations are time dependent harmonic oscillations of the form $e^{i\omega t}$. Hence, the acoustic fluctuation p' can be written as

$$p'(t) = \hat{p}(x)e^{i\omega t} \quad (5.18)$$

where $\hat{p}(x)$ is the complex amplitude and ω the angular frequency of the oscillation. When ω is complex

$$\omega = \text{Re}(\omega) + i \text{Im}(\omega) \quad (5.19)$$

the real part $\text{Re}(\omega)$ represents the real angular frequency and the imaginary part $\text{Im}(\omega)$ the growth rate of the oscillation. The latter gives information on the stability of the system. When the imaginary part is negative ($\text{Im}(\omega) < 0$) the amplitude of the acoustic pressure p' grows in time describing an unstable acoustic system. Consequently, if the imaginary part is positive ($\text{Im}(\omega) > 0$) the amplitude decays, i.e. the system is damped.

5.3.1 Helmholtz Equation

Assuming a harmonic time dependence $e^{i\omega t}$ for the acoustic variables and replacing the time derivative $\partial/\partial t = i\omega$, the acoustic wave equation (Eqn. 5.14) can be written for the particular case of harmonic oscillations in the frequency domain. This yields the Helmholtz equation for a 2D wave propagation:

$$\frac{\omega^2}{c^2} \hat{p} + \left(\frac{\partial^2 \hat{p}}{\partial x^2} + \frac{\partial^2 \hat{p}}{\partial y^2} \right) = 0 \quad (5.20)$$

5.3.2 Acoustic Waves in Longitudinal 1D Ducts

The solution of the Helmholtz equation for a 1D wave propagation in straight ducts with constant cross-section and mean flow of velocity \bar{u} is in terms of the complex acoustic pressure \hat{p}

$$\frac{1}{\bar{\rho}c} \hat{p}(x) = \left(f e^{-ik_x^+ x} + g e^{-ik_x^- x} \right) \quad (5.21)$$

and in terms of the complex acoustic velocity \hat{u}

$$\hat{u}(x) = \left(f e^{-ik_x^+ x} - g e^{-ik_x^- x} \right). \quad (5.22)$$

The parameter k_x^\pm is the axial wavenumber describing the distribution of the acoustic mode in axial direction defined as

$$k_x^\pm = \pm \frac{\omega}{c \pm \bar{u}} = \pm \frac{\omega}{c(1 \pm M)} \quad (5.23)$$

where $M = \bar{u}/c$ is the Mach number and c the velocity of sound.

Eqns. 5.21 and 5.22 describe the 1D acoustic field as a superposition of the Riemann invariants f and g . These are acoustic velocity waves propagating in the downstream and upstream directions, respectively, as presented in Fig. 5.1.

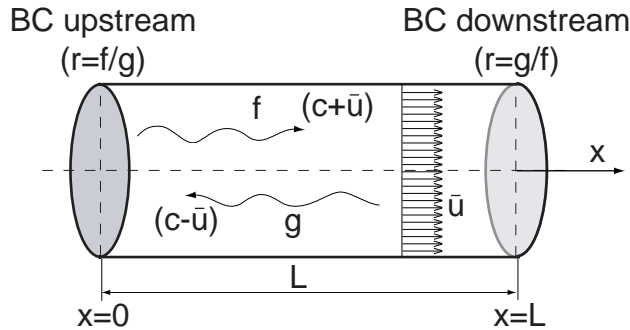


Figure 5.1: 1D wave propagation in the presence of a mean axial flow (\bar{u})

The relation between the Riemann invariants f and g and the acoustic variables pressure p' and velocity u' can be deduced from Eqs. 5.21 and 5.22 and are given in Eqs. 5.24 and 5.25 at a particular axial coordinate x :

$$f = \frac{1}{2} \left(\frac{p'}{\rho c} + u' \right) \quad (5.24)$$

$$g = \frac{1}{2} \left(\frac{p'}{\rho c} - u' \right) \quad (5.25)$$

5.3.3 Acoustic Intensity, Energy, Impedance, Admittance and Reflection

The physical characteristics of the acoustic field are expressed by scalar and vectorial variables like the acoustic intensity, energy, admittance and impedance. The acoustic intensity i_{ac} is a complex variable defined in terms of the acoustic pressure p' and velocity u' :

$$i_{ac} = u' p' \quad (5.26)$$

The variable i_{ac} is a vector which describes the transport of acoustic energy. The acoustic energy includes the kinetic energy of the infinitesimal motion of the molecules and the volume expansion work of the isentropic compression at the wave front. Thus, the acoustic energy is:

$$e_{ac} = \frac{1}{2} \rho u'^2 + \frac{1}{2} \frac{1}{c^2 \rho} p'^2 \quad (5.27)$$

The acoustic impedance and admittance are complex variables, which characterise the acoustic field in one point in terms of the the variables pressure and velocity:

$$Z = \frac{\hat{p}}{\hat{u}} \quad (5.28)$$

The admittance is the inverse of the impedance:

$$A = \frac{1}{Z} = \frac{\hat{u}}{\hat{p}} \quad (5.29)$$

The acoustic variables presented above can be used to describe acoustic boundary conditions. Physically open ($p' = 0$) and closed (hard wall) ($u' = 0$) ends are fully reflective acoustic boundaries. The acoustic intensity is here zero ($i_{ac} = p' u' = 0$). At the open end the acoustic pressure vanishes and the impedance is zero ($Z = 0$) and at the closed end the acoustic velocity is zero which yields that the impedance tends to infinity.

The Riemann invariants f and g from Eqns. 5.21 and 5.22 are related at the boundaries (Fig. 5.1, $x = 0$ and $x = L$) through the reflection coefficient r . The reflection coefficient r of the boundary is defined as the complex ratio of the reflected and the transmitted waves as

$$r = \frac{g}{f} \quad (5.30)$$

for the downstream boundary and

$$r = \frac{f}{g} \quad (5.31)$$

for the upstream boundary. If Eqns. 5.21 and 5.22 are introduced in Eqns. 5.28 and 5.29, the impedance and admittance of the acoustic boundary can be expressed in terms of the reflection coefficient r :

$$Z = \frac{\hat{p}}{\hat{u}} = \frac{1}{\bar{\rho}c} \frac{1+r}{1-r} \quad (5.32)$$

$$A = \frac{\hat{u}}{\hat{p}} = \bar{\rho}c \frac{1-r}{1+r} \quad (5.33)$$

Depending on the values of the reflection coefficient r several cases with practical relevance can be distinguished:

- $r = \pm 1$ - fully reflective acoustic boundary. When the reflection coefficient is ± 1 the amplitudes of the Riemann invariants f and g are equal. The amplitude of the resulting acoustic mode is characterised by a stationary pattern with fixed axial positions for the nodes and antinodes. The resulting phase shows $\pm\pi$ jumps delimiting the antinodes which oscillate in opposition of phase. The case when the reflection coefficient is unity ($r = 1$) corresponds to a physical closed end whereas $r = -1$ is an open end.
- $r < |1|$ - partially reflective acoustic boundary.
- $r = 0$ - non-reflective acoustic boundary (anechoic). In this case the acoustic energy is entirely transported over the boundary of the system and the reflected wave has a zero amplitude. This acoustic state is characterized by propagating waves with a constant amplitude and a linearly falling phase in the direction of propagation.

5.3.4 Acoustic Waves in Thin Annular Ducts

The solution of the Helmholtz equation for thin annular ducts is [49]

$$\frac{1}{\bar{\rho}c} \hat{p}(x, y) = r_{++} + r_{+-} + r_{-+} + r_{--} \quad (5.34)$$

where $r_{\pm\pm}$ designate four helical waves, travelling in the downstream and upstream directions with a clockwise and anticlockwise sense of rotation as represented schematically in Fig. 5.2. The helical waves $r_{\pm\pm}$ are defined as

$$r_{++}(x, y) = R_{++} e^{-ik_y^+ y - ik_x^+ x} \quad (5.35)$$

$$r_{+-}(x, y) = R_{+-} e^{-ik_y^- y - ik_x^+ x} \quad (5.36)$$

$$r_{-+}(x, y) = R_{-+} e^{-ik_y^+ y - ik_x^- x} \quad (5.37)$$

$$r_{--}(x, y) = R_{--} e^{-ik_y^- y - ik_x^- x} \quad (5.38)$$

where $R_{\pm\pm}$ are the complex amplitudes of the helical waves $r_{\pm\pm}$ of order m .

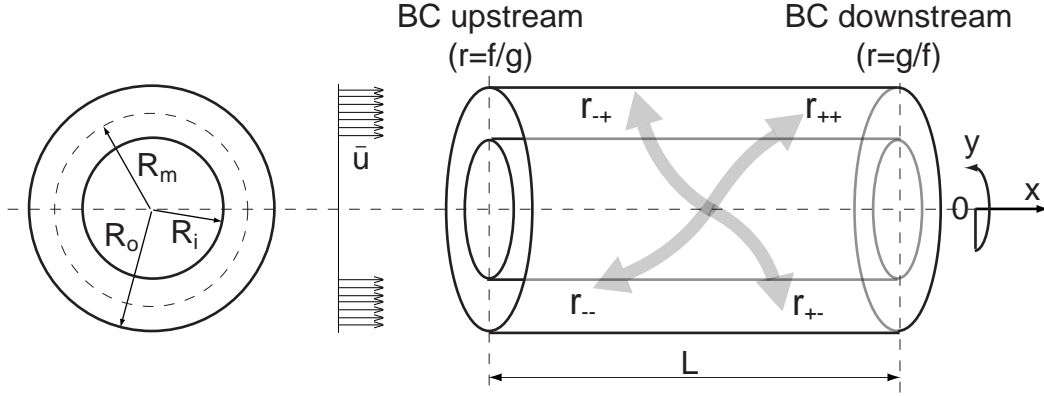


Figure 5.2: 2D acoustic field in an annular duct

By introducing Eqns. 5.35 to 5.38 in Eqn. 5.34, the general solution of the Helmholtz equation for a thin annular duct in terms of the complex acoustic pressure \hat{p} is obtained:

$$\frac{1}{\bar{\rho}c} \hat{p}(x, y) = \left(R_{++} e^{-ik_y^+ y} + R_{+-} e^{-ik_y^- y} \right) e^{-ik_x^+ x} + \left(R_{-+} e^{-ik_y^+ y} + R_{--} e^{-ik_y^- y} \right) e^{-ik_x^- x} \quad (5.39)$$

The azimuthal wavenumber k_y^\pm is derived from Eqn. 5.39 by applying the condition of mode continuity in the circumferential direction y

$$\left. \frac{\partial \hat{p}}{\partial y} \right|_{y=0} = \left. \frac{\partial \hat{p}}{\partial y} \right|_{y=2\pi R_m} = 0 \quad (5.40)$$

as

$$k_y^\pm = \pm \frac{m}{R_m}. \quad (5.41)$$

In Eqn. 5.41 m is the azimuthal mode index and R_m the mean radius of the annulus. R_m is defined in terms of the inner R_i and outer R_o radii as:

$$R_m = \frac{R_i + R_o}{2} \quad (5.42)$$

The axial wavenumber k_x^\pm describes the acoustic wave propagation in axial direction. This is illustrated in Fig. 5.3 for a generic (x, y) plane.

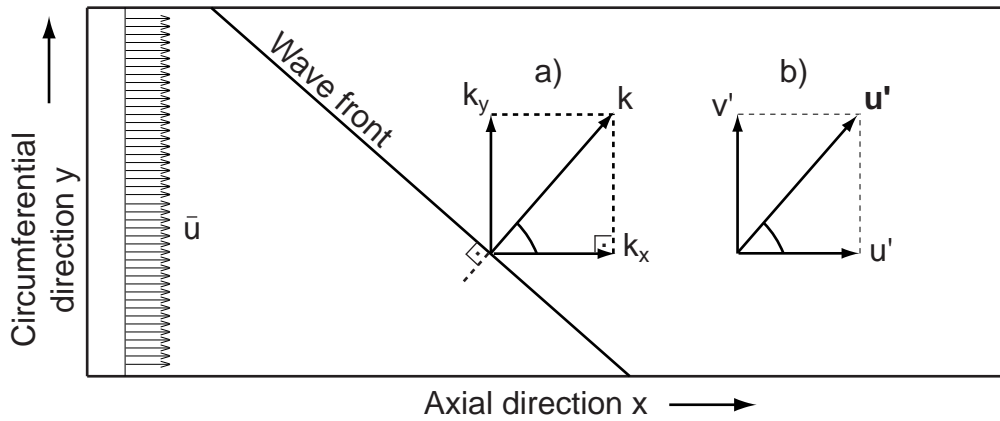


Figure 5.3: Schematic representation of the wave propagation in a 2D acoustic field, the global wavenumber k is perpendicular on the wave front. a) triangle of wavenumbers; b) triangle of acoustic velocities

The parameter k is the global wavenumber defined as:

$$k = \frac{\omega}{c} - Mk_x \quad (5.43)$$

The second term in Eqn. 5.43 is the Mach number correction ($M = \bar{u}/c$) describing the effect of the mean flow on the acoustic wave propagation, similarly to the convective wave equation (Eqns. 5.15, 5.16 and 5.17). As seen in Fig. 5.3 a, the axial k_x , azimuthal k_y and global k wavenumbers satisfy the following equation:

$$k_x^2 + k_y^2 = \left(\frac{\omega}{c} - Mk_x \right)^2 \quad (5.44)$$

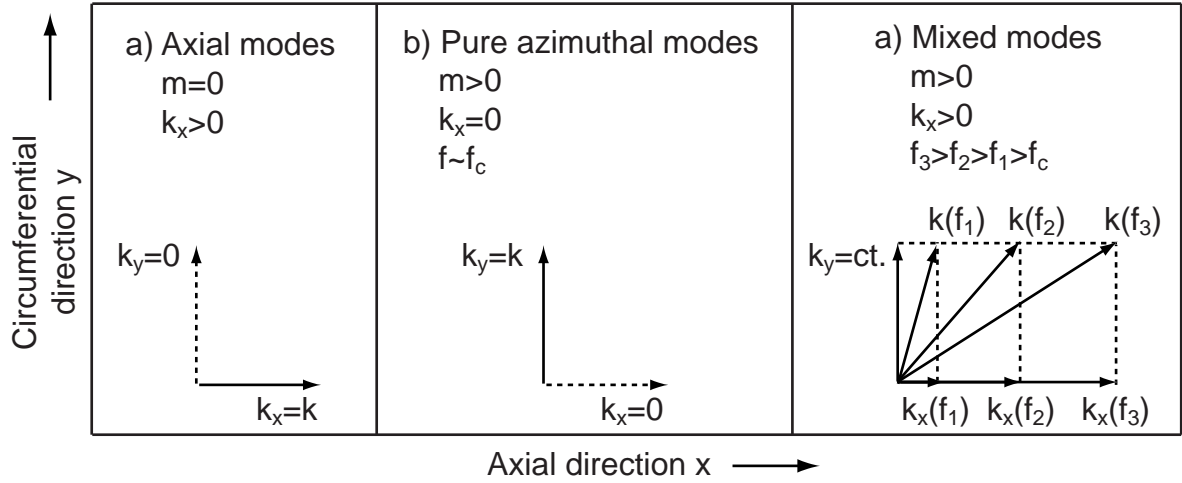


Figure 5.4: Modal components as a function of the azimuthal mode index m and the axial wavenumber k_x

Eqn. 5.44 can be solved for the axial wavenumber k_x^\pm :

$$k_x^\pm = \frac{\omega}{c(1-M^2)} \left(-M \pm \sqrt{1 - \left(\frac{m c}{R_m \omega}\right)^2 (1-M^2)} \right) \quad (5.45)$$

The axial wavenumber k_x^\pm describes the acoustic wave propagation in axial direction as presented schematically in Figs. 5.3 and 5.4. The modes propagate only if k_x^\pm is real, i.e the quantity under square root in Eqn. 5.45 is positive:

$$\left(\frac{\omega}{c}\right)^2 - \left(\frac{m}{R_m}\right)^2 (1-M^2) \geq 0 \quad (5.46)$$

If the above inequality is not satisfied the axial wavenumber is complex with a negative imaginary part. Hence, the respective modes will be attenuated exponentially and will not propagate in the axial direction (evanescent waves). The cut-on frequency of the mode m is defined as:

$$f_c = \frac{m c}{2\pi R_m} \sqrt{1-M^2} \quad (5.47)$$

According to Fig. 5.4, when $m = 0$ the azimuthal wavenumber k_y^\pm is zero as well and thus, k_x^\pm describes the propagation of planar modes in the axial direction. Here, k_x^\pm is a real number, i.e. the planar modes always propagate. For $m > 0$, k_x^\pm describes the propagation of non-planar modes in the axial direction. Two cases can be distinguished here (see Fig. 5.4 b and c). For frequencies lower than the cut-on frequency f_c , k_x^\pm is complex with a negative imaginary part and the modes are exponentially damped (evanescent) in the axial direction. With increasing the frequency close to the cut-on value, k_x^\pm tends to zero meaning that the acoustic waves propagate only along the circumferential direction, i.e. pure azimuthal modes (Fig. 5.4 b). For frequencies above the cut-on value, k_x^\pm is positive ($k_x^\pm > 0$) and k_y^\pm remains constant. The axial wavenumber k_x^\pm describes the propagation of mixed modes - both axial and azimuthal components - in the axial direction (Fig. 5.4c).

The inclination of the wave front with respect to the x axis is (see Fig. 5.3)

$$\kappa_u^\pm = \frac{k_x^\pm}{k} = \frac{k_x^\pm}{\omega/c - Mk_x^\pm} \quad (5.48)$$

and with respect to the y axis

$$\kappa_v^\pm = \frac{m/R_m}{k} = \frac{m/R_m}{\omega/c - Mk_x^\pm}. \quad (5.49)$$

The factors κ_u^\pm and κ_v^\pm are used together with the momentum equation (Eqn. 5.2) to express the acoustic velocity components in the axial and the azimuthal directions as ([19]):

$$\hat{u}(x, y) = \kappa_u^+ e^{-ik_x^+ x} \left(R_{++} e^{-ik_y^+ y} + R_{+-} e^{-ik_y^- y} \right) + \kappa_u^- e^{-ik_x^- x} \left(R_{-+} e^{-ik_y^+ y} + R_{--} e^{-ik_y^- y} \right) \quad (5.50)$$

$$\hat{v}(x, y) = \kappa_v^+ e^{-ik_x^+ x} \left(R_{++} e^{-ik_y^+ y} - R_{+-} e^{-ik_y^- y} \right) + \kappa_v^- e^{-ik_x^- x} \left(R_{-+} e^{-ik_y^+ y} - R_{--} e^{-ik_y^- y} \right) \quad (5.51)$$

The azimuthal modes can exhibit a standing, spinning or a mixed pattern de-

pending on the relation between the complex amplitudes $R_{\pm\pm}$ of the helical waves. If the amplitudes of the waves propagating in the clockwise and anti-clockwise sense of rotations are equal

$$R_{++} = R_{+-} = \frac{F}{2} \quad (5.52)$$

and

$$R_{-+} = R_{--} = \frac{G}{2} \quad (5.53)$$

the azimuthal mode has a standing character with fixed circumferential positions for the nodes and antinodes (Fig. 5.5). In this case the acoustic field in an annular duct is reduced to the waves F and G propagating in the upstream and downstream directions.

If the azimuthal components have a standing character, the mode shape in circumferential direction (see Eqn. 5.39) can be described analytically by a cosine function:

$$\frac{1}{\bar{\rho}c} \hat{p}(x, y) = \cos\left(\frac{m}{R_m} y\right) \left(F e^{-ik_x^+ x} + G e^{-ik_x^- x} \right) \quad (5.54)$$

The expressions for the acoustic velocities are

$$\hat{u}(x, y) = \cos\left(\frac{m}{R_m} y\right) \left(\kappa_u^+ F e^{-ik_x^+ x} + \kappa_u^- G e^{-ik_x^- x} \right) \quad (5.55)$$

$$\hat{v}(x, y) = -i \sin\left(\frac{m}{R_m} y\right) \left(\kappa_v^+ F e^{-ik_x^+ x} + \kappa_v^- G e^{-ik_x^- x} \right) \quad (5.56)$$

where the circumferential acoustic velocity \hat{v} has a $\pi/2$ phase delay with respect to axial acoustic velocity \hat{u} . The waves F and G describing the 2D acoustic field in an annular duct are similar to the Riemann invariants f and g from

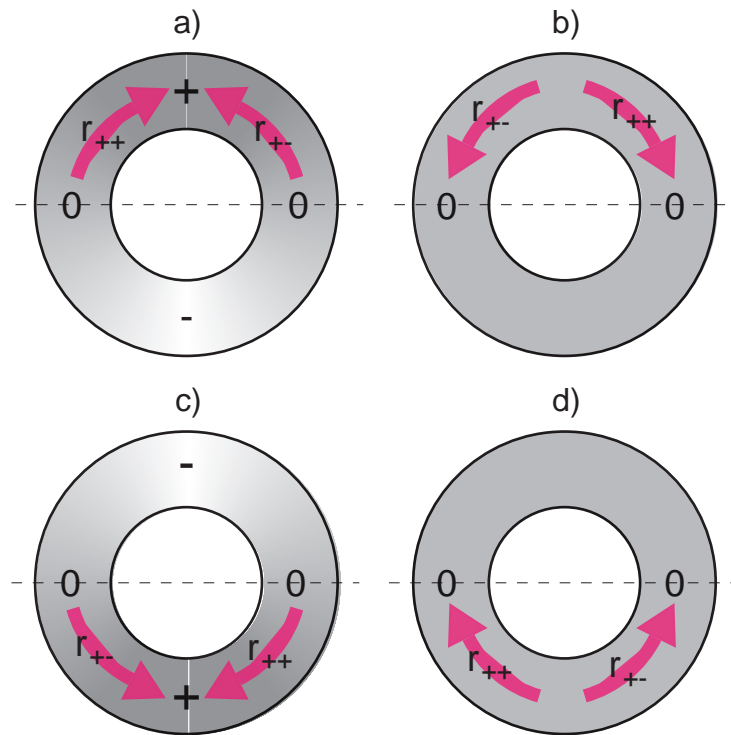


Figure 5.5: Schematic representation of a 1st order standing azimuthal mode ($m=1$) at phase 0 (a), $\pi/2$ (b), π (c) and $3\pi/2$ (d). Notation: + and - are antinodes in π phase delay and 0 the nodes

the 1D wave propagation (Chapter 5.3.2). For the particular case when the azimuthal mode index m is zero ($m = 0$), which corresponds to planar modes, Eqns. 5.54, 5.55 and 5.56 reduce to Eqns. 5.21 and 5.22 describing the 1D wave propagation. Here, the azimuthal velocity \hat{v} vanishes and the factors κ_u^+ and κ_u^- take the values 1 and -1, respectively.

When the complex amplitudes of the helical waves with different sense of rotation are not equal the azimuthal modes exhibit a spinning character. A pure spinning wave is characterized by rotating positions for the nodes and antinodes, as presented schematically in Fig. 5.6

The spinning components of \hat{p} , \hat{u} and \hat{v} are defined with respect to the positive and negative sense of rotation [19] in Eqns. 5.57 to 5.62.

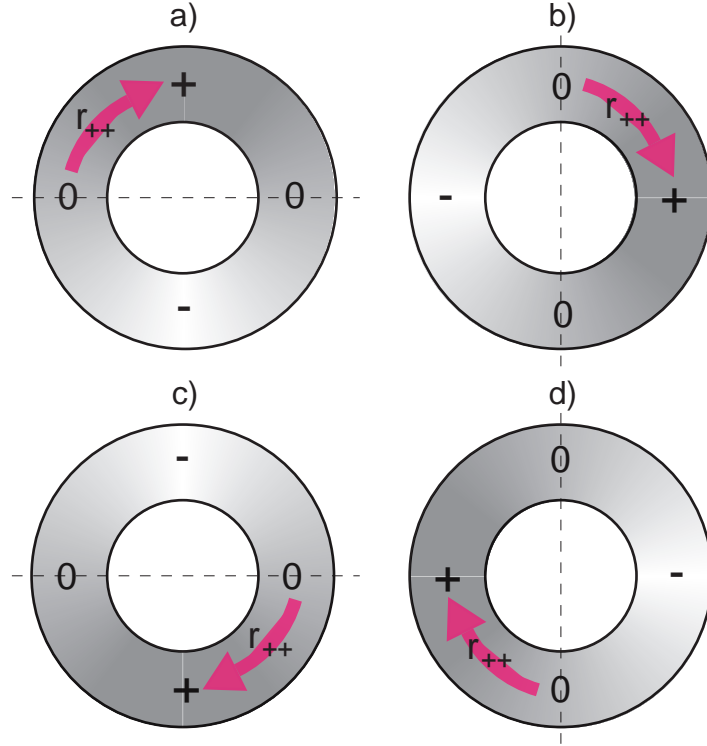


Figure 5.6: Schematic representation of a 1st order spinning azimuthal mode ($m=1$) at phase 0 (a), $\pi/2$ (b), π (c) and $3\pi/2$ (d). Notation: + and - are antinodes in π phase delay and 0 the nodes

$$\frac{1}{\bar{\rho}c} \hat{p}_{sp}^+(x, y) = e^{-ik_y^+ y} \left[(R_{++} - R_{+-}) e^{-ik_x^+ x} + (R_{-+} - R_{--}) e^{-ik_x^- x} \right] \quad (5.57)$$

$$\frac{1}{\bar{\rho}c} \hat{p}_{sp}^+(x, y) = -e^{-ik_y^- y} \left[(R_{++} - R_{+-}) e^{-ik_x^+ x} + (R_{-+} - R_{--}) e^{-ik_x^- x} \right] \quad (5.58)$$

$$\hat{u}_{sp}^+(x, y) = e^{-ik_y^+ y} \left[\kappa_u^+ (R_{++} - R_{+-}) e^{-ik_x^+ x} + \kappa_u^- (R_{-+} - R_{--}) e^{-ik_x^- x} \right] \quad (5.59)$$

$$\hat{v}_{sp}^+(x, y) = e^{-ik_y^+ y} \left[\kappa_v^+ (R_{++} - R_{+-}) e^{-ik_x^+ x} + \kappa_v^- (R_{-+} - R_{--}) e^{-ik_x^- x} \right] \quad (5.60)$$

$$\hat{u}_{sp}^-(x, y) = -e^{-ik_y^- y} \left[\kappa_u^+ (R_{++} - R_{+-}) e^{-ik_x^+ x} + \kappa_u^- (R_{-+} - R_{--}) e^{-ik_x^- x} \right] \quad (5.61)$$

$$\hat{v}_{sp}^-(x, y) = -e^{-i\bar{y}} \left[\kappa_v^+ (R_{++} - R_{+-}) e^{-ik_x^+ x} + \kappa_v^- (R_{-+} - R_{--}) e^{-ik_x^- x} \right] \quad (5.62)$$

A quantitative criteria for the assessment of the spinning character of an azimuthal mode m is the spin-ratio Δ_{sp}^m [19]

$$\Delta_{sp}^m = \frac{(1 - |\alpha_m|)^2}{1 + |\alpha_m|^2} \quad (5.63)$$

where α_m is the ratio of the complex modal amplitudes of the m^{th} order helical waves travelling in the clockwise R_{++} and anticlockwise R_{+-} sense of rotation:

$$\alpha_m = \frac{R_{+-}}{R_{++}} \quad (5.64)$$

Evesque et al. [19] have classified the azimuthal modes depending on the spinning character. For spin-ratios $\Delta_{sp}^m > 0.5$ the azimuthal modes are characterised as dominantly spinning and consequently for $\Delta_{sp}^m < 0.5$ as dominantly standing.

The spin ratio Δ_{sp} of the whole acoustic field can be determined with the method described above (Eqns. 5.63 and 5.64) if the acoustic field includes only the azimuthal mode m . In reality tough, the acoustic field of an annular combustor is a superposition of the system eigenmodes, including here 1st, 2nd and higher order azimuthal modes. Hence, the spin ratio Δ_{sp} of the whole acoustic field must determined with respect to each modal component. A method for this, which includes a modal decomposition procedure, has been developed in this work and is presented in detail in Chapter 7.

5.3.5 Eigenfrequencies of Thin Annular Ducts

The acoustic field of a thin annular duct can be composed of planar ($m = 0$) and non-planar modes ($m > 0$). The first category are axial modes where all circumferential positions oscillate in phase and phase differences arise only along the axial direction. For non-planar modes ($m > 0$) pure azimuthal and mixed modes can be distinguished. In the first case the waves propagate exclusively along the circumferential direction and all the axial positions oscillate in phase. For mixed modes both axial and azimuthal components are present.

The eigenfrequencies of a thin annular duct with fully reflective closed acoustic boundaries can be calculated with the following formula [16]:

$$f_{l,m} = \frac{c}{2\pi} \sqrt{\left(\frac{l\pi}{L}\right)^2 + \left(\frac{m}{R_m}\right)^2} \quad (5.65)$$

where $l, m = 0, 1, 2$ are the axial and azimuthal mode indexes and c the speed of sound. In Eqn. 5.65, the first term under the square root is the resonant axial component derived from the axial wavenumber k_x^\pm (Eqn. 5.45) and Eqn. 5.55. The second term is the azimuthal wavenumber defined in Eqn. 5.41. Eqn. 5.65 calculates the eigenfrequencies of pure axial modes for $m = 0$ and pure azimuthal modes for $l = 0$. When both parameters l and m are non-zero, Eqn. 5.65 calculates the eigenfrequencies of mixed modes. In Tab. 5.1 the eigenfrequencies of the axial and the first three pure azimuthal modes of a simple annular duct with the geometrical parameters resembling that of the annular combustion chamber ($L_{cc} = 279\text{mm}$ and $D_m = 437\text{mm}$, Chapter 4) are presented. The propagation medium is air at ambient temperature and atmospheric pressure.

Table 5.1: Eigenfrequencies of the isothermal annular duct

Mode[l, m]	[1, 0]	[0, 1]	[0, 2]	[0, 3]
$f_{l,m}$ [Hz]	615	250	500	750

5.4 Acoustic Damping

Acoustic damping influences directly the stability behaviour of a combustion system. According to Polifke et al. [50], three types of acoustic energy dissipation need to be considered for a gas turbine combustor:

- visco-thermal acoustic damping in boundary layers
- visco-thermal acoustic damping in the free field
- flow induced dissipation (at area discontinuities and trijunctions)

The visco-thermal acoustic damping in the free field is in general neglected. Hence, the types of acoustic damping which remain relevant for the work presented here are the visco-thermal damping in boundary layers and the flow induced dissipation. These are going to be presented in the following.

5.4.1 Visco-Thermal Damping in Boundary Layers

The acoustic damping due to the oscillation of the acoustic boundary layers needs to be considered only for *narrow tubes*, i.e. pipes with the length much larger than the hydraulic diameter. In a typical gas turbine, this concerns only the cooling channels for the combustion chamber walls whose lengths are about 100 times larger than the hydraulic diameter [50]. In modern low NO_x lean premixed combustors, the cooling air is used as reactant to achieve the lean premixed mode and therefore flows in the plenum chamber. The large volume of the plenum chamber produces the uncoupling of the cooling system from the acoustics in the combustion chamber and consequently the cooling channels do not produce acoustic damping. For the annular combustor test rig described in Chapter 4, the damping due to the oscillation of the acoustic boundary layers is also not relevant because the test rig does not have cooling channels. Furthermore, the condition for *narrow tubes* is not fulfilled, i.e. the mean diameter of the annulus is of the same order of magnitude with

the total length of the combustor. Consequently, it is assumed that in the annular combustor test rig, the acoustic damping is not influenced by the oscillation of the acoustic boundary layers. In this case the damping coefficient α , which describes the attenuation in the boundary layers in a turbulent flow, is similar to the damping coefficient in a quiescent fluid. Hence, the modelling of the acoustic damping in boundary layers in the annular combustor test rig has been followed with considering the damping coefficient α for a quiescent fluid.

The visco-thermal acoustic damping in boundary layers was investigated for quiescent fluids by Kirchhoff [29] in the 19th century. He solved the conservation equations for mass, momentum and energy for acoustic perturbations where viscous forces and heat conduction to the walls were considered. The outcome of this theoretical work was an analytical model of the wave number with damping effects. In a later work, Peters et al. [46] revised the theory from Kirchhoff and presented the results in a new formulation. The low-frequency approximation of the wavenumber applies for low Helmholtz numbers $ka \ll 1$ and for high shear numbers $Sh = d_h \sqrt{\frac{\omega}{\nu}} \gg 1$ and is presented in the following

$$k = \frac{\omega}{c} \left[1 + \frac{1-i}{\sqrt{2}} \frac{1}{Sh} \left(1 + \frac{\gamma-1}{\sqrt{Pr}} \right) - \frac{i}{Sh^2} \left(1 + \frac{\gamma-1}{\sqrt{Pr}} - \frac{1}{2} \gamma \frac{\gamma-1}{Pr} \right) \right] \quad (5.66)$$

where Pr is the Prandtl number. The parameters d_h , ω and ν are the hydraulic diameter, angular frequency and kinematic viscosity, respectively. In a more general formulation the wavenumber can be expressed as

$$k = \frac{\omega}{c} - i\alpha \quad (5.67)$$

where α is the damping coefficient. According to Eqn. 5.66 α equals:

$$\alpha = \frac{\omega}{c} \frac{1}{\sqrt{2}} \frac{1}{Sh} \left(1 + \frac{\gamma-1}{\sqrt{Pr}} \right) + \frac{i}{Sh^2} \left(1 + \frac{\gamma-1}{\sqrt{Pr}} - \frac{1}{2} \gamma \frac{\gamma-1}{Pr} \right) \quad (5.68)$$

5.4.2 Flow Induced Damping

The flow induced dissipation is the most important type of acoustic damping which occurs in gas turbine combustors [50] and is directly associated with the losses of fluid-mechanic energy due to friction inside the fluid. This effect occurs especially at regions of flow separation with vorticity generation occurring in elements like area discontinuities, orifices or acoustic junctions (Fig. 5.7). This damping effect is characterized by the total pressure drop across the element.

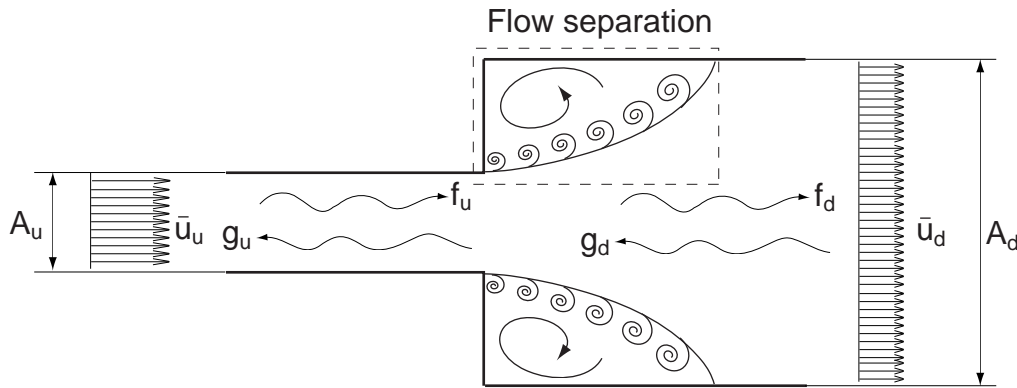


Figure 5.7: Flow induced acoustic dissipation in the regions of vorticity generation at an area expansion

The relations describing the acoustic damping are derived from the mass conservation equation (Eqn. 5.69) and the axial momentum balance (Eqn. 5.70)

$$[\rho Au]_u^d = 0 \quad (5.69)$$

$$\left[p + \frac{1}{2} \rho u^2 \right]_u^d + \frac{1}{2} \rho \zeta u_u^2 = 0 \quad (5.70)$$

where ζ is the pressure loss coefficient related to the upstream cross section (A_u). After linearising the flow parameters in Eqs. 5.69 and 5.70 in the stationary component and the fluctuating acoustic part (Eqs. 5.5, 5.6, 5.7) and re-

taining only the first order terms, the following equations for describing the acoustic wave propagation through the element are obtained:

$$\left[A \left(\hat{u} + \frac{\hat{p}}{\bar{\rho}c} M \right) \right]_u^d = 0 \quad (5.71)$$

$$\left[\frac{\hat{p}}{\bar{\rho}c} + M \hat{u} \right]_u^d + \zeta M_u \hat{u}_u = 0 \quad (5.72)$$

6 Acoustic Two Port Elements

The linear acoustic theory presented in Chapter 5 provides the basis for the introduction of the acoustic network modelling theory. As seen in Chapter 2, this method is applied widely at present for studying the dynamic behaviour of industrial gas turbines. The development of this method has been pioneered by Munjal [40]. He has shown that in the plane wave regime, where the acoustic wavelengths are much longer than the geometrical dimensions and thereby the acoustic variables pressure p' and velocity u' are assumed to be constant over the cross-section, the test elements can be described as acoustic two-ports. Hence, the acoustic states upstream and downstream of the test element are related by means of simple relations from the linear acoustic theory presented in Chapter 1. By combining acoustic elements together in a network, complex acoustic systems can be represented. The acoustic network model created in this way can be used for simulation and stability analysis purposes as reported in [28], [32], [4], [44], [53], [9], [56], [10], [11], [30] and [58]. The modular character of an acoustic network provides great flexibility in using different modelling techniques. A widespread approach is to combine pure theoretical modelling with experimental measurements or with analytical modelling solutions derived from experimental results. The theoretical solutions are often sufficient for simple elements like ducts or area changes. The experimental solutions are used in general for representing more complicated elements like burners and flames because for these no general theoretical representation is available. The analytical solutions derived from experimental results are referred to in general as hybrid methods and are used as well for representing complicated acoustic elements like burners and flames. These consist in describing the dynamic characteristics of two ports with analytical models validated with experimental data. In the following section a brief introduction in the acoustic two ports theory is given. The focus lies here on the relevant forms of acoustical two ports and on the methods used for the direct

experimental evaluation. In the last section the most frequently used analytical solutions for two port elements are presented.

A two port element is a linear system used frequently in disciplines like acoustics, electrical engineering or quantum mechanics to relate the input and output states of a test element, as presented schematically in Fig. 6.1.

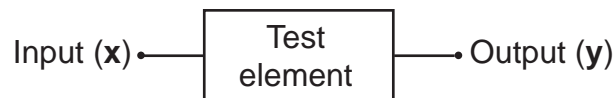


Figure 6.1: Schematic representation of a two port element

The mathematical representation of a linear time invariant two port element is given in the frequency domain by:

$$\mathbf{y} = \mathbf{H}\mathbf{x} \quad (6.1)$$

where \mathbf{H} is the two port transfer function relating the input \mathbf{x} to the output \mathbf{y} .

In acoustics a two port relates the acoustic fields upstream and downstream of the test element as presented schematically in Fig. 6.2. In the case of an 1D duct, the acoustic field is characterized in the frequency domain by the parameters pressure \hat{p} and velocity \hat{u} , or the Riemann invariants f and g (see Chapter 5). Then, the two port transfer function \mathbf{H} is a 2×2 matrix also referred to in literature as *four pole* element. For a thin annular duct, the acoustic velocity has beside the axial component \hat{u} also a azimuthal component \hat{v} (see Fig. 6.3).

In the framework presented here, the 2D acoustic field of the annular combustor is characterised by azimuthal modes with a predominantly standing character (Chapter 8.1). Hence, the shape of the mode in circumferential direction is described analytically (Eqns. 5.54, 5.55 and 5.56) and the acoustic characterisation reduces to the determination of the two variables F and G . Consequently, the acoustic modelling of a thin annular duct can be approached,



Figure 6.2: Schematic representation of an acoustic two port of an 1D duct. Indices u and d denote the upstream and downstream sides of the duct respectively

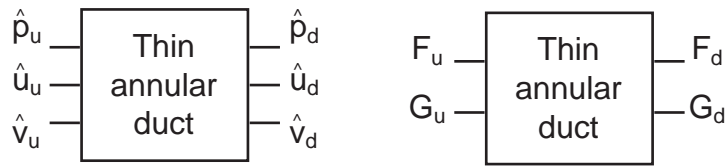


Figure 6.3: Schematic representation of an acoustic two port of a thin annular duct. Indices u and d denote the upstream and downstream sides of the duct respectively

similarly to the 1D plane case, with the two port theory and represented by 2×2 transfer matrices. Representations like this are often preferred in practical applications and results have been reported frequently in [4], [11], [9], [30] and [56].

6.1 Equivalent Forms of Acoustic Two Port Matrices

The two port transfer function of acoustic elements \mathbf{H} is a 2×2 matrix relating the upstream and downstream state vectors. Depending on the definition of the state vectors, the two port matrix can be represented in different forms. The most commonly used forms are the *transfer matrix* and the *scattering matrix*. In this work the *transfer matrix* representation is preferred and is presented in the following. The *transfer matrix*, denoted in the following with \mathbf{T} , relates the acoustic variables pressure \hat{p} and velocity \hat{u} or the Riemann invariants f and g across the test element

$$\begin{pmatrix} \frac{\hat{p}}{\bar{\rho}c} \\ \hat{u} \end{pmatrix}_d = \underbrace{\begin{pmatrix} T_{11} & T_{12} \\ T_{21} & T_{22} \end{pmatrix}}_{\mathbf{T}_{pu}} \begin{pmatrix} \frac{\hat{p}}{\bar{\rho}c} \\ \hat{u} \end{pmatrix}_u \quad (6.2)$$

and, respectively

$$\begin{pmatrix} f \\ g \end{pmatrix}_d = \underbrace{\begin{pmatrix} T_{11} & T_{12} \\ T_{21} & T_{22} \end{pmatrix}}_{\mathbf{T}_{fg}} \begin{pmatrix} f \\ g \end{pmatrix}_u. \quad (6.3)$$

In Eqs. 6.2 the acoustic pressure \hat{p} is normalized with the characteristic impedance $\bar{\rho}c$ of the medium in order to have non-dimensional elements. In general, the *transfer matrix* representation is suitable for acoustic two port elements combined in a linear configuration. The transformation relations between the (pu) and the (fg) formulations can be easily derived from the Eqs. 5.24 and 5.25 presented in Chapter 5. According to Fischer [22] and Abom [2] these are

$$\mathbf{T}_{fg} = \Omega \cdot \mathbf{T}_{pu} \cdot \Omega^{-1} \quad (6.4)$$

and, respectively

$$\mathbf{T}_{pu} = \Omega^{-1} \cdot \mathbf{T}_{fg} \cdot \Omega \quad (6.5)$$

where Ω is

$$\Omega = \frac{1}{2} \begin{pmatrix} 1 & 1 \\ 1 & -1 \end{pmatrix} = \frac{1}{2} \Omega^{-1}. \quad (6.6)$$

6.2 Direct Experimental Evaluation

The first experimental evaluations of two port transfer matrices were made in the early 70s and were concentrated mostly on the dynamic characterization of simple flow elements and acoustic boundaries. Since then, the methods were continuously developed. This has been made possible also due to the improvement and the accessibility of multi channel high speed measurement and data post processing techniques. A summary of these works is presented in [2].

In principle, the methods consist of acoustic measurements in 1D ducts with an external excitation source. The system is forced and the acoustic response is measured in terms of the acoustic pressure p' with multi channel data acquisition systems. The excitation types most frequently used are periodic mono frequent signals with a constant amplitude in time ([2], [6], [45], [57]). To et al. [60], [61] have used multi frequent transient signals for their investigations.

The evaluation of the four parameters of the acoustic transfer matrix \mathbf{T}_{fg} requires four equations and thereby two sets of state vectors $(f, g)_u$ and $(f, g)_d$. The state vectors are determined experimentally and need to be linearly independent to ensure a good evaluation result. The experimental methods, which have been mostly used for the determination of the state vectors, are the *two load method*, the *two source location method* and the *two source method*. From these, the most stable approach was proven to be the *two source location method* ([3]) which ensure always the linear independence of the state vectors.

The *two source location method* was introduced in the field of aero-acoustics by Munjal [41]. The experimental set-up is described schematically in Fig. 6.4. Positions 1, 2, 3 and 4 are the axial planes where the acoustic pressure is measured. The two acoustic independent states a and b are generated by switching the position of the sound source between the upstream and downstream sides of the test element with keeping the rest of the system unchanged.

An extension of the *two source location method* is the *two source location*,

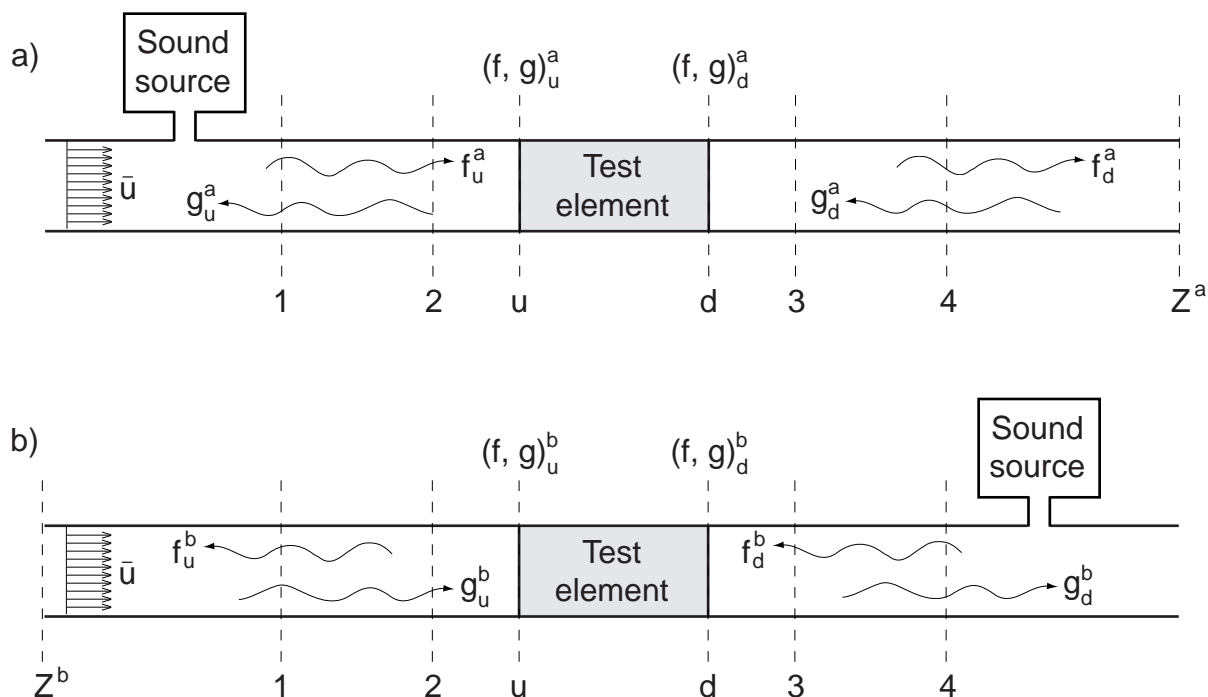


Figure 6.4: Schematic representation of the experimental set-up of the *two source location method* for a 1D duct with a mean flow of velocity \bar{u} . Superscripts a and b denote the two acoustic states generated by switching the position of the sound source between the upstream and downstream sides of the test element

multi microphone method presented by Paschereit et al. [45]. Here, the number of measurement points for the acoustic pressure p' has been extended to more than four. This is required especially for acoustic measurements in combustion chambers where the signal-to-noise ratio is relatively low. The higher number of measurement points has a positive effect on the determination of the state vectors and thereby on the evaluation of the transfer matrix elements.

Alemela et al. [6] have used the *two source location, multi microphone method* for measuring the dynamic characteristics of lean premixed flames in the single burner combustor test rig at Lehrstuhl für Thermodynamik and have shown that six measurement points are sufficient to obtain very good results. The direct application of this method on the annular combustor test rig pre-

sented in Chapter 4 requires a much larger number of measurement points and thereby dynamic pressure transducers. This would transform the measurement activity in a laborious project with high experimental efforts and financial costs. A crude evaluation of the minimum number of dynamic pressure sensors required is presented in Chapter 7. Hence, a new method has been developed which allows the measurement of the dynamic characteristics of lean premixed flames in the annular combustion chamber with a reduced the number of dynamic pressure transducers. This method is presented in detail in Chapter 7.

6.3 Analytical Transfer Matrices

This section presents analytical models of acoustic elements which are relevant to the actual work. These can be distinguished in pure theoretical models and models which are developed based on experimental validation. The pure theoretical models are universally applicable and can be adopted to describe the dynamic behaviour of simple acoustic elements like ducts and area discontinuities. The models which are developed based on experiments validation are used for describing the dynamic behaviour of more complex acoustic elements like burners and flames.

6.3.1 Duct with Constant Cross-Section

The acoustic wave propagation in a duct segment with a mean flow velocity \bar{u} , length L and constant cross-section is presented schematically in Fig. 6.5. The analytical transfer matrix of the duct segment is derived from the basic acoustic relations presented in Chapter 5. In Fig. 6.5 the waves f_u and g_u are the Riemann invariants which propagate upstream of the duct segment. Further, the waves f_d and g_d are the Riemann invariants which propagate downstream of the duct segment. The transfer matrix \mathbf{T} relates the Riemann invariants f and g at the axial planes upstream (u) and downstream (d) of the duct segment considered.

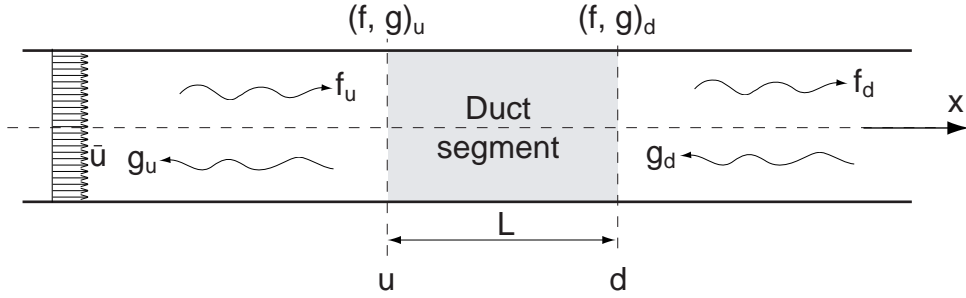


Figure 6.5: Schematic representation of a generic duct of length L and constant cross-section; u and d denote the axial positions of the upstream and downstream reference planes respectively

The transfer matrix in (fg) notation is:

$$\begin{pmatrix} f \\ g \end{pmatrix}_d = \underbrace{\begin{pmatrix} e^{-ik_x^+ L} & 0 \\ 0 & e^{-ik_x^- L} \end{pmatrix}}_{\mathbf{T}_{fg}} \begin{pmatrix} f \\ g \end{pmatrix}_u \quad (6.7)$$

The transfer matrix in the pu notation can be easily deduced from Eqn. 6.7 by applying the transformation rules from Eqns. 6.5 and 6.4. In Eqn. 6.7, k_x^\pm is the axial wavenumber defined in Eqn. 5.23 for a 1D wave propagation. For a 2D wave propagation in thin annular ducts, the axial wavenumber k_x^\pm is defined in Eqn. 5.45.

When the visco-thermal acoustic damping in boundary layers (Chapter 5.4.1) is considered, the axial wavenumber k_x^\pm is complex and is defined as in Eqns. 5.66 and 5.67. The imaginary part of k_x^\pm is the damping coefficient α (Eqn. 5.68) which describes the decrease of the modal amplitude in the direction of propagation. For the 2D acoustic wave propagation in thin annular ducts, the damping coefficient α is applied also as imaginary part to the axial wavenumber k_x^\pm defined in Eqn. 5.45.

6.3.2 Compact Element with Losses

This model describes the transfer matrix of acoustic elements which are characterised by a relatively complex 3D geometry and generate acoustic losses. In the acoustic model of the annular combustor (Chapter 7) this element was used to describe the transfer matrix of the EV5 burner. The complex geometry of the swirler has an impact on the local pattern of the acoustic field [17], i.e. curvature of the wave front and excitation of higher order evanescent waves. These produce a change in phase and therefore in the thermo-acoustic eigenfrequencies of the system. To account for these, the model includes the effective length l_{eff} and the reduced length l_{red} which describe the capacitance and the inductance effects. The expansion of the swirling jet of the burner into the combustion chamber yields the flow separation at the burner edge with the formation of the outer recirculation zone (ORZ). Hence, this region is characterised by aerodynamic losses generated by the dispersion of the fluid-mechanic energy through viscous forces. The acoustic losses thus generated are accounted for in the model by the pressure loss coefficient ζ .

The starting equations for deriving the analytical transfer matrix of the element are the mass conservation and axial momentum balance equations (Eqns. 5.71 and 5.72) presented in Chapter 5.4.2. After linearisation around the mean quantities and retaining only the first order terms these become [25]

$$\left[A \left(\hat{u} + \frac{\hat{p}}{\bar{\rho}c} M \right) \right]_u^d + i \frac{\omega}{c} l_{red} A_d \left(\frac{\hat{p}}{\bar{\rho}c} \right)_u = 0 \quad (6.8)$$

and, respectively

$$\left[\frac{\hat{p}}{\bar{\rho}c} + M \hat{u} \right]_u^d + \zeta M_u \hat{u}_u + i \frac{\omega}{c} \hat{u}_u l_{eff} = 0. \quad (6.9)$$

where the pressure loss coefficient ζ is related to the upstream cross-section A_u .

By rewriting Eqs. 6.8 and 6.9 and after neglecting the 2nd order terms contain-

ing acoustic variables and Mach number, the analytical transfer matrix form is obtained

$$\begin{pmatrix} \frac{\hat{p}}{\hat{\rho}c} \\ \hat{u} \end{pmatrix}_d = \underbrace{\begin{pmatrix} 1 & \left[1 - \zeta - \left(\frac{A_u}{A_d}\right)^2\right] M_u - i\frac{\omega}{c} l_{eff} \\ -i\frac{\omega}{c} l_{red} & \frac{A_u}{A_d} \end{pmatrix}}_{\mathbf{T}_{pu}} \begin{pmatrix} \frac{\hat{p}}{\hat{\rho}c} \\ \hat{u} \end{pmatrix}_u \quad (6.10)$$

where the subscripts u and d denote the upstream and downstream sides of the element.

6.3.3 Premixed Flames

Turbulent premixed flames are treated in the acoustic network modelling theory as flow discontinuities with heat addition as shown in Fig. 6.6.

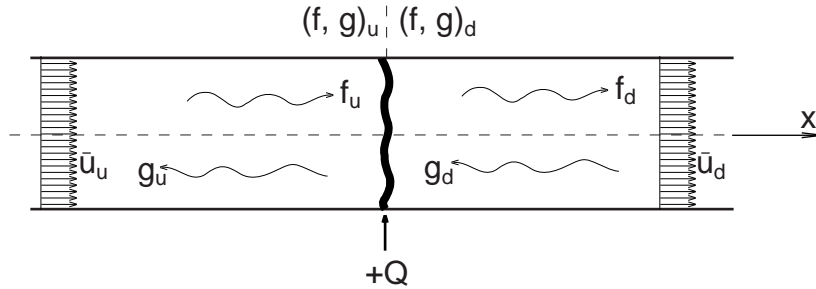


Figure 6.6: Schematic representation of a flame as a flow discontinuity with heat input Q

A thermo-acoustic model of the flame in a compressible and ideal gas was derived by Chu et al. [13] from the conservation equations for mass, momentum and energy and is expressed by the Rankine-Hugoniot relations

$$\frac{p_d}{p_u} = 1 - (\gamma - 1) \frac{q}{\rho_u u_u} M_u^2 \quad (6.11)$$

and

$$\frac{u_d}{u_u} = 1 + \frac{\gamma - 1}{\gamma} \frac{q}{\rho_u u_u} \quad (6.12)$$

where γ is the rate of specific heats and q the specific heat input from the flame on the unit area. An acoustic wave travelling through the flame front produces a change of the flow variables. These can be deduced from Eqs. 6.11 and 6.12 by linearising the flow variables pressure p and velocity u in terms of the mean value and a fluctuating component as described in [57]. Hence, Eqns. 6.11 and 6.12 become

$$p'_d = p'_u - \left(\frac{T_d}{T_u} - 1 \right) \bar{\rho}_u \bar{u}_d^2 \left(\frac{u'_u}{\bar{u}_u} + \frac{Q'}{\bar{Q}} \right) \quad (6.13)$$

and, respectively

$$u'_d = u'_u + \left(\frac{T_d}{T_u} - 1 \right) \bar{u}_u^2 \left(\frac{Q'}{\bar{Q}} - \frac{p'_u}{\bar{p}_u} \right) \quad (6.14)$$

where Q' and \bar{Q} are the fluctuation component and mean quantity of the integral heat release Q . Eqns. 6.13 and 6.14 couple the acoustic fields upstream and downstream of the flame. As it can be seen, this coupling depends on the heat release fluctuation Q' , which must be determined in order to close the system of equations. In the frequency domain, the heat release fluctuation \hat{Q} is related with the acoustic velocity in the burner \hat{u} through the flame transfer function (FTF):

$$FTF(\omega) = \frac{\hat{Q}/\bar{Q}}{\hat{u}_b/\bar{u}_b} \quad (6.15)$$

The flame transfer matrix (FTM) is obtained by inserting the flame transfer function in Eqns. 6.13 and 6.14 as

$$\begin{pmatrix} \frac{p'}{\bar{\rho}c} \\ u' \end{pmatrix}_d = \underbrace{\begin{pmatrix} \beta & -\beta \left(\frac{T_d}{T_u} - 1 \right) M_u (1 + FTF(\omega)) \\ -\left(\frac{T_d}{T_u} - 1 \right) \gamma M_u & 1 + FTF(\omega) \end{pmatrix}}_{\mathbf{T}_{pu}} \begin{pmatrix} \frac{p'}{\bar{\rho}c} \\ u' \end{pmatrix}_u \quad (6.16)$$

with $\beta = \bar{\rho}_u c_u / \bar{\rho}_d c_d$ is the ratio of the specific impedances. Thus, the determination of the FTM reduces to the determination of the FTF. Due to its complexity the FTF is determined experimentally ([6], [23], [27], [34], [55]) by measuring the flame response Q' to the acoustic velocity fluctuation in the burner u'_b .

A different approach for determining the FTF was proposed by Schuermans et al. [57] [55]. They developed an analytical model for the FTF (Eqn. 6.17) based on the time-lag formulation used by Crocco et al. [14] for investigating combustion instabilities in rocket engines:

$$FTF(\omega) = \frac{n}{\left(\frac{T_d}{T_u} - 1 \right)} \left(e^{-i\omega\tau - \frac{1}{2}\omega^2\sigma^2} - e^{-i\omega\tau_\phi - \frac{1}{2}\omega^2\sigma_\phi^2} \right) \quad (6.17)$$

The flame transfer function (Eqn. 6.17) has parameters which characterize the convective transport of the mixture fluctuations at the burner outlet and of the equivalence ratio waves. Thereby, the parameter τ is the mean convective time delay of the flow rate fluctuations and τ_ϕ the mean convective time delay of the equivalence ratio waves. The parameters σ and σ_ϕ characterise the width of the normal distributions, respectively. In case of a perfectly premixed flame the term describing the propagation of equivalence ratio waves vanishes:

$$FTF(\omega) = \frac{n}{\left(\frac{T_d}{T_u} - 1 \right)} e^{-i\omega\tau - \frac{1}{2}\omega^2\sigma^2} \quad (6.18)$$

The parameter n in Eqs. 6.17 and 6.18 is the interaction coefficient and describes the increase in the acoustic velocity due to the volume expansion. In

the case of a flame with fixed axial position ($\sigma = 0$), the interaction coefficient n is defined as:

$$n = \left(\frac{T_d}{T_u} - 1 \right) \quad (6.19)$$

Eqns. 6.18 and 6.19 show that the amplitude of the FTF model tends to unity for frequencies tending to zero ($\omega \rightarrow 0$). This is due to the fact that in the stationary regime ($\omega \rightarrow 0$) the variation of flame heat release (Q') is produced exclusively by the variation of the burner flow rate (u'). This agrees with the experimental determinations of the FTF presented in [6], [5], [23].

In the case of the axially distributed flame ($\sigma > 0$) expressed by Eqn. 6.18, the interaction coefficient is [5]

$$n = n_c \cdot \left(\frac{T_h}{T_c} - 1 \right) \quad (6.20)$$

where T_c and T_h are the preheating temperature and the adiabatic flame temperature, respectively. The factor n_c is defined as:

$$n_c(\tau, \sigma) = \frac{1}{\int_{t=0}^{t=\tau_{max}} \Phi_{\tau, \sigma^2}(t) dt} \quad (6.21)$$

$$= \frac{1}{\frac{1}{2} \left[\text{Erf} \left(\frac{\tau}{\sigma} \frac{\tau_{max}^{\tau-1}}{\sqrt{2}} \right) + \text{Erf} \left(\frac{\tau}{\sqrt{2}\sigma} \right) \right]} \quad (6.22)$$

In Eqn. 6.22, τ and τ_{max} are the mean and the maximum convective time delays, respectively. According to Alemela [5], the factor n_c accounts for the discrepancies between the value of the free parameter n determined through regression on the experimental data and the theoretical value (Eqn. 6.19). The flame model presented in Eqn. 6.18 assumes the reaction zone to have a Gaussian distribution σ . In reality though, the flame exhibits a finite distribution $[\tau_{min}, \tau_{max}]$. Hence, the missing area resulted after integrating the

probability density function (PDF(σ)) of the σ distribution on the finite domain $[\tau_{min}, \tau_{max}]$ is accounted for by the multiplication factor n_c .

With the analytical flame models presented in Eqns. 6.17 and 6.18, the determination of the FTF and FTM reduces to the experimental evaluation of the free model parameters n , τ , σ , τ_ϕ and σ_ϕ .

6.3.4 Acoustic Uncoupling Element

The acoustic uncoupling element models the transition from a 2D to a 1D acoustic wave propagation and vice-versa [16]. In the acoustic model of the annular combustor (Chapter 7), this element was used, in combination with other elements, to describe the transfer matrices of hardware components where the multi-dimensional character of the acoustic field changes. The 2D→1D transition occurs from the annular plenum chamber to the burner and from the annular combustion chamber to the exit nozzles (see Fig. 6.7). The backwards transition (1D→2D) is located at the interface between the burner and the annular combustion chamber. The uncoupling element allows only the propagation of plane waves ($k_y = 0$) in the burner and the exit nozzle, respectively. Evesque et al. [18] has shown that for the modelling of the burner, this solution delivers better results than the case when the propagation of azimuthal waves is considered [58].

The acoustic uncoupling relations along the annular circumference for a 2D→1D transition include the conditions for the acoustic pressure \hat{p} and velocity \hat{u} :

$$\frac{1}{\bar{\rho}_{pl}c_{pl}}\hat{p}_{pl}(x, y) = \cos\left(\frac{m}{R_m}y\right)(F_{pl} + G_{pl}) = f_b + g_b = \frac{1}{\bar{\rho}_bc_b}\hat{p}_b(x) \quad (6.23)$$

$$\hat{u}_{pl}(x, y) = \cos\left(\frac{m}{R_m}y\right)(\kappa_u^+F_{pl} + \kappa_u^-G_{pl}) = f_b - g_b = \hat{u}_b(x) \quad (6.24)$$

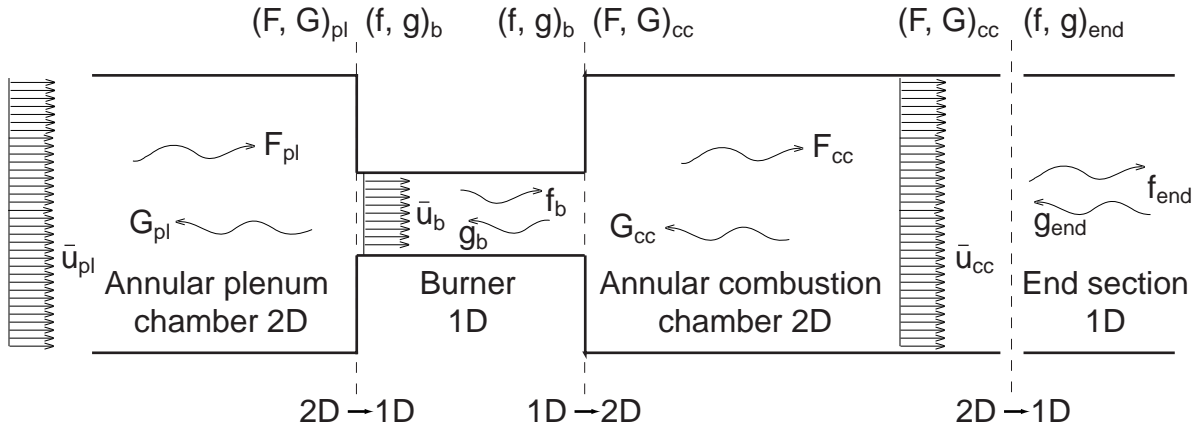


Figure 6.7: The uncoupling element describes the transition from the 2D acoustic field of the annular plenum chamber to 1D acoustic field of the burner and the transition from the 1D acoustic field of the burner section to the 2D acoustic field of the annular combustion chamber

For the 1D→2D transition these relations are:

$$\frac{1}{\bar{\rho}_b c_b} \hat{p}_b(x) = f_b + g_b = \cos\left(\frac{m}{R_m} y\right) (F_{cc} + G_{cc}) = \frac{1}{\bar{\rho}_{cc} c_{cc}} \hat{p}_{cc}(x, y) \quad (6.25)$$

$$\hat{u}_b(x) = f_b - g_b = \cos\left(\frac{m}{R_m} y\right) (\kappa_u^+ F_{cc} + \kappa_u^- G_{cc}) = \hat{u}_{cc}(x, y) \quad (6.26)$$

The plenum-burner interface consists physically of an area contraction (see Fig. 6.7). In the acoustic model of the annular combustor (Chapter 7.2), this interface was modelled with an acoustic uncoupling element $\mathbf{T}_{\text{uncoupling}}$ followed by an area change $\mathbf{T}_{\text{area change}}$ without acoustic losses. For $\mathbf{T}_{\text{area change}}$ the transfer matrix of the compact element (Eqn. 6.10) was used, where the pressure loss coefficient and the reduced length have been set to zero ($\zeta = 0$, $l_{red} = 0$). The effective length l_{eff} has been kept to account for the 3D acoustic effects at the area jump [17]. If the relations for the acoustic uncoupling element (Eqns. 6.23 and 6.24) and for the area change element are related at the reference

circumferential position $y = 0$, the transfer matrix of the plenum-burner interface becomes

$$\begin{pmatrix} \frac{\hat{p}}{\hat{\rho}c} \\ \hat{u} \end{pmatrix}_b = \underbrace{\begin{pmatrix} 1 & 0 \\ \frac{\kappa_u^+ + \kappa_u^-}{2} & \frac{\kappa_u^+ - \kappa_u^-}{2} \end{pmatrix}}_{\mathbf{T}_{\text{uncoupling 2D} \rightarrow \text{1D}}} \underbrace{\begin{pmatrix} 1 & -i\frac{\omega}{c}l_{eff} \\ 0 & \frac{A_{pl}}{A_b} \end{pmatrix}}_{\mathbf{T}_{\text{area change}}} \begin{pmatrix} \frac{\hat{p}}{\hat{\rho}c} \\ \hat{u} \end{pmatrix}_{pl} \quad (6.27)$$

where additionally, the reference Mach number corresponding to the plenum chamber has been neglected ($M_u = M_{pl} \cong 0$) as its value is in general very small.

The interface between the annular combustion chamber and the end section (Fig. 6.7) was modelled as a simple 2D \rightarrow 1D uncoupling condition using the transfer matrix $\mathbf{T}_{\text{uncoupling 2D} \rightarrow \text{1D}}$ from Eqn. 6.27.

The interface burner-combustion chamber is physically an area expansion (see Fig. 6.7) characterised by acoustic losses (Chapter 5.4.2). In the acoustic model of the annular combustor, this interface was modelled as a compact element with losses (Chapter 6.3.2) followed by an acoustic uncoupling element for a 1D \rightarrow 2D transition (Eqns. 6.25 and 6.26). The analytical transfer matrix of the burner-combustion chamber interface at the reference circumferential position $y = 0$ is

$$\begin{pmatrix} \frac{\hat{p}}{\hat{\rho}c} \\ \hat{u} \end{pmatrix}_{cc} = \underbrace{\begin{pmatrix} 1 & \left[1 - \zeta - \left(\frac{A_b}{A_{cc}}\right)^2\right] M_b - i\frac{\omega}{c}l_{eff} \\ -i\frac{\omega}{c}l_{red} & \frac{A_b}{A_{cc}} \end{pmatrix}}_{\mathbf{T}_{1-\zeta}} \underbrace{\begin{pmatrix} 1 & 0 \\ -\frac{\kappa_u^+ + \kappa_u^-}{\kappa_u^+ - \kappa_u^-} & \frac{2}{\kappa_u^+ - \kappa_u^-} \end{pmatrix}}_{\mathbf{T}_{\text{uncoupling 1D} \rightarrow \text{2D}}} \begin{pmatrix} \frac{\hat{p}}{\hat{\rho}c} \\ \hat{u} \end{pmatrix}_b \quad (6.28)$$

where the pressure loss coefficient ζ is related to the upstream cross-section of the burner A_b .

6.3.5 Acoustic Junction Element

The acoustic junction element describes an acoustic bifurcation where an incident acoustic wave separates in two outgoing waves. In the acoustic model of the annular combustor, this element was used to describe the end section of the combustion chamber (see Fig. 6.8). This includes the excitation module with the speaker element and the exit acoustic boundary (exit nozzle).

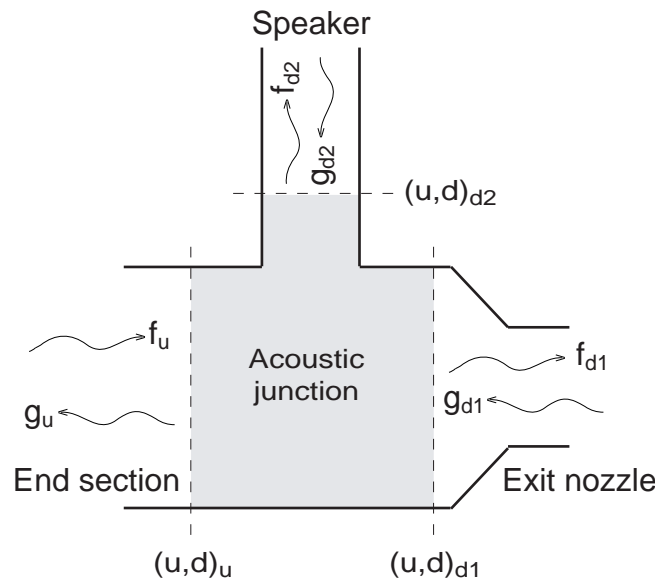


Figure 6.8: Schematic representation of the acoustic junction element; u denotes the upstream side and $d1, d2$ the downstream branches

The transfer matrix of the element is derived from the mass and momentum balance equations (Eqns. 5.69 and 5.70). For simplification reasons, the acoustic losses of the junction element have been neglected. After linearisation and exclusion of the second order terms, the mass and momentum balance equations become:

$$\left[A \left(\hat{u} + \frac{\hat{p}}{\bar{\rho}c} M \right) \right]_u = \left[A \left(\hat{u} + \frac{\hat{p}}{\bar{\rho}c} M \right) \right]_{d1} + \left[A \left(\hat{u} + \frac{\hat{p}}{\bar{\rho}c} M \right) \right]_{d2} \quad (6.29)$$

$$\left[\frac{\hat{p}}{\bar{\rho}c} + M\hat{u} \right]_u = \left[\frac{\hat{p}}{\bar{\rho}c} + M\hat{u} \right]_{d1} \quad (6.30)$$

$$\left[\frac{\hat{p}}{\bar{\rho}c} + M\hat{u} \right]_u = \left[\frac{\hat{p}}{\bar{\rho}c} + M\hat{u} \right]_{d2} \quad (6.31)$$

From Eqns. 6.29, 6.30 and 6.31, the transfer matrix form of the acoustic junction element is obtained:

$$\begin{aligned} \begin{pmatrix} \frac{\hat{p}}{\bar{\rho}c} \\ \hat{u} \end{pmatrix}_{d1} &= \begin{pmatrix} 1 & M_u - M_{d1} \frac{A_u}{A_{d1}} \\ \frac{A_u}{A_{d1}} M_u - M_{d1} & \frac{A_u}{A_{d1}} \end{pmatrix} \begin{pmatrix} \frac{\hat{p}}{\bar{\rho}c} \\ \hat{u} \end{pmatrix}_u \\ &+ \begin{pmatrix} 0 & M_{d1} \frac{A_{d2}}{A_{d1}} \\ -\frac{A_{d2}}{A_{d1}} M_{d2} & -\frac{A_{d2}}{A_{d1}} \end{pmatrix} \begin{pmatrix} \frac{\hat{p}}{\bar{\rho}c} \\ \hat{u} \end{pmatrix}_{d2} \end{aligned} \quad (6.32)$$

$$\begin{aligned} \begin{pmatrix} \frac{\hat{p}}{\bar{\rho}c} \\ \hat{u} \end{pmatrix}_{d2} &= \begin{pmatrix} 1 & M_u - M_{d2} \frac{A_u}{A_{d2}} \\ \frac{A_u}{A_{d2}} M_u - M_{d2} & \frac{A_u}{A_{d2}} \end{pmatrix} \begin{pmatrix} \frac{\hat{p}}{\bar{\rho}c} \\ \hat{u} \end{pmatrix}_u \\ &+ \begin{pmatrix} 0 & M_{d2} \frac{A_{d1}}{A_{d2}} \\ -\frac{A_{d1}}{A_{d2}} M_{d1} & -\frac{A_{d1}}{A_{d2}} \end{pmatrix} \begin{pmatrix} \frac{\hat{p}}{\bar{\rho}c} \\ \hat{u} \end{pmatrix}_{d1} \end{aligned} \quad (6.33)$$

7 Method Development

The determination of the BTM and FTM in the annular combustor with the methods described in Chapter 6.2 requires a large number of simultaneous measurements of the acoustic pressure p' and thereby dynamic pressure transducers. According to Kunze [33] and Fischer [22], a number of approximately 40 dynamic pressure transducers are necessary. This would turn the experimental activity in a very cumbersome task if considered only the time needed for calibrating such a large number of sensors (Chapter 4.3.1). Furthermore, the financial effort for purchasing the measurement technique including here the sensors and the additional equipment would be very large.

A simplification of this problem was possible due to the low spinning tendency of the acoustic field, i.e. the azimuthal modes have a predominantly standing character. This was shown after the preliminary acoustic measurements made on the cold isothermal flow, which are presented in Chapter 8.1. Hence, the acoustic pressure field of the annular combustor can be described in a simplified form with only 2 unknowns F and G , as in Eqns. 5.54, 5.55 and 5.56.

The standing character of the azimuthal modes opened the way for the development of a new method for the determination of the BTM and FTF in the annular combustor. The new method is called *model based method* and is a combination of both theoretical modelling and experimental investigations. The new method comprises the modelling of the acoustic system based on the linear acoustic two port theory (Chapter 6) followed by validation with experimental data. An important advantage in using the acoustic network modelling is the possibility of applying physical constraints to the acoustic system like standing azimuthal modes and defined acoustic boundaries. This has the positive effect of reducing the degrees of freedom which results that the experimental characterisation of the acoustic field needed for the model validation

is required in only two axial planes in the combustion chamber and plenum, respectively. The experimental characterisation in an axial plane is performed by measuring the acoustic pressure p' at several locations along the annular circumference. Further, by applying a modal decomposition method on the measured data, the modal components of the acoustic field are extracted and used for the validation of the acoustic model. With the *model based method* the number of dynamic pressure sensors required for the determination of the BTM and FTF in the annular combustor reduces significantly.

The central parts of the acoustic model of the annular combustor are the burner and flame models. The validation of the burner model (BTM) is made in a first phase with experimental data measured with the cold isothermal flow. Then, in a second phase, the FTF model is validated with experimental data measured in the annular combustor with flame. The results are presented in detail in Chapter 8 together with the corresponding conclusions and comments.

The modal decomposition and analysis method is presented in the following section and in the last part of this chapter the acoustic network model of the annular combustor is described in detail.

7.1 Modal Decomposition Method

The modal decomposition method has been developed to identify and extract the modal components of the acoustic field from simultaneously measured dynamic pressures. This technique was introduced by Abom [1] who investigated the multi-dimensional acoustic field of a simple duct with circular cross-section. More recently, Mastrovito et al. [38] have applied successfully a similar approach to identify the unstable acoustic modes in a full scale annular combustion chamber. Based on these, Ettner [16] developed a modal decomposition method to study the acoustic field of the annular combustor test rig at Lehrstuhl für Thermodynamik of TU München. As in [38], the method relies on the simultaneous multipoint measurements of the acoustic pressure with dynamic pressure transducers. The sensors are mounted on the outer

wall of the combustor (see Fig. 7.1) at the same axial position and distributed along the circumference.

The modal decomposition method described in [16] assumes that the annular combustor (Chapter 4) does not exhibit radial modes in the frequency domain of interest (0-800 Hz). According to [16], the cut-on frequencies of the first radial modes of the cold plenum and combustion chamber lie at 1250 Hz and 2208 Hz, respectively. Since Sallikudin et al. [52] have shown that radial modes are negligible for frequencies below 80% of their cut-on frequency ($0.8 \cdot (kR_M)_{cut-on}$) with $k = \omega/c$ the wavenumber and $R_M = \sqrt{0.5(R_i^2 + R_o^2)}$ the radial modes do not need to be taken in consideration in this work where the investigated frequencies were below 800 Hz.

The modal decomposition of the acoustic pressure field measured in one axial plane is based on the assumption that the annular combustor is a linear system whose dynamic behaviour is a weighted superposition of the system eigenmodes. Analytically, this can be modelled as an infinite summation of orthogonal functions each representing one eigenmode. As seen in Chapter 5.3.4, the eigenmodes of the annular combustor are the solutions of the 2D Helmholtz equation (Eqn. 5.20) presented in Eqn. 5.39 where additionally the boundary conditions for the wave propagation in axial direction must be considered. When considering the acoustic field at one axial position only, the solution from Eqn. 5.39 becomes 1D. Then, the analytical description of the acoustic pressure field can be written as

$$\hat{p}(\theta) = a_0 + \sum_{k=1}^N \{a_{k+} [\cos(k\theta) + i \sin(k\theta)] + a_{k-} [\cos(k\theta) - i \sin(k\theta)]\} \quad (7.1)$$

where N is the number of eigenmodes taken in consideration. In Eqn. 7.1 the cartesian coordinate y from Eqn. 5.39 has been transferred in the azimuthal coordinate θ and the parameters $a_{k\pm}$ are the complex amplitudes of the k^{th} order spinning azimuthal modes travelling in the clockwise and anticlockwise sense of rotations, respectively. In Eqn. 7.1 the axial wave propagation is not considered but the axial component is represented by the complex constant a_0 .

If the azimuthal modes in the annular combustor are standing, the description of acoustic pressure waves can be further simplified as in Eqn. 5.54. Hence, the modal decomposition function is [16]

$$\hat{p}(\theta) = a_0 + \sum_{k=1}^N a_k \cos[k(\theta - \theta_k)] \quad (7.2)$$

where a_0 is a complex constant describing the axial component and a_k are the complex amplitudes of the standing azimuthal modes up to the N^{th} order. The standing azimuthal modes are described analytically as cosine functions with the parameters θ_k being introduced additionally. These express the offset angle of rotation for the azimuthal components k with respect to the origin ($\theta = 0^\circ$).

Eqn. 7.1 or 7.2 deliver the exact solution of the acoustic field only if an infinite number of azimuthal components ($N \rightarrow \infty$) is considered. Nevertheless, for most common engineering problems and for the acoustic investigations performed in this work, a reduced number of modes is enough to ensure a very good approximation.

With the measured amplitudes and phases of the acoustic pressure at several azimuthal positions θ , a linear system consisting of Eqs. 7.1 or 7.2 can be constructed where the complex modal amplitudes $a_{k\pm}$, a_k and the azimuthal offsets θ_k represent the unknowns to be evaluated. The condition to be fulfilled in order to ensure the solvability of the system is that the number of equations - the number of measurement points - must be equal to or greater than number of unknowns. The number of unknowns depends on the acoustic eigenmodes existing in the frequency domain of interest. According to Tab. 5.1 four eigenfrequencies ($N=0,1,2,3$ with $N=0$ the axial mode and $N=1,2,3$ the azimuthal modes of the 1st, 2nd and 3rd order) of the combustor are expected in the frequency domain below 800Hz. Therefore, at least seven dynamic pressure transducers ($N=3$ in Eqn. 7.1 yields 7 complex or 14 real unknowns) are necessary for solving the system with Eqn. 7.1. For Eqn. 7.2 the number of unknowns is less ($N=3$ in Eqn. 7.2 yields 4 complex and 3 real unknowns or 11 real unknowns) and consequently six sensor units are sufficient.

By having more measurement points than unknowns, a least square fit procedure of the modal functions from Eqs. 7.1 and 7.2 is made on the experimental data to determine the modal components:

$$\sum_{\theta=1}^I \left[\hat{p}_{\theta} - a_0 - \sum_{k=1}^N a_k \cos(k(\theta - \theta_k)) \right]^2 \rightarrow \min \quad (7.3)$$

Here I is the number of measurement points for the acoustic pressure and N the number of azimuthal acoustic modes considered. The experimental data is measured with dynamic pressure transducers distributed on the outer wall of the plenum and combustion chambers at several circumferential positions and at the same axial coordinate, as represented in Fig. 7.1.

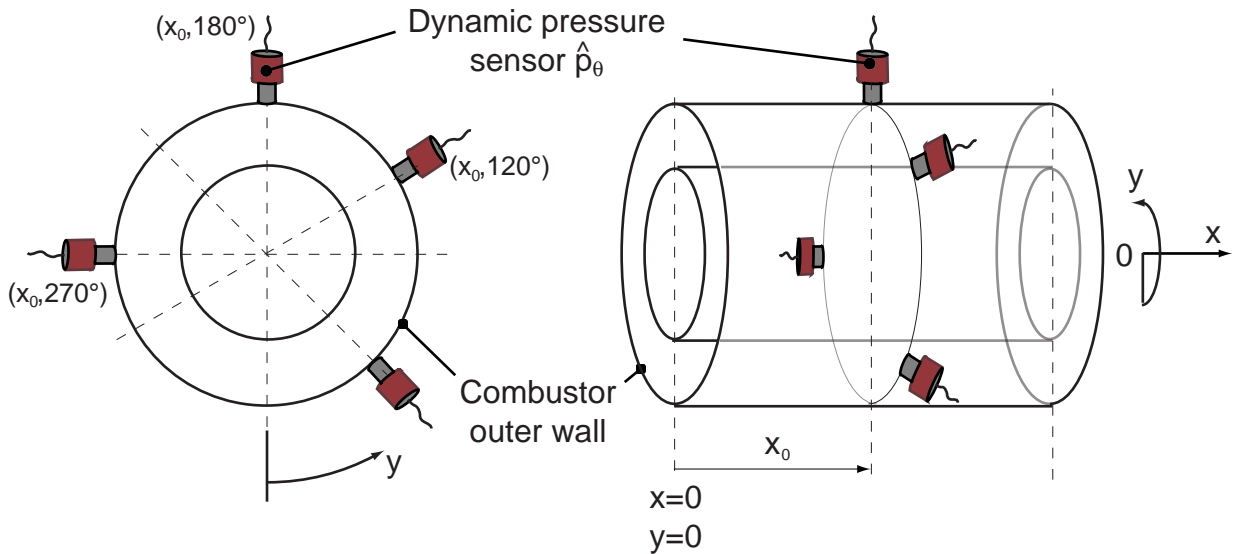


Figure 7.1: Schematic representation of the experimental set-up for the acoustic pressure measurement: dynamic pressure transducers mounted on the outer combustor wall at one axial position x_0 and different circumferential coordinates y

The quality of the modal decomposition can be expressed by the approximation error of the least square fit procedure defined in Eqn. 7.4.

$$e = \frac{\sum_{\theta=1}^I |\hat{p}(\theta) - \hat{p}_\theta|^2}{\sum_{\theta=1}^I |\hat{p}_\theta|^2} \quad (7.4)$$

With the modal decomposition procedure, only the azimuthal modal shapes are determined in the respective axial plane. For the mode shapes in axial direction, it is postulated that the structure of the acoustic field is similar in the other axial planes with the respective phase delay corresponding to the axial distribution of the acoustic pressure.

As explained above, the evaluation of the complex modal amplitudes a_k is made with the acoustic pressures measured at several azimuthal positions. Here, the phase of every sensor is reported to the phase of the sensor placed at the reference azimuthal position (θ_{ref}). Hence, the phases of the decomposed modal amplitudes $a_{k\pm}$ and a_k are related to the reference azimuthal position (θ_{ref}) as well. The azimuthal offset θ_k of every standing modal component is related to the azimuthal origin ($\theta = 0^\circ$). The reference azimuthal position θ_{ref} and the azimuthal origin $\theta = 0^\circ$ may coincide ($\theta_{ref} = 0^\circ$) if for the respective measurement the reference was chosen at the azimuthal origin. The option of choosing the reference at the azimuthal origin ($\theta_{ref} = 0^\circ$) is conditioned by the existence of an acoustic pressure sensor here. For measurements campaigns where, depending on the specific conditions, the sensors were placed at other azimuthal positions than the origin ($\theta = 0^\circ$), the reference was chosen accordingly.

The relative contribution of the modal component a_k to the total signal power in the axial plane under consideration is

$$Y_k = \frac{a_k^2}{\sum_{j=0}^N a_j^2} \quad (7.5)$$

where the index k can take the value zero to include also the axial component.

As seen in Chapter 5.3.4, the spinning tendency of the k^{th} order azimuthal modes is described quantitatively by the spin-ratio Δ_{sp}^k

$$\Delta_{sp}^k = \frac{(1 - |\alpha_k|)^2}{1 + |\alpha_k|^2} \quad (7.6)$$

where α_k is a complex parameter defined as:

$$\alpha_k = \frac{a_{k-}}{a_{k+}} \quad (7.7)$$

In Eqn. 7.7 $k = 1, 2, 3$ denotes the 1st, 2nd and 3rd order azimuthal modes, respectively.

In order to express the spinning tendency of the whole acoustic field with respect to each modal component, the spin-ratios Δ_{sp}^k determined with Eqn. 7.6 can be weighted with the relative contributions Y_k of every modal component (Eqn. 7.5).

7.2 Acoustic Network Model of the Annular Combustor

The acoustic network model of the annular combustor was developed based on the linear acoustic network theory introduced in Chapter 6 and was used as a platform for the determination of the BTM and FTF.

The model captures the 2D character of the acoustic field with axial and azimuthal modes. Regarding the azimuthal modes, only the standing components are considered. In the work presented here, this is in agreement with the experimental findings. Preliminary investigations under cold isothermal flow, presented in Chapter 8.1, have shown that the azimuthal modes are predominantly standing. The modal amplitudes of the spinning components are negligible and appear only when the excitation pattern is set accordingly (purposefully excitation of spinning modes). With considering only standing azimuthal modes, the 2D acoustic wave propagation is described simplified with

Eqs. 5.54, 5.55 and 5.56 where the mode shape in circumferential direction is expressed analytically by the cosine function $\cos(my/R)$. Hence, with this model the complex modal amplitudes \hat{p} , \hat{u} and \hat{v} need to be calculated only at a single reference circumferential position. At all other circumferential position along the annulus, these can be deduced analytically with $\cos(my/R)$. By choosing the reference circumferential position at $y = 0$, the azimuthal acoustic velocity \hat{v} vanishes ($\sin(my/R) = 0$) and the acoustic field is completely determined by the two variables pressure \hat{p} and axial velocity \hat{u} expressed by the following equations:

$$\frac{1}{\rho c} \hat{p}(x) = \left(F e^{-ik_x^+ x} + G e^{-ik_x^- x} \right) \quad (7.8)$$

$$\hat{u}(x) = \left(\kappa_u^+ F e^{-ik_x^+ x} + \kappa_u^- G e^{-ik_x^- x} \right) \quad (7.9)$$

In Eqns. 7.8 and 7.9, the axial wavenumber k_x^\pm is defined as in Eqn. 5.45 and is extended with an additional term which models the visco-thermal acoustic damping in boundary layers. Hence, the the expression of the axial wavenumber k_x^\pm which includes damping in the boundary layers is for a 1D wave propagation ($m = 0$):

$$k_x^\pm = \frac{\omega}{c(1 \pm M)} \left[1 + \frac{1-i}{\sqrt{2}} \frac{1}{Sh} \left(1 + \frac{\gamma-1}{\sqrt{Pr}} \right) \right] \quad (7.10)$$

The term enclosed in the square brackets in Eqn. 7.10 expresses the visco-thermal acoustic damping in boundary layers and is similar to the expression proposed by Peters et al. [46] (see Eqn. 5.66) with the only difference that the term containing the second power of the shear number Sh has been neglected.

The acoustic network model of the annular combustor, developed with the simulation tool TA2 (ALSTOM), is presented schematically in Fig. 7.2. The elements of the model are numbered in Fig. 7.2 and are described in detail the following.

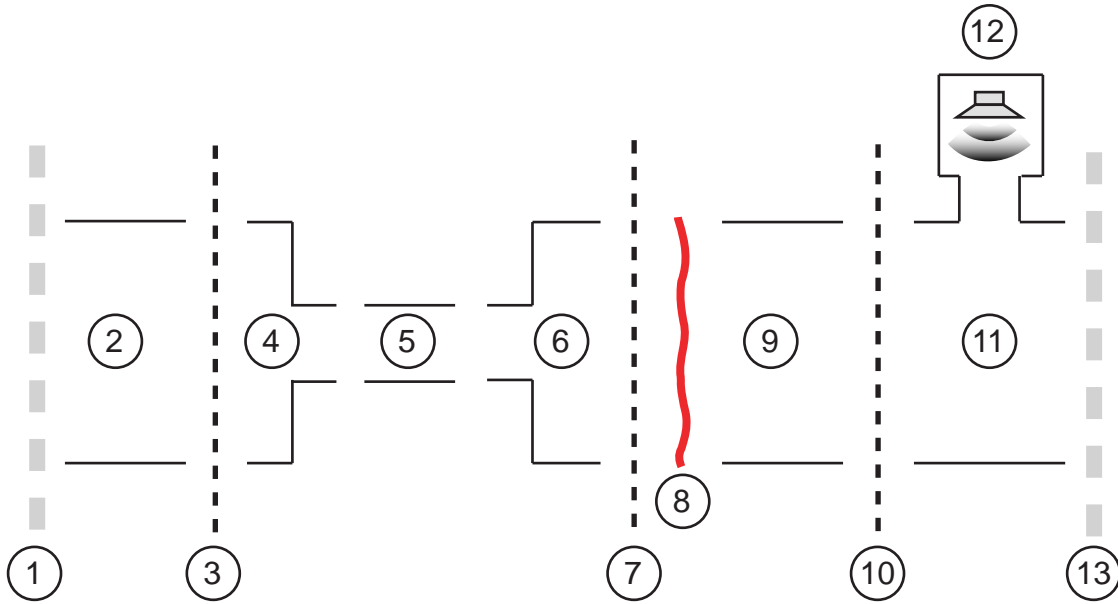


Figure 7.2: Schematic representation of the acoustic network model of the ACC

1. Inlet (upstream) acoustic boundary

The upstream acoustic boundary was modelled as fully reflective. The reflection coefficient was set to unity in the whole frequency domain. The motivation for this ansatz is given by the high area ratio of 55 between the cross-section of the plenum chamber and the inlet mixing tubes.

2. and 9. Annular plenum and combustion chambers

The annular plenum and combustion chamber were modelled as thin annular ducts with a 2D acoustic wave propagation. The input dimensions are (see Section 4.1) $h_{cc}/D_{cc}/L_{cc} = 136\text{mm}/437\text{mm}/223\text{mm}$ for the plenum chamber and $h_{cc}/D_{cc}/L_{cc} = 77\text{mm}/437\text{mm}/279\text{mm}$ for the combustion chamber, respectively. The change of the acoustic parameters pressure and axial velocity is described in Eqs. 7.8 and 7.9 with the axial wavenumber k_x^\pm that is defined in Eqn. 5.45.

3. and 4. Acoustic uncoupling element and area contraction (interface plenum-burner)

The elements acoustic uncoupler and area change model the zero length interface plenum-burner (see Section 6.3.4). The first element describes the transition from the 2D wave propagation in the upstream side to the 1D wave propagation in the burner. The area change element describes the area contraction from the plenum chamber to the burner inlet ducts and was modelled as an area discontinuity without acoustic losses and with an effective length. The effective length l_{eff} has been calculated with the formula presented by Evesque [17]

$$\frac{l_{eff}}{h_b} = \frac{1}{\pi} \left[\frac{(h_{pl} - h_b)^2}{2h_{pl}h_b} \ln \left(\frac{h_{pl} + h_b}{h_{pl} - h_b} \right) + \ln \left(\frac{(h_{pl} + h_b)^2}{4h_{pl}h_b} \right) \right] \quad (7.11)$$

where the h_{pl} is the thickness of the plenum chamber and h_b the thickness of a generic annulus having the cross-section of the 12 burners ($12A_b$). The analytical transfer matrix of the plenum-burner interface is presented in Eqn. 6.27.

5. Burner

The burner was represented acoustically as a simple longitudinal duct with a 1D acoustic wave propagation. The input dimensions are the length $L_b = 40mm$ and the cross section A_b corresponding to the nominal burner diameter d_0 . The analytical transfer matrix is given in Eqn. 6.7 and the corresponding wavenumber for the 1D wave propagation in Eqn. 5.23.

6. and 7 Area expansion and acoustic uncoupling element (interface burner-combustion chamber)

The zero length interface burner-combustion chamber was modelled as a compact element with losses (Chapter 6.3.2) followed by an acoustic uncoupling element (Chapter 6.3.4). The compact element describes the acoustic losses produced by the swirled flow of the burner at the expansion in the combustion chamber and the acoustic uncoupling element models the transition between the 1D acoustics in the burner and the

2D wave propagation in the combustion chamber. The transfer matrix of the burner-combustion chamber interface is given in Eqn 6.28. The parameters effective length l_{eff} and the pressure loss coefficient ζ have been kept as free parameters to be determined through validation with experimental data. The reduced length has been set to zero ($l_{red} = 0$) as its influence of the acoustic transfer matrix of the burner was found to be negligible [5].

In the framework presented here, the burner arrangement was assumed symmetrical, i.e. the 12 burner units are geometrically identical and consequently are modelled with a global transfer matrix.

8. Premixed flame

The dynamic characteristics of the premixed flame were implemented in the acoustic model of the annular combustor as a classical $n - \tau$ formulation which describes the reaction zone as a acoustic discontinuity of infinitesimal length (Chapter 6.3.3). The $(n - \tau - \sigma)$ model presented in Eqn. 6.18 expresses the transfer function of the flame in terms of the acoustic perturbations in the burner and is used to describe the acoustic behaviour of the EV5 burner in the PPM. For IPM the flame transfer function is expressed by the $(n - \tau - \sigma - \phi)$ model presented in Eqn. 6.17, which describes the dynamic behaviour of the flame as an effect of both the variation of the turbulent burning velocity at the flame front and equivalence ratio fluctuations. The determination of the flame transfer matrix in both operational modes is made through regression of the free model parameters n , τ , σ , τ_ϕ and σ_ϕ on experimental data.

As in the case of the burner arrangement, the 12 premixed flames are assumed to be identical and are therefore represented with a global FTF.

10. Acoustic uncoupling element

This uncoupling element models the transition between the 2D acoustic wave propagation in the annular combustion chamber and the 1D acoustic field in the end section. The transfer matrix $\mathbf{T}_{\text{uncoupling } 2\text{D} \rightarrow 1\text{D}}$ is given in Eqn. 6.27.

11. Acoustic junction element

The acoustic junction element was used to model the end section of the combustion chamber (see Chapter 6.3.5), which consists of the external excitation module (speaker element) and the exit acoustic boundary. The analytical transfer matrices of the element are given in Eqns. 6.32 and 6.33 where the downstream cross-sections were set equal to the cross-sectional area of the combustion chamber ($A_{d1} = A_{d2} = A_{cc}$).

12. Acoustic excitation source. Speaker

The acoustic excitation of the network model was designed as velocity forcing. This network element is an acoustic boundary condition which imposes an acoustic velocity with a constant amplitude and phase on the entire frequency domain as expressed in the following equation:

$$\hat{u}_{speaker} = f - g \quad (7.12)$$

In Eqn. 7.12, f and g are the Riemann invariants, the downstream and upstream propagating acoustic velocity waves for a 1D acoustic field. The parameter $\hat{u}_{speaker}$ is the amplitude of the excitation.

13. Outlet (downstream) acoustic boundary

The convergent nozzles mounted at the exit of the annular combustion chamber generate a highly reflecting acoustic boundary. This must be modelled appropriately in order to simulate correctly the dynamic behaviour of the test rig. Hence, the reflection coefficient of the nozzle was measured in the single burner test rig with the MMM described in Chapter 6.2. This investigation was carried out in the frequency domain below 800 Hz and with variation of the Mach number in the nozzle. Afterwards, the results were implemented in the model. The measured reflection coefficient of the exit nozzle is presented in Fig. 7.3 as a function of the nozzle Mach number and frequency.

The results of the reflection coefficient measurements for the exit nozzle, presented in Fig. 7.3, reveal that the amplitude increases with higher Mach numbers as expected from the literature [37]. Below 300 Hz this exhibits a non-

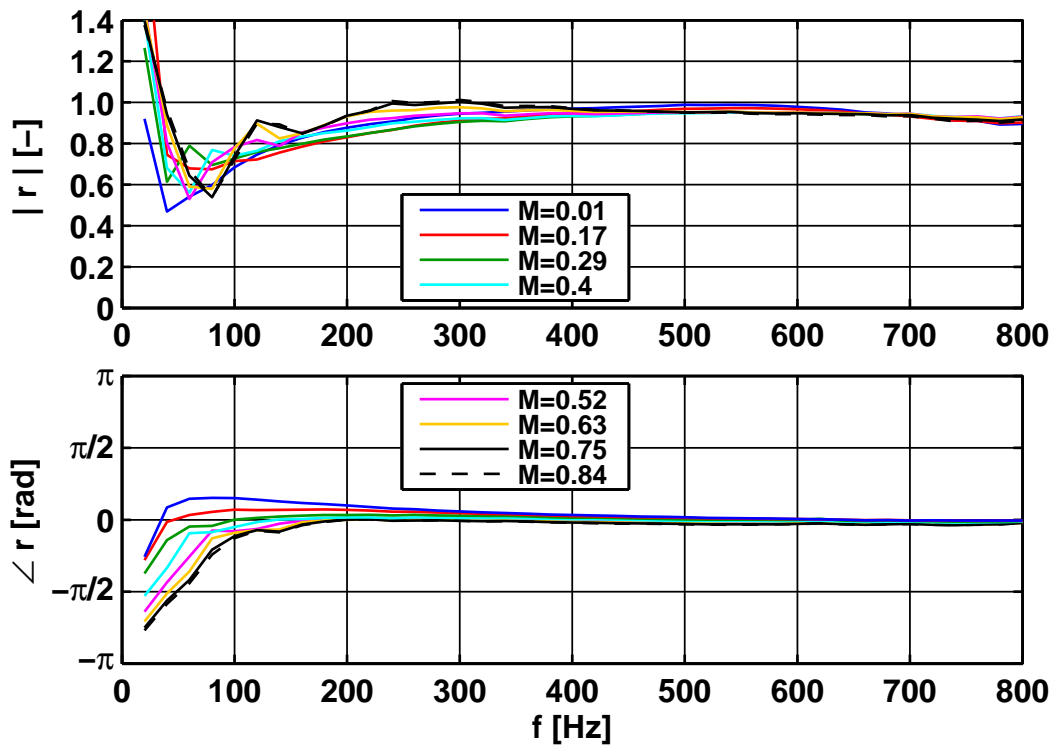


Figure 7.3: Measured reflection coefficient of the exit nozzle

constant evolution. Towards the lower frequency limit - below 50 Hz - the amplitude increases strongly and reaches values well over unity. This non-physical behaviour in the low frequency domain is an effect of the measurement uncertainty [5].

8 Determination of the BTM and FTF

8.1 Acoustic Measurements with the Isothermal Flow

The acoustic measurements with the cold isothermal flow have been made prior to the determination of the burner and flame transfer matrices in order to investigate in detail the acoustic field of the annular combustor. The focus of the investigations lay on the variation of the operating parameters mass flow, exit Mach number and external excitation mode. The important aspects were the quantitative evaluation of the spinning tendency and the formation and structure of the system eigenmodes. A summary of all operating points investigated is given in Tab. 8.1.

The annular combustion chamber test rig was equipped with the choked exit. Both standard and reduced diameter nozzles have been used, the latter to produce a high exit Mach number flow and therefore a highly reflective acoustic boundary, similarly to the case with combustion. The six air sirens were mounted on the downstream side, equally distributed on the circumference. The combustion chamber was equipped with 12 lean premixed swirl stabilised EV5 burners from ALSTOM.

Each measurement consisted in acoustic pressure recordings at a specific operating point defined by the parameters air mass flow rate and external excitation mode. The forcing frequency was varied from 10 to 800 Hz. In this frequency band, the axial and the first three azimuthal eigenfrequencies were expected, according to Tab. 5.1. To identify all modal components of the measured acoustic pressure field with the modal functions from Eqs. 7.1 and 7.2 ($N = 3$), seven dynamic pressure transducers were employed. These were mounted on the combustor wall (see Fig. 4.7) at the same axial position and distributed at several azimuthal coordinates. The data acquisition consisted

Table 8.1: Operating parameters and excitation modes for the cold acoustic measurements

Operating point	AMF [g/s]	M_{nozzle} [-]	Exit nozzle	Excitation mode
1	100	0.25	standard	axial
2	100	0.25	standard	1 st azimuthal standing
3	285	0.27	standard	axial
4	285	0.27	standard	1 st azimuthal standing
5	285	0.58	reduced	axial
6	285	0.58	reduced	1 st azimuthal standing
7	400	0.31	standard	axial
8	400	0.31	standard	1 st azimuthal standing
9	500	0.38	standard	axial
10	500	0.38	standard	1 st azimuthal standing
11	500	0.83	reduced	axial
12	500	0.83	reduced	1 st azimuthal standing
13	660	0.97	reduced	axial
14	660	0.97	reduced	1 st azimuthal standing

in the recording of 16 loops of time domain series for every frequency and channel. All measurement loops were sampled simultaneously at 16384 samples/second and a number of 16384 values was stored.

The experimental results corresponding to the operating points 11 and 12 (Tab. 8.1) are presented in Fig. 8.1 for the axial and in Fig. 8.2 for the 1st order azimuthal excitation modes. The data was measured in the combustion chamber at an axial position $x = 80\text{mm}$ (Fig. 4.3). The results are displayed as frequency response function spectra of the seven dynamic signals with respect to the reference ($\theta_{ref} = 0^\circ$). For this operating point, the exit nozzles were equipped with the special adapters in order to reduce the diameter. The air

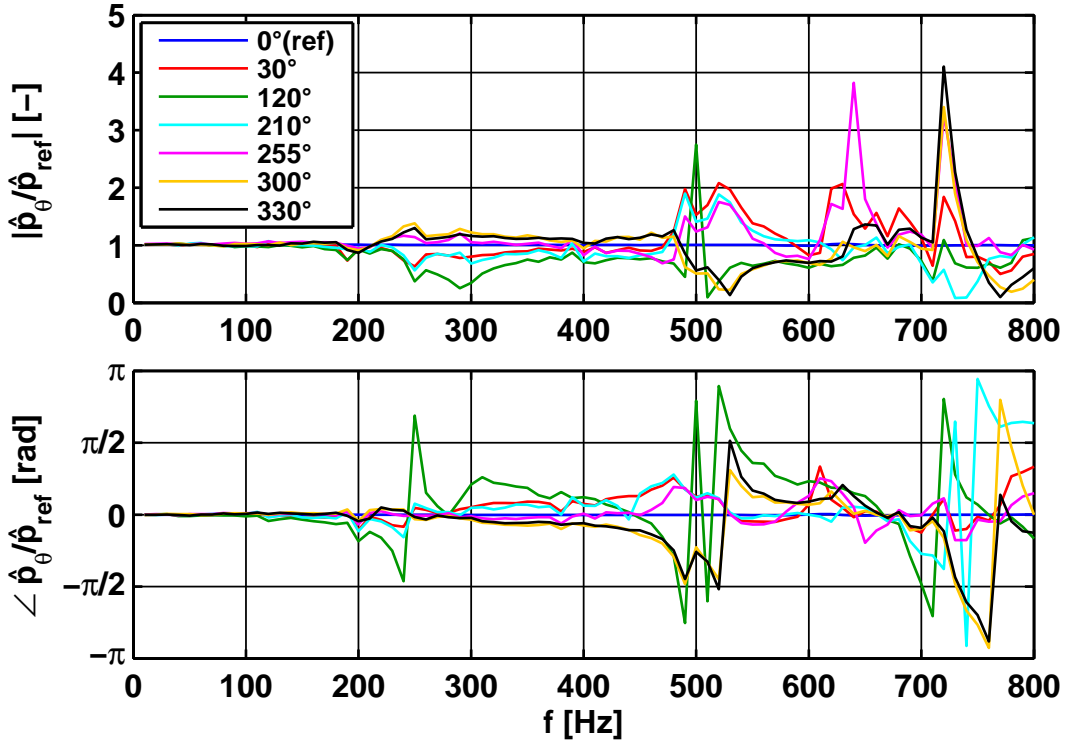


Figure 8.1: Frequency response function of the measured acoustic response under axial excitation

mass flow rate was set to 500 g/s at ambient temperature. The exit Mach number was around 0.83, similar to the case with combustion. With this large Mach number, a highly reflective exit acoustic boundary was generated.

The frequency spectra of the absolute acoustic pressure \hat{p} measured with axial excitation did not exhibit a clear axial resonant behaviour. In the spectra of the frequency response function, an axial eigenfrequency would be characterised by equal amplitudes and phases along the circumference. In Fig. 8.1, the amplitudes and phases along the annular circumference differ especially above 200 Hz due to the presence of the azimuthal modes. These oscillate because the system is excited close to or at the respective eigenfrequencies (250 Hz, 500 Hz and 750 Hz, Tab. 5.1). The amplitudes and phases are equal ($|\hat{p}_\theta / \hat{p}_{ref}| \rightarrow 1, \angle \hat{p}_\theta / \hat{p}_{ref} \rightarrow 0$) only towards the lower frequency limit as an effect of the excitation type.

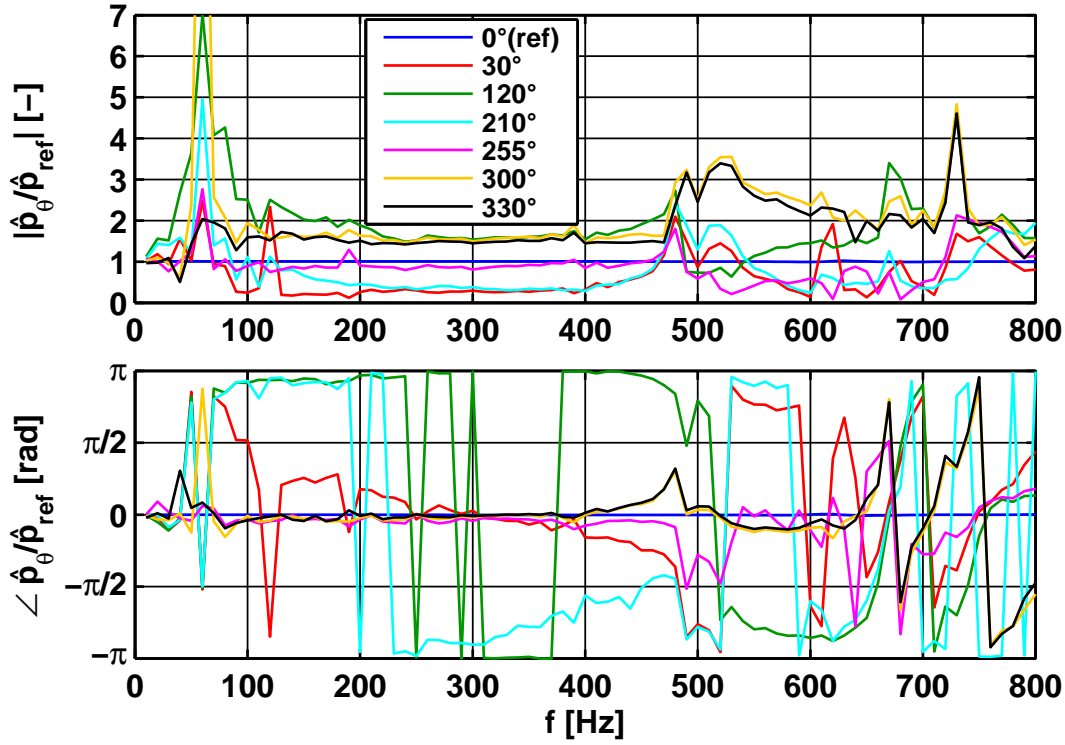


Figure 8.2: Frequency response function of the measured acoustic response under 1st order standing azimuthal excitation

In the case of the 1st order azimuthal excitation, the frequency spectra of the absolute acoustic pressure \hat{p} exhibited a clear resonant peak at 250 Hz, the eigenfrequency of the 1st order azimuthal mode (Tab. 5.1). The spectra of the frequency response function presented in Fig. 8.2, shows in the frequency band between 100 and 400 Hz a variation of the amplitude and $\pm\pi$ phase jumps along the circumference. This indicates a standing azimuthal mode pattern.

The spinning tendency of the acoustic field measured in cold isothermal conditions (Tab. 5.1) was evaluated quantitatively with the method described in Chapter 7.1. The results are presented in Fig. 8.3 as the spin-ratio Δ_{sp} of the modal components a_1 , a_2 and a_3 for the excitation states axial and 1st order standing azimuthal. Here, Δ_{sp} has been weighted with the relative contribution of the modal component Υ (Eqn. 7.5) in the total signal power, in order to express the spinning tendency of the entire acoustic field.

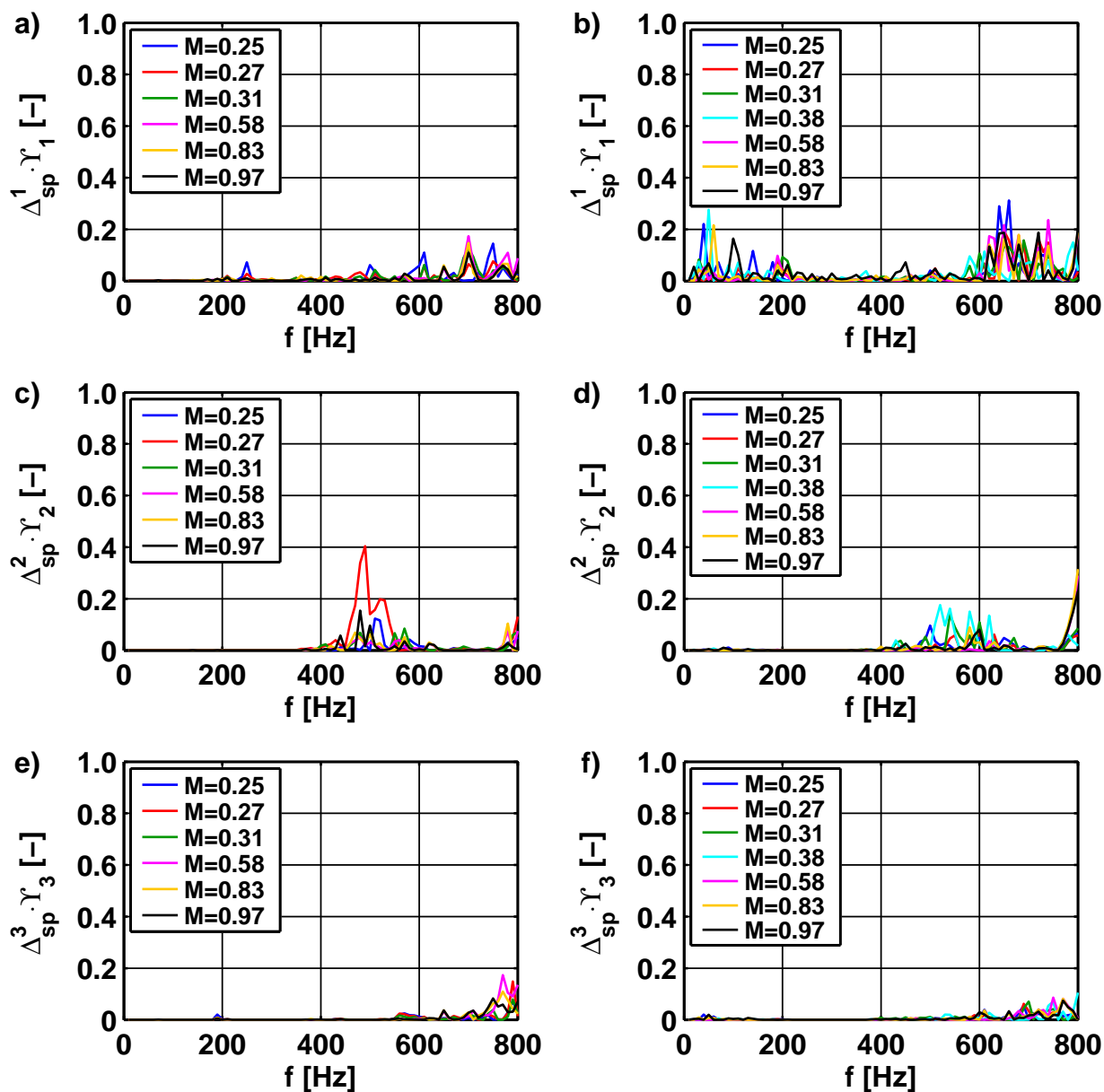


Figure 8.3: Weighted spin-ratios Δ_{sp}^1 , Δ_{sp}^2 and Δ_{sp}^3 for axial (a,c,e) and 1st order standing azimuthal (b,d,f) excitation

Fig. 8.3 shows clearly that the acoustic field is dominantly standing with the spin-ratios being in general very low in the entire frequency domain. Nevertheless, locally some preferred frequency bands can be identified where spinning components oscillate stronger. This applies especially to the higher order

azimuthal components $a_{2\pm}$ and $a_{3\pm}$. The first exhibits relatively high values of the spin-ratio around the eigenfrequency of 500 Hz (Fig. 8.3 c and d) with values up to 30%. The spin ratio Δ_{sp}^3 of the 3rd order azimuthal component is negligibly small and raises only in the upper frequency domain between 600 and 800 Hz (Fig. 8.3 e and f). In the case of the 1st order azimuthal excitation, the weighted spin-ratio of the driving mode Δ_{sp}^1 exhibits values close to zero around the eigenfrequency of 250 Hz (Fig. 8.3b). This is a consequence of pulsating the standing mode at the eigenfrequency which results in a "fixing" effect. In the rest of the frequency domain Δ_{sp}^1 is more pronounced but still low. The Mach number variation in the exit nozzle does not have a significant influence on the spinning ratio; all the operating points investigated are characterised qualitatively by similar results.

As seen in Fig. 8.3, the spinning tendency of the acoustic field is more pronounced in the higher frequency region due to the superposition of the spinning components corresponding to all azimuthal modes. Consequently, the modal decomposition with the modal function from Eqn. 7.2, which takes in consideration only standing azimuthal modes, shows large errors for frequencies above 600 Hz (Fig. 8.4).

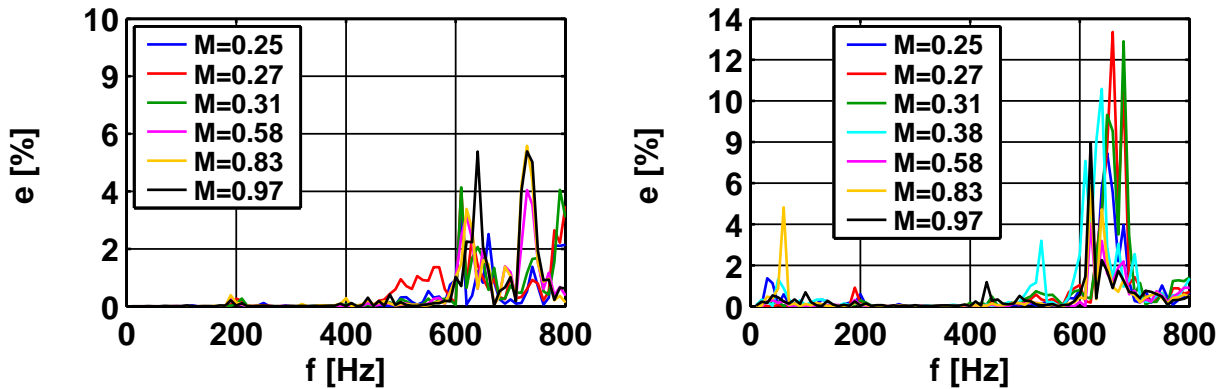


Figure 8.4: Error of the modal analysis procedure for axial (left) and 1st order standing azimuthal (right) excitation

In the lower frequency domain, where the spinning tendency is small, the error e (Eqn. 7.4) does not exceed in general 1%. For this reason, the experimental results of the modal decomposition method presented in the next para-

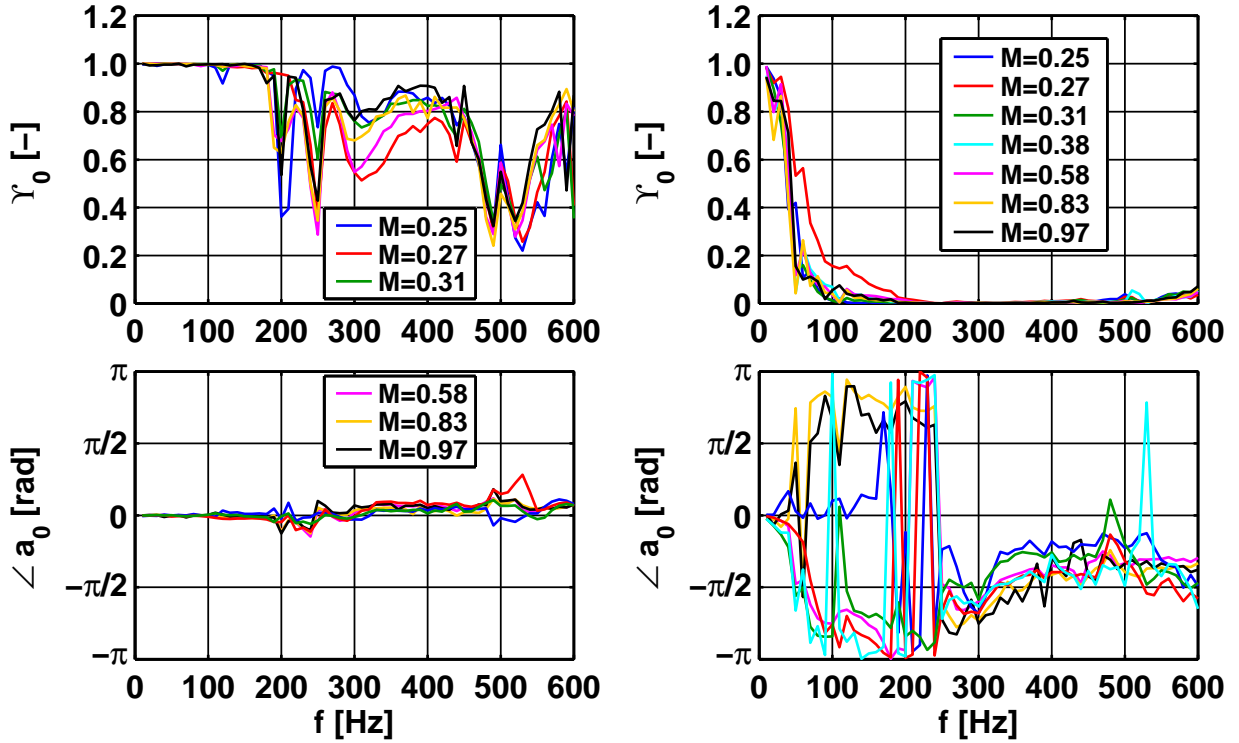


Figure 8.5: γ_0 for axial (left) and 1st order azimuthal (right) excitation

graphs are used further for the development of the acoustic model of the cold annular combustor only in the frequency domain below 600 Hz.

The modal components a_k evaluated with the modal function from Eqn. 7.2 are presented in Figs. 8.5, 8.6 and 8.7 for the external excitation axial (left) and 1st order standing azimuthal (right). The results show that the structure of the acoustic field of the annular combustor is determined by acoustic eigenmodes of the system which are driven by the external excitation (axial or 1st order standing azimuthal). In essence, the acoustic response is not influenced by the exit Mach number.

For the case with axial excitation (Fig. 8.5 left), the relative contribution γ_0 of the axial component a_0 exhibits high values in the entire frequency range. At the lower frequency limit, γ_0 reaches unity and zero phase with respect to the reference azimuthal position $\theta_{ref} = 0^\circ$ due to the excitation type. With increasing frequency however, the amplitude of a_0 drops continuously due

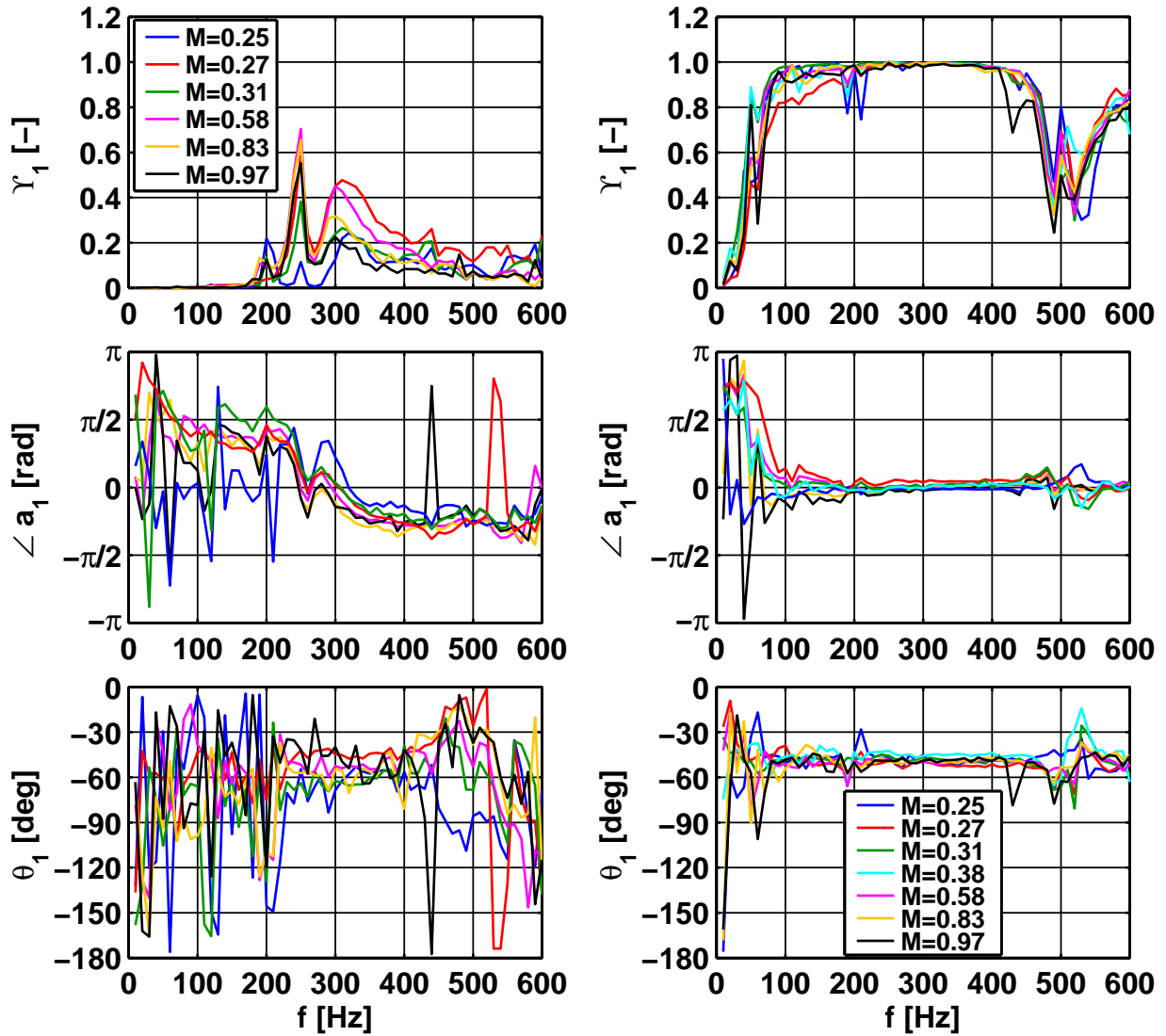


Figure 8.6: γ_1 for axial (left) and 1st order azimuthal excitation (right)

to increasing the modal component a_1 as an effect of pulsating the combustor at the resonance frequency of the 1st order azimuthal mode (Fig. 8.6 left). Around the eigenfrequency of 250 Hz, the two modal components a_0 and a_1 exhibit opposite trends with the latter having a local maximum (Fig. 8.6 left). When the excitation pattern is set to pulsate the 1st order azimuthal mode, the azimuthal component a_1 dominates the acoustic pressure field (Fig. 8.6 right) in the entire frequency range below 500 Hz. Consequently, the relative contribution of the axial component γ_0 is very low (Fig. 8.5 right) and as an effect of

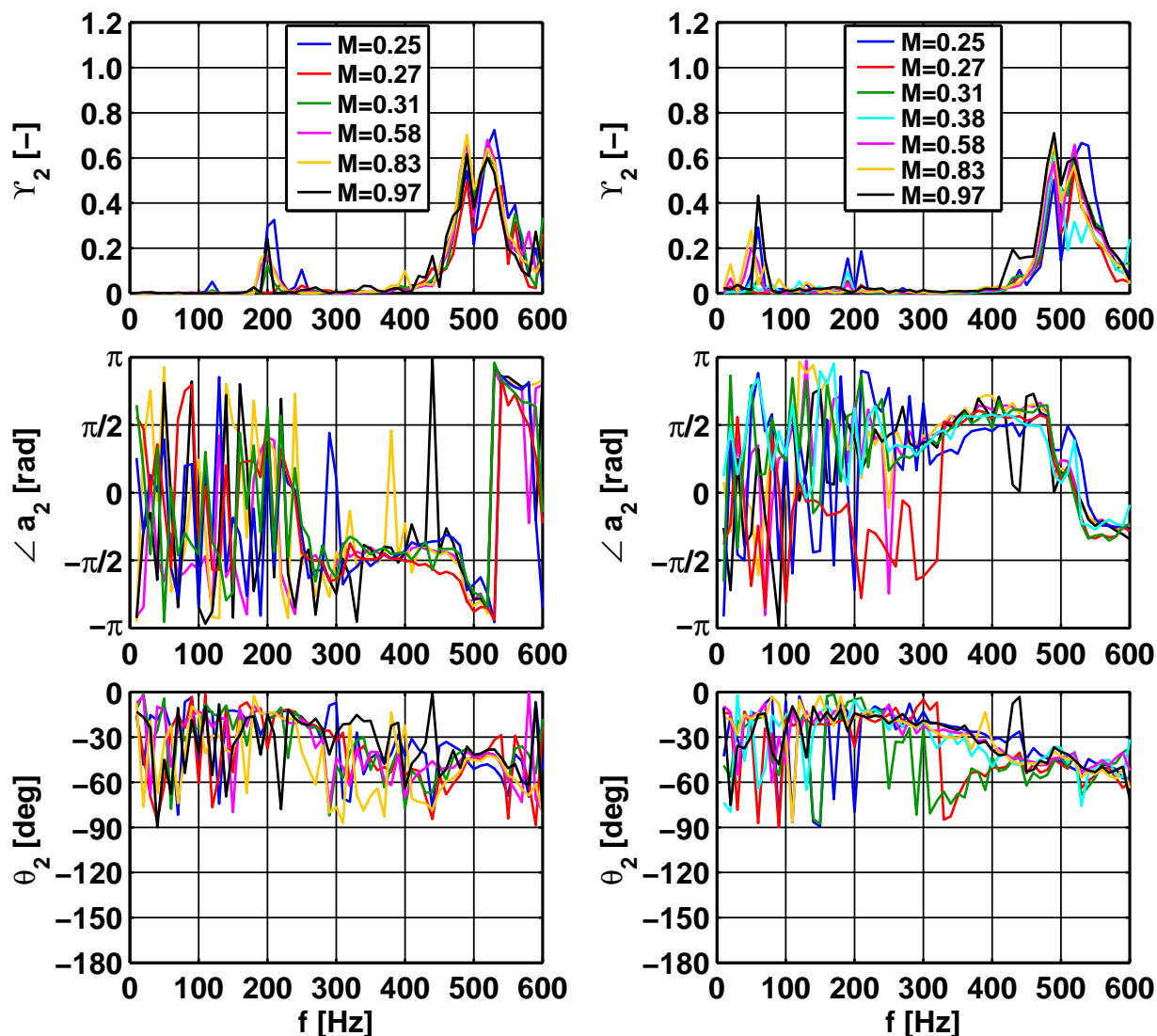


Figure 8.7: Υ_2 for axial (left) and 1st order azimuthal excitation (right)

this the phase has a large scatter. These results correlate very well with the data presented in Fig. 8.2 where the resonance of the 1st order standing azimuthal mode could be recognised in the frequency band from 100 to 400 Hz.

The 2nd order azimuthal component a_2 is strongly cut-off in the lower frequency domain and develops only in the upper half exhibiting a peak at the eigenfrequency of 500 Hz (Fig. 8.7). It can be clearly noticed that the mode develops relatively independent of the excitation pattern.

One additional aspect which can be noticed is the tendency of the azimuthal modes to exhibit a "preferred" azimuthal position θ_k . This observation is valid especially at the resonance and for the azimuthal components which are not directly forced by the external excitation, i.e. the modal component a_1 with axial excitation (Fig. 8.6 left) and a_2 with both axial and azimuthal excitations (Fig. 8.7). The azimuthal position of the modal component a_1 with the 1st order azimuthal excitation (Fig. 8.6 right) is determined, however, by the excitation pattern.

The experimental investigations of the cold isothermal flow presented in this chapter have shown that the acoustic system of the combustor can be externally pulsed with both planar and non-planar modes. The structure of the acoustic field is predominantly determined by the driving mode of the siren. Nevertheless, other modal components oscillate as well, especially when the frequency of the external excitation lies close to or at the respective eigenfrequencies. Furthermore, the azimuthal modes have a standing pattern. The fraction of the spinning components is negligibly small and become dominant only when the driving mode is set accordingly. Consequently, the acoustic field of the annular combustor can be modelled with the acoustic network modelling theory described in Chapter 6.

8.2 Model Based Analysis of the Cold Acoustic Measurements

The experimental results of the acoustic investigations of the isothermal flow presented in the previous chapter have been used as reference data for the development of the acoustic model of the cold annular combustor. A model based analysis consisting of a qualitative and quantitative comparison between the model calculations and the measured data in both plenum and combustion chamber has been made. The focus of the model based analysis was the determination of the burner transfer matrix, i.e. the evaluation of the free model parameters ζ and l_{eff} (Chapter 6.3.2). For the model based analysis, the acoustic response of the annular combustor has been measured in both combustion chamber and plenum at the operating parameters 9 and 10 from Tab. 8.1). In Chapter 8.1 it was shown that the acoustic field of the annu-

lar combustor does not change qualitatively with the variation of the operating parameters.

Additionally, the acoustic response of the annular combustor was calculated with the acoustic model presented in Chapter 7.2. As described in Chapter 5.3.4, the acoustic model computes the pressure spectrum for a planar wavefront by setting the mode index m of the axial wavenumber (Eqn. 5.45) to zero. This corresponds to the complex amplitude of the axial component a_0 (Eqn. 7.2) obtained after performing the modal decomposition of the measured pressure field. For $m = 1, 2, 3$ the acoustic model computes the pressure spectra of pure and mixed standing azimuthal modes 1st, 2nd and 3rd order respectively. For the simulations, the flow parameters and the corresponding acoustic exit boundary condition have been set according to the operating parameters of the test rig. The parameters of the simulations are given in Tab. 8.2. In Tab. 8.2 x_{pl} and x_{cc} are the axial positions where the acoustic response was calculated.

Table 8.2: Simulation parameters for the cold acoustic measurements

Mode index m	0	1
$M_{pl}[-]$	0.006	0.006
$c_{pl}[m/s]$	342	342
$\rho_{pl}[kg/m^3]$	1.27	1.27
$M_b[-]$	0.05	0.05
$c_b[m/s]$	342	342
$\rho_b[kg/m^3]$	1.27	0.27
$M_{cc}[-]$	0.01	0.01
$c_{cc}[m/s]$	342	342
$\rho_{cc}[kg/m^3]$	1.27	1.27
$x_{pl}[mm]$	-160	-160
$x_{cc}[mm]$	80	80
Experiment	Point 9	Point 10

The results are presented in Fig. 8.8 as amplitude factor and phase difference spectra between the calculated and measured acoustic modes in the plenum and combustion chamber. This representation allows for a thorough evaluation of the quality of the acoustic simulations. It avoids misinterpretations

due to the uncertainties of the acoustic model regarding the assumed level of the external excitation. The external excitation has been implemented as a constant acoustic velocity over frequency because no knowledge on the siren impedance was available. This solution is not necessarily correct as it may not correspond with the real conditions in the test rig. Consequently, the interpretation of the results may encounter difficulties when comparing directly the simulation with the measurement. Eventual discrepancies may not be correctly explained as these could be an effect of either the acoustic characteristics of the combustor which hadn't been modelled properly or of the improperly modelled siren impedance. For this reason the measured and calculated acoustic pressure spectra are compared as the ratio between the combustion chamber and plenum values.

Fig. 8.8 shows a good overall agreement between simulation and experiment for both modes considered. The axial mode (Fig. 8.8 left) has shown in experiments a relatively low amplitude because of the absence of resonance in the frequency domain of interest. This can be observed in the plenum chamber where the measured amplitude decreases with increasing frequency. This trend is more pronounced above 200 Hz and is caused by the development of the 1st order azimuthal mode with the eigenfrequency at 250 Hz. The acoustic model reflects qualitatively and quantitatively this trend until 200 Hz. Above this, the amplitude of the calculation deviates slightly from the measurement showing a less stronger decrease. The simulated phase curve shows a better agreement. A local deviation from the measurement can be seen around 250 Hz, which may be partly due to an incomplete modal decomposition.

In the case of the azimuthal mode (Fig. 8.8 right), the results of the model simulations show also good consistency with the measurement. At frequencies away from the resonance band, the measured amplitude in the plenum is small compared to the combustion chamber. With approaching the eigenfrequency of 250 Hz, it rises strongly and at 270 Hz a local maxima is found being even higher than in the combustion chamber. Further increasing the frequency over the resonant range, the amplitude in the plenum drops again and becomes relatively low. The acoustic model reflects these trends qualitatively and quantitatively very well in the entire frequency range. The model

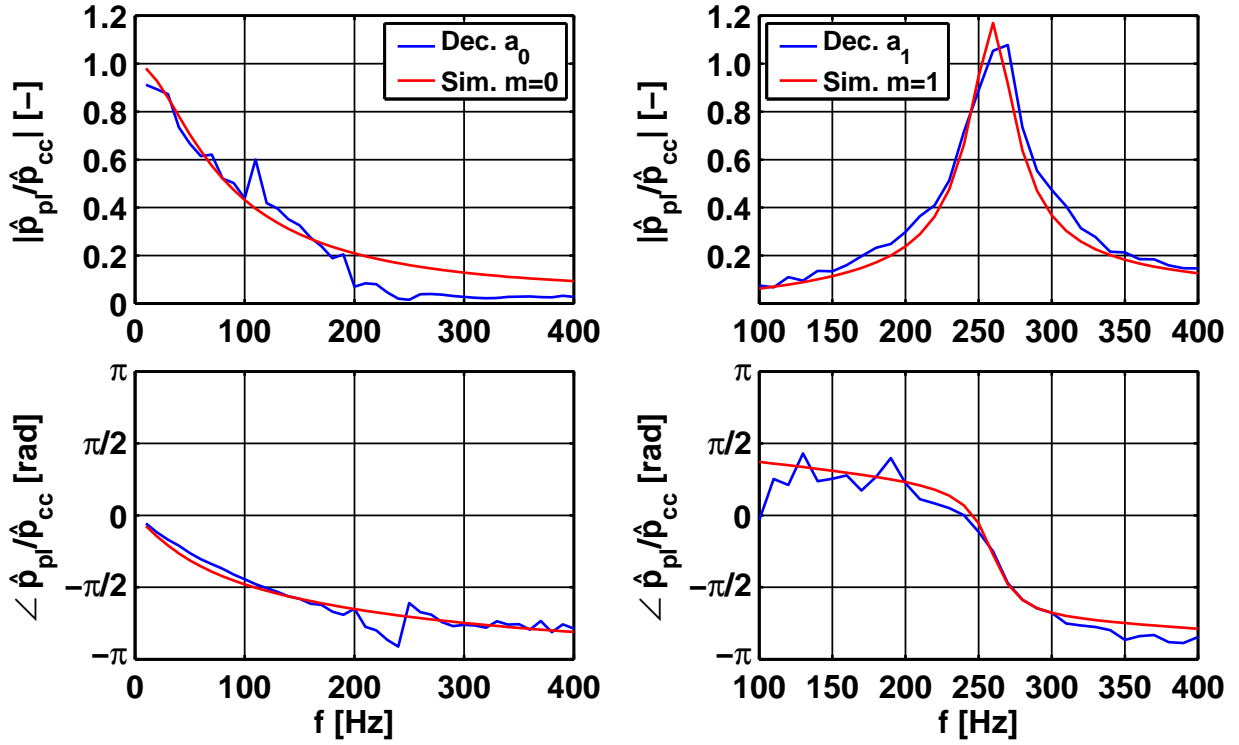


Figure 8.8: Relative amplitude of the measured (Dec.) and simulated (Sim.) axial (left) and 1st order azimuthal (right) components in the plenum with respect to the combustion chamber

predicts a slightly stronger amplitude increase in the plenum than in the combustion chamber at the resonance and the local maximum lies here at 260 Hz, a little lower than in the measurements. This behaviour of the azimuthal mode indicates a stronger damping effect in the combustion chamber than in the plenum. The acoustic model reproduces well this effect. Different values of the reflection coefficients implemented for the inlet and outlet side are the basis for this observation. On the plenum side (inlet) the reflection coefficient was set (Chapter 7.2) to unity corresponding to a fully reflective acoustic boundary. On the combustion chamber side (outlet) the reflection coefficient of the exit nozzles corresponds, according to Fig. 7.3, to a partially reflective acoustic boundary. For the isothermal flow, the eigenfrequencies of the azimuthal modes are equal in both combustion chamber and plenum due to the same sound velocity.

The azimuthal distribution of the decomposed (Dec.) and simulated (Sim.) acoustic pressure fields in the combustion chamber and plenum are presented at 130 Hz for the axial component (Fig. 8.9) and at 260 Hz for the 1st order azimuthal component (Fig. 8.10). Additionally, the totally decomposed (Dec. total) acoustic field $\hat{p}(\theta)$ (Eqn. 7.2) and the directly measured data (Exp.) have been plotted. For each modal component, the acoustic pressures along the circumference $\hat{p}(\theta)$ have been normalised with the value at the respective reference position $\theta_{ref} = 30^\circ$ in the combustion chamber. Consequently, the azimuthal phase distribution in the plenum shows a constant shift with respect to the downstream side. This is for the axial mode -0.57π at 130 Hz and for the azimuthal mode -0.27π at 260 Hz. In Figs. 8.9 and 8.10 the directly measured data from the dynamic pressure transducers has also been plotted as amplitude factors and phase differences with respect to the reference sensor (Exp. ref).

The axial mode is constant along the circumference and corresponds to the decomposed complex modal amplitude a_0 . The azimuthal distribution of the acoustic pressure \hat{p} for the simulated 1st order azimuthal mode (Fig. 8.9) is described by the equation

$$\hat{p}(x_{cc}, \theta) = \bar{\rho}c \cos(\theta - \theta_1) \left(F e^{-ik_x^+ x_{cc}} + G e^{-ik_x^- x_{cc}} \right) \quad (8.1)$$

which has been derived from Eqn. 5.54 after setting the mode index to one ($m = 1$) and transferring the Cartesian coordinate y in the azimuthal coordinate θ . The complex parameters F and G are the fundamental waves characterising a 2D acoustic field of a thin annular duct where the azimuthal modes are standing (Eqn. 5.54). These parameters have been calculated at the axial positions where the acoustic response have been measured, i.e. x_{cc} in the combustion chamber and x_{pl} in the plenum chamber, respectively. In order for the simulated and measured azimuthal modes to have the same azimuthal origin, the azimuthal position θ_1 of the decomposed mode a_1 has been added in the cosine function of Eqn. 8.1.

Fig. 8.10 shows also that the simulation predicts a higher amplitude in the plenum than in the combustion chamber for the azimuthal component at 260

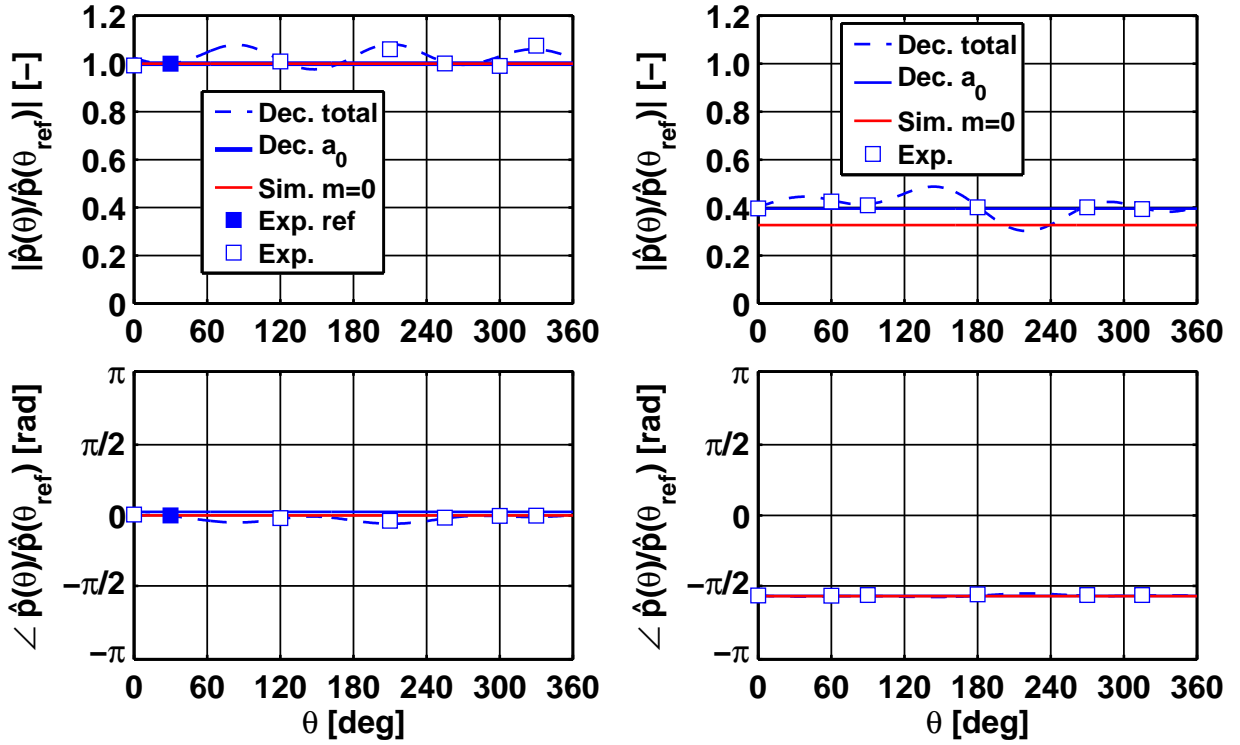


Figure 8.9: Azimuthal distribution of \hat{p} for the decomposed (Dec. a_0) and simulated (Sim. $m = 0$) axial modes in the combustion chamber (left) and plenum (right) at 130 Hz. Additionally, data (Exp.) measured at 130 Hz is plotted

Hz as it has already been observed in Fig. 8.8 right. The slight discrepancies between the measured data (Exp.) and decomposed modes (Dec.) in Figs. 8.9 and 8.10 indicate the presence of other modal components beside a_0 and a_1 . These have nevertheless an insignificant contribution to the total signal.

The results of the model based analysis presented in this section tend to the conclusion that the acoustic model of the annular combustor describes the dynamic behaviour of the test rig under cold isothermal conditions for both the axial and azimuthal modal components very well. Consequently, it can be followed that the free parameters of the burner model ζ and l_{eff} have been determined with high accuracy. The values of ζ and l_{eff} are presented in Chapter 8.3.3 (Tab. 8.7).

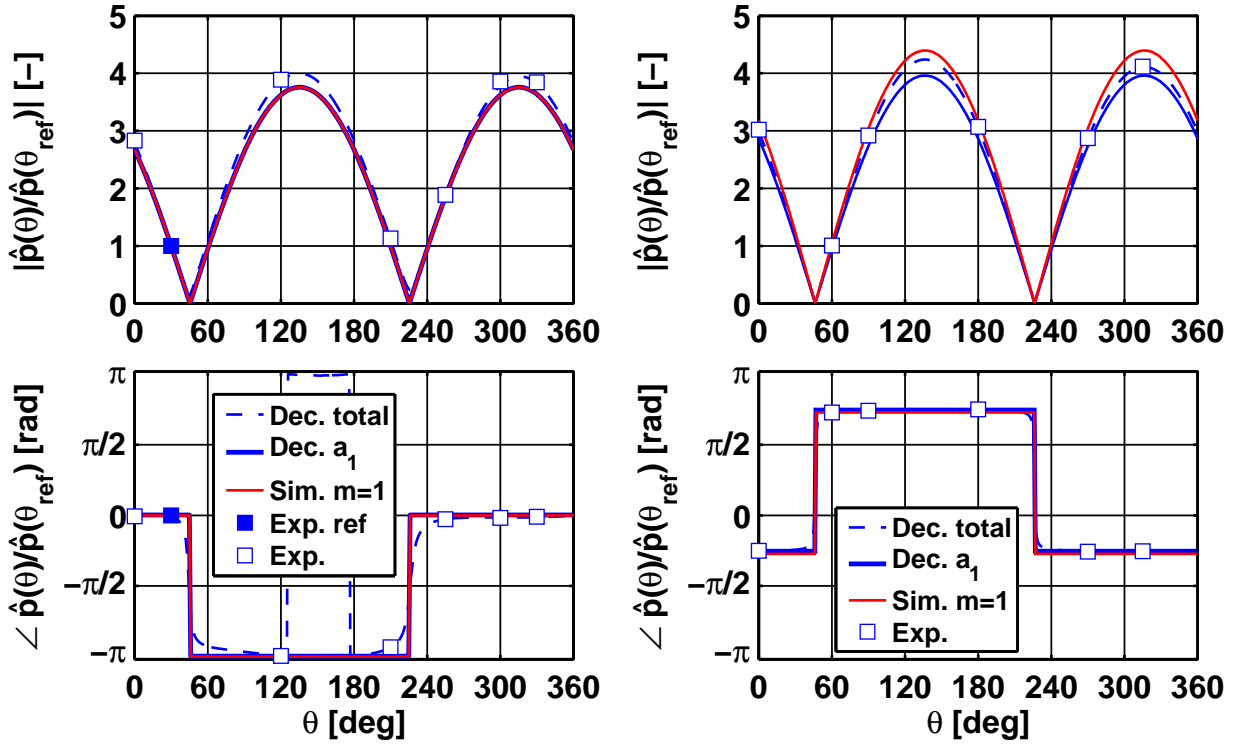


Figure 8.10: Azimuthal distribution of \hat{p} for the decomposed (Dec. a_1) and simulated (Sim. $m = 1$) 1st order azimuthal modes in the combustion chamber (left) and plenum (right) at 260 Hz. Additionally, data (Exp.) measured at 260 Hz is plotted

8.3 Determination of the FTF

The determination of the free parameters n , τ , σ , τ_ϕ and σ_ϕ of the flame transfer function model was made by means of a model based analysis of the experimental data, similarly to the cold isothermal case. The acoustic measurements with flame were performed with the EV5 burner in PPM as well as IPM operation. The dynamic pressure transducers were distributed azimuthally on the outer wall of the combustion chamber and plenum. The acoustic pressure measurements in the presence of flame differed from the cold case mainly in the longer recording times stretching up to 100 seconds/frequency for every sensor. The longer time domain series were necessary for the post processing procedure to suppress the broad band stochastic combustion noise and

obtain stable results. Additionally to the dynamic pressure, the optical measurement technique presented in Chapter 4.3.2 has been employed for optical flame characterisations.

The operation of the annular combustor with flame posed the problem of thermo-acoustic stability of the system. Hence, the acoustic measurements for the determination of the FTF were performed at stable operation points where the annular combustor exhibited no self sustained acoustic pulsations. The operating parameters for the acoustic measurements with flame are given in Tab. 8.3 for the PPM and in Tab. 8.5 for the IPM. The results of the measured acoustic pressure field for the reacting flow are going to be presented in the following paragraphs.

8.3.1 Perfectly Premixed Mode Operation (PPM)

Fig. 8.11 shows the frequency response function of the measured dynamic signals in the combustion chamber under axial excitation for the PPM.

Table 8.3: Operating parameters of the annular combustor in the PPM

Operating parameters	
Preheating temperature T_{pl} [K]	573
Thermal power P_{th} [kW]	860
Equivalence ratio ϕ [-]	0.57
Excitation type	axial

Towards the lower frequency limit (10 Hz), where the acoustic wavelengths are much longer than the combustor length, the measured acoustic pressure field shows equal phases in the combustion chamber and plenum. Furthermore, the amplitudes are equal as well. This is due to the fact that in the lower frequency regime, a bulk mode oscillates in the whole combustor. This is characterised by large amplitudes in the frequency spectra of the absolute acoustic pressure \hat{p} . With increasing frequency, the amplitude and phase drop continuously on the plenum side relative to the combustion chamber. This trend can be explained as the combined effects of the the acoustic excitation made

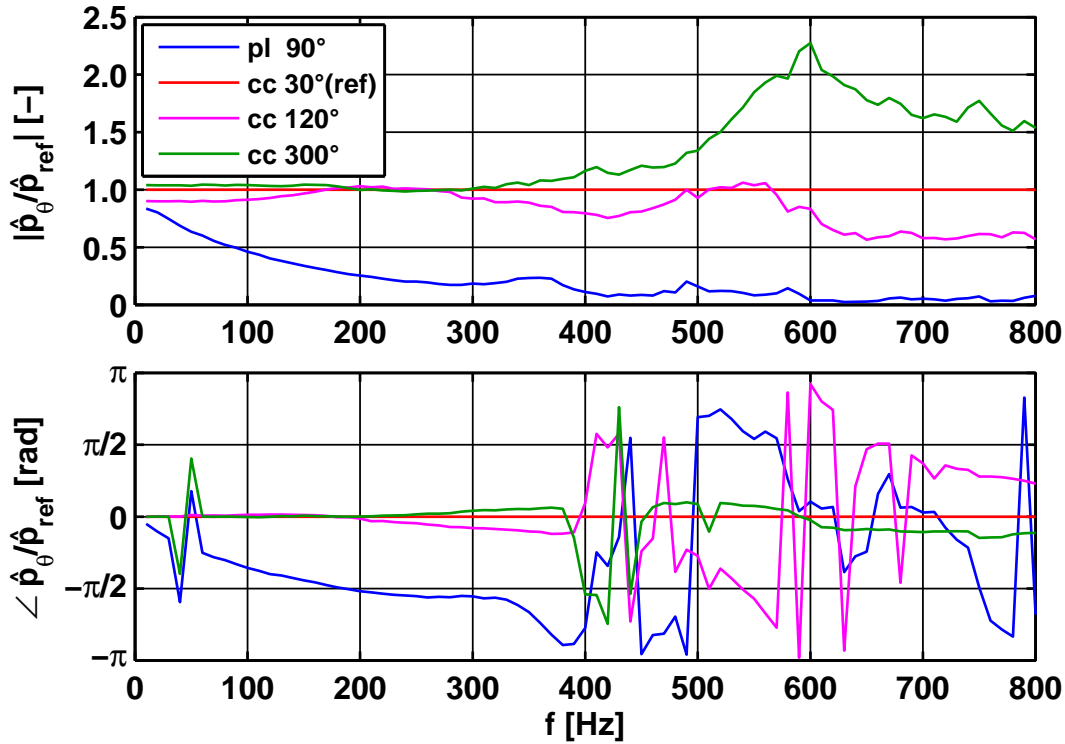


Figure 8.11: Frequency response function of the measured acoustic pressure \hat{p} in the combustion chamber and plenum in the PPM under axial excitation

from the downstream side, the acoustic losses and the inertia effects generated in the burner ring and the flame dynamics. The measured BFTM of the EV5 burner, presented by Alemela [5], has shown a dynamic behaviour especially of the element T_{12} , which relates the acoustic pressure in the combustion chamber \hat{p}_{cc} with the acoustic velocity in the plenum. The amplitude of this element increases in the frequency range 0-600 Hz due to the inertia effects in the burner. For the case presented in Fig. 8.11, which relates the upstream side (plenum) to the downstream side (combustion chamber), this explains the dropping amplitude in the plenum with respect to the combustion chamber. Furthermore, this effect is amplified by the external excitation which is made in the ACC from the downstream side. Hence, the acoustic losses over the burner ring yield lower oscillation amplitudes in the plenum than in the combustion chamber.

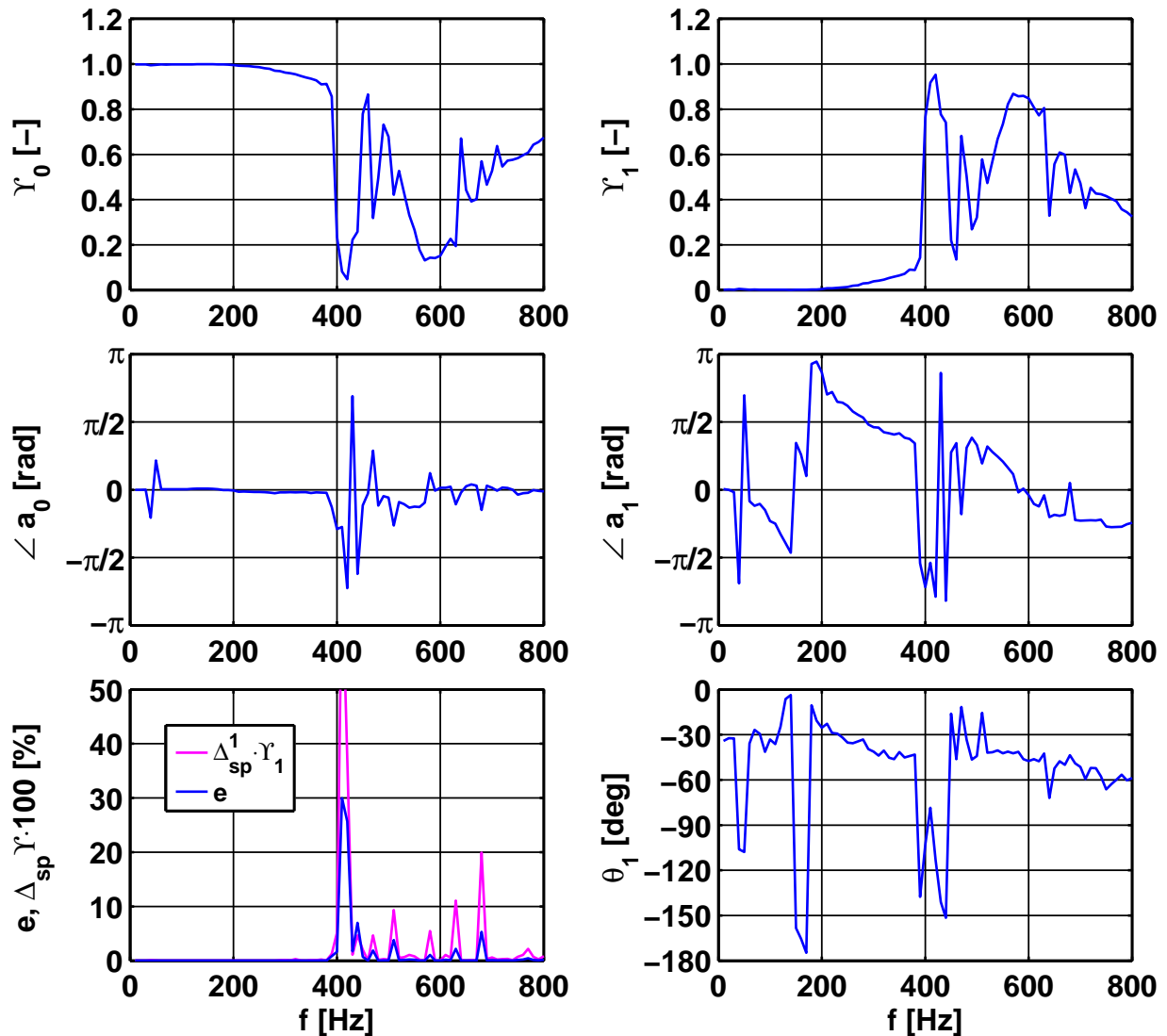


Figure 8.12: Modal decomposition in the combustion chamber for the PPM

In the combustion chamber the amplitude and phases of the acoustic pressure measured along the circumference are equal in the frequency domain between 100 and 300 Hz (Fig. 8.11). This indicates the dominant presence of an axial modal component in the acoustic field. For frequencies above 400 Hz the trend shows variations between the acoustic pressure amplitudes along the circumference and a pronounced tendency for $\pm\pi$ jumps in the phase curves, a behaviour which is characteristic for an azimuthal mode.

The observations made on the basis of the directly measured data are further supported by the results of the modal analysis in the combustion chamber presented in Fig. 8.12. These show a dominant axial component a_0 for frequencies below 400 Hz. In the upper frequency regime, the relative contribution of a_0 decreases with respect to the 1st order azimuthal mode a_1 which has maxima at 420 and 570 Hz. At 400 Hz the acoustic field switches between the axial and the 1st order azimuthal component and is characterised by a relatively high spinning tendency (Δ_{sp}^1). This can be seen from the lower left plot of Fig. 8.12. In this region, the error e of the modal decomposition is relatively large with 30% at 420 Hz. Therefore, the results of the modal decomposition in the frequency domain from 400 to 450 Hz shall not be considered for further analysis. In the rest of the spectrum, the spinning tendency is much lower and more pronounced only at isolated frequencies; hence the results of the modal decomposition are considered to be valid. An important aspect to be noticed is that the error e corresponds very well with the spinning tendency of the acoustic field, i.e. the frequencies where e is larger are characterised by a higher spinning tendency. The maximum at 570 Hz corresponds to the eigenfrequency of the 1st order azimuthal mode. Thus, the acoustic field is dominated by the azimuthal component with $\Upsilon_1 = 87\%$ (see Fig. 8.12 right). The rest consists of the axial component (see Fig. 8.12 left), which pulsates due to the external excitation.

Compared with the cold acoustic measurements presented in Chapter 8.1, where the azimuthal modes develop similarly in the combustion chamber and plenum, in the case with flame the eigenfrequency at 570 Hz mentioned above corresponds to the 1st order azimuthal mode in the combustion chamber. The 1st order azimuthal mode in the plenum has the eigenfrequency below 570 Hz due to the lower temperature and is strongly damped. Nevertheless, the mode develops at 570 Hz in the plenum chamber as well but with a lower amplitude. In the following, when the 1st order azimuthal mode in the case with flame will be referred to, it will be self understood that this corresponds to the the combustion chamber side. Concerning the axial modes, these develop in both combustion chamber and plenum for the isothermal flow as well as with flame, i.e. from the upstream acoustic boundary (plenum inlet) to the downstream acoustic boundary (exit nozzle).

Table 8.4: Simulation parameters for the PPM

Mode index m	0	1
$M_{pl}[-]$	0.006	0.006
$c_{pl}[m/s]$	480	480
$\rho_{pl}[kg/m^3]$	0.97	0.97
$M_b[-]$	0.05	0.05
$c_b[m/s]$	480	480
$\rho_b[kg/m^3]$	0.97	0.97
$M_{cc}[-]$	0.02	0.02
$c_{cc}[m/s]$	800	800
$\rho_{cc}[kg/m^3]$	0.33	0.33
$x_{pl}[mm]$	-220	-220
$x_{cc}[mm]$	50	50
Experiment	Tab. 8.3	Tab. 8.3

Figs. 8.11 and 8.12 show that the annular combustor has in the PPM two eigenfrequencies in the range 0-800 Hz, the axial and the 1st order azimuthal. Hence, the 1st order azimuthal mode develops with axial excitation as well. This implies that the experimental data for the axial and the 1st order azimuthal modes, which are necessary for the validation of the acoustic model, can be obtained from the acoustic measurements made with axial excitation alone. Additional measurements when the system is being pulsated azimuthally are not required, which saves time and effort. These have been carried out nevertheless and the results have shown that the 1st order azimuthal mode develops similarly and is independent of the excitation type. The only obvious difference observed was the slightly higher modal amplitude with azimuthal excitation. This was due to the fact that the azimuthal mode was pulsated directly and thus, the axial component was less present.

The parameters of the simulation are given in Tab. 8.4. The model based analysis of the experimental data for the PPM is presented in Fig. 8.13 as calculated and measured acoustic pressure fields for the axial (left) and 1st order azimuthal (right) modes. The results are plotted, similarly to the cold isothermal case, as amplitude factors and phase difference in the plenum with respect to the combustion chamber. In the case of the axial mode, the agreement is

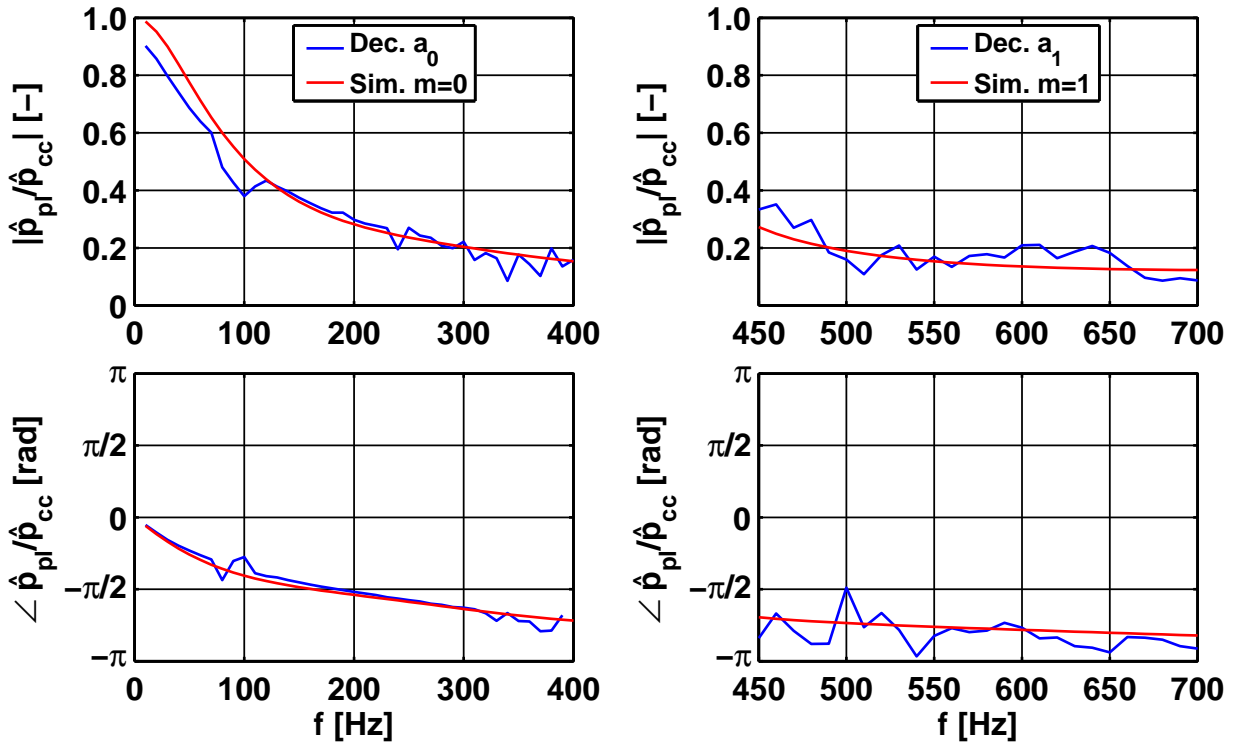


Figure 8.13: Relative amplitude of the measured (Dec.) and simulated (Sim.) axial (left) and 1st order azimuthal (right) components in the plenum with respect to the combustion chamber for the PPM

gut with some local inconsistencies in the lower frequency domain. The amplitude in the plenum shows in general a decreasing trend with respect to the combustion chamber. Towards the lower frequency limit, the phase converges to zero as expected for large acoustic wavelengths. For the 1st order azimuthal component, a good agreement between experiment and computation on the frequency domain considered is achieved. Even though the amplitude and phase of the decomposed azimuthal mode scatter, due to the relatively low signal in the plenum chamber, the general decreasing trend can be easily recognised. This is well reflected by the simulation in the frequency range considered.

The acoustic model describes the azimuthal distribution of the axial and 1st order azimuthal components. The results are presented in Figs. 8.14 and 8.15

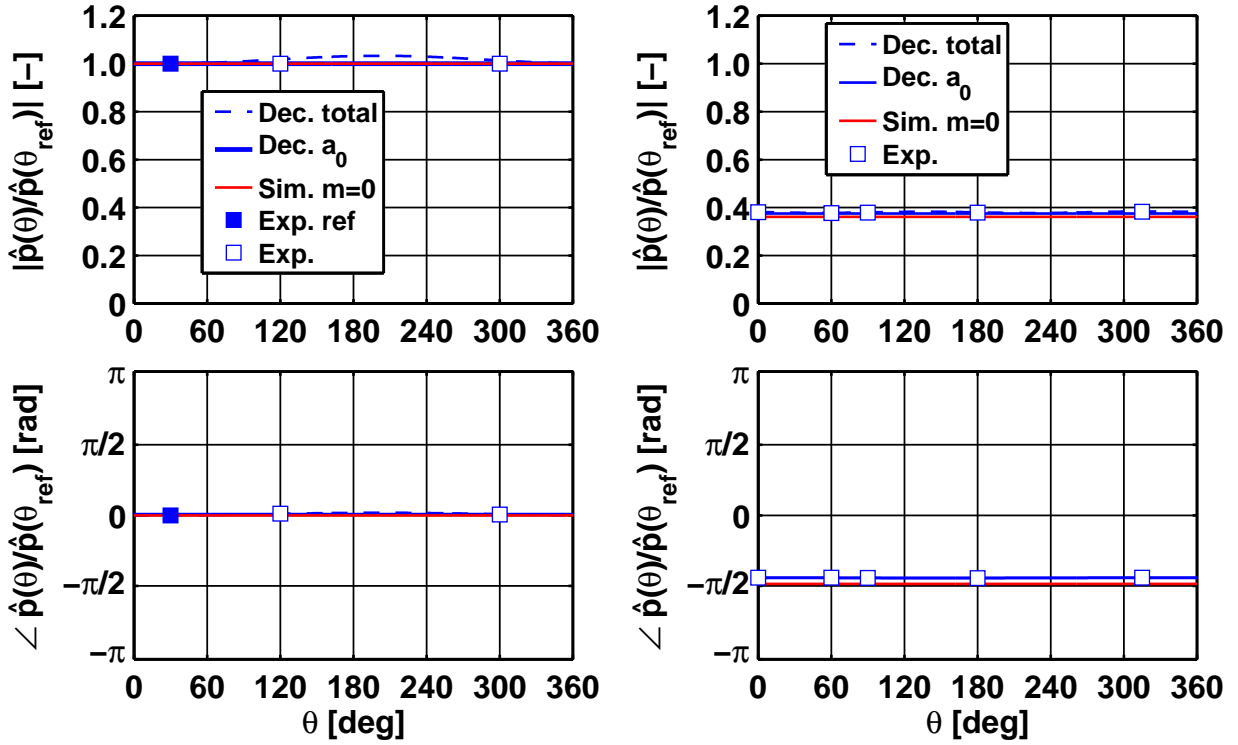


Figure 8.14: Azimuthal distribution of \hat{p} for the decomposed (Dec. a_0) and simulated (Sim. $m = 0$) axial modes in the combustion chamber (left) and plenum (right) at the frequency of 150 Hz. Additionally, data (Exp.) measured at 150 Hz is plotted

at one frequency only; 150 Hz for the axial and 570 Hz for the 1st order azimuthal. Additionally, the correspondent decomposed mode a_k , the totally decomposed (Dec. total) acoustic field $\hat{p}(\theta)$ (Eqn. 7.2) and the directly measured data (Exp.) have been plotted as reference. The complex acoustic pressures of the simulation, decomposition and experiment have been normalised with the corresponding values at the reference azimuthal position $\theta_{ref} = 30^\circ$ in the combustion chamber. The azimuthal distribution of \hat{p} for the axial component (Fig. 8.14) is constant in both, combustion chamber and plenum. In case of the 1st order azimuthal component (Fig. 8.15) the typical form with two nodes and anti nodes on the circumference can be recognised. The difference between the decomposed mode a_1 and the measured signal (Exp.) in Fig. 8.15 indicates the presence of an axial component. This agrees with the results

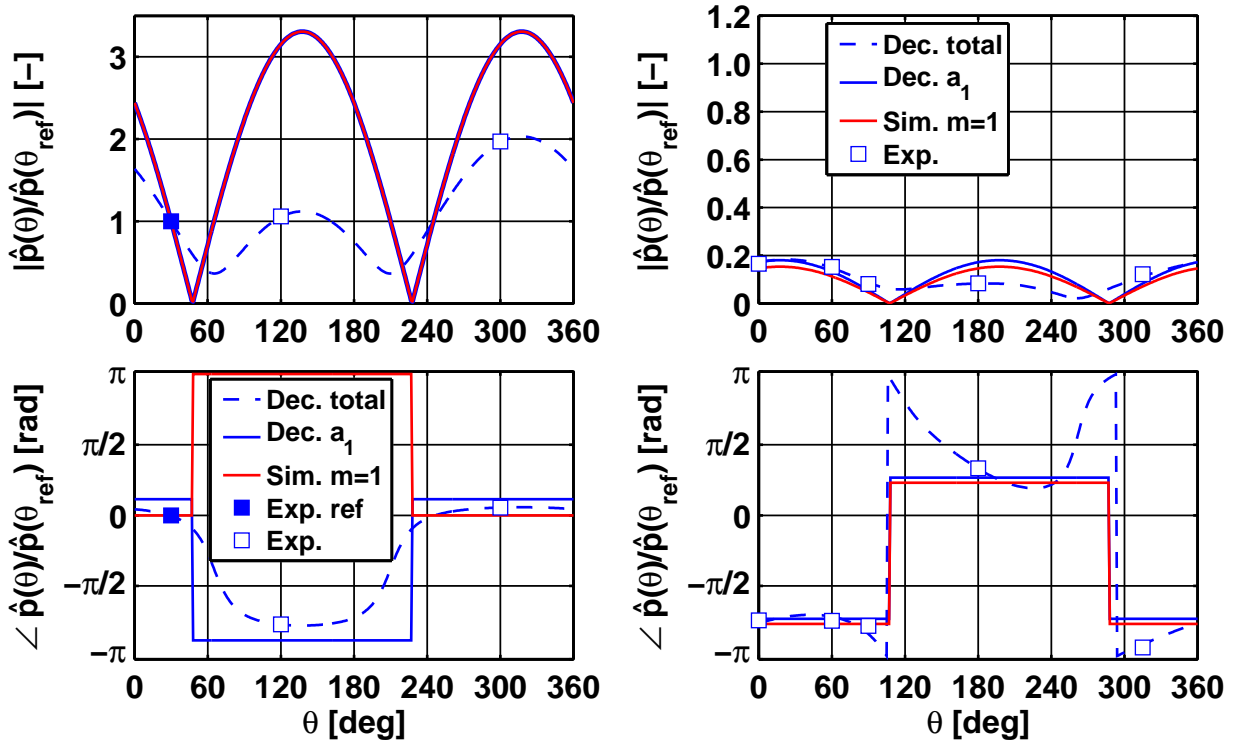


Figure 8.15: Azimuthal distribution of \hat{p} for the decomposed (Dec. a_1) and simulated (Sim. $m = 1$) 1st order azimuthal modes in the combustion chamber (left) and plenum (right) at the frequency of 570 Hz. Additionally, data (Exp.) measured at 570 Hz is plotted

of the modal decomposition, presented previously in Fig. 8.12, which showed that at 570 Hz both 1st azimuthal (a_1) and axial (a_0) components contribute in the total acoustic field.

8.3.2 Injector Premixed Mode Operation (IPM)

The measured data for the IPM is presented in Fig. 8.16. The operating parameters of the test rig are given in Tab. 8.5. Compare to the PPM, in the IPM the EV5 burner has exhibited stable operation for richer air-fuel mixtures. Therefore, for similar air mass flow rates and preheating temperatures, the equivalence ratio and consequently the thermal power are higher in the IPM.

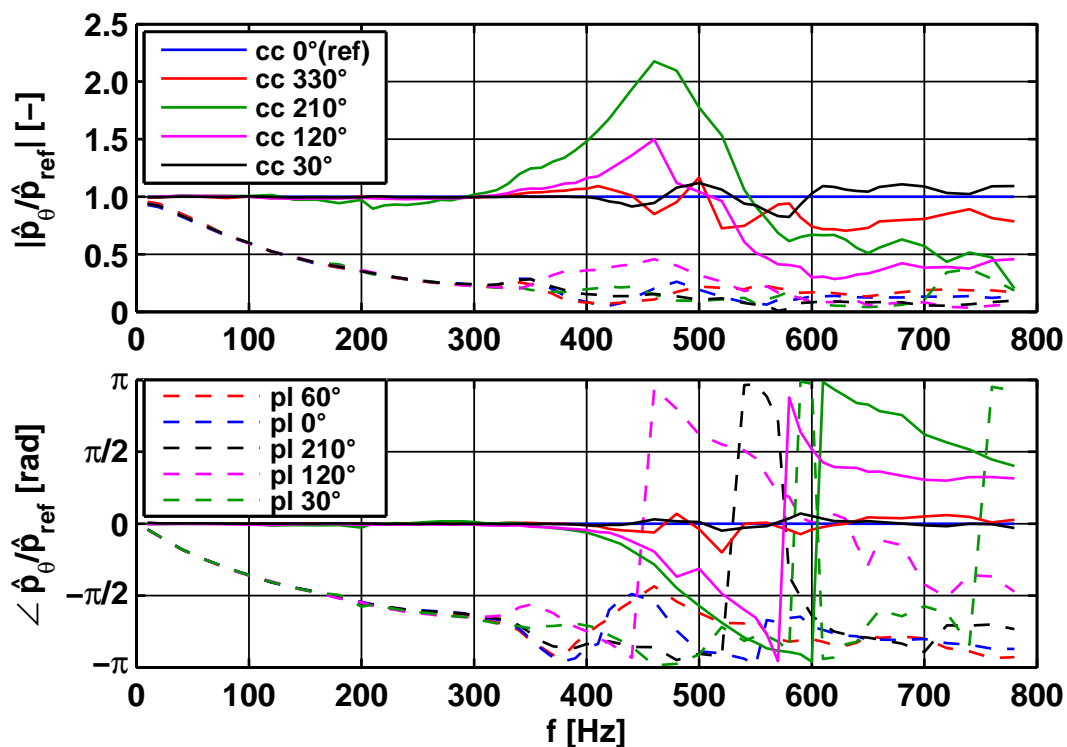


Figure 8.16: Frequency response function of the measured \hat{p} in the combustion chamber and plenum in the IPM under axial excitation

Table 8.5: Operating parameters of the annular combustor in the IPM

Operating parameters	
Preheating temperature T_{pl} [K]	573
Thermal power P_{th} [kW]	1025
Equivalence ratio ϕ [-]	0.68
Excitation type	axial

Similarly to the PPM, in the IPM the acoustic field of the annular combustor is characterised towards the lower frequency limit by equal amplitudes and phases between the upstream and downstream side of the burner ring and by a dropping signal with increasing frequencies in the plenum relatively to the combustion chamber. The resonant range for the axial mode - equal amplitudes and phases along the circumference in both combustion chamber and plenum - extends here to higher frequencies than in the PPM. These obser-

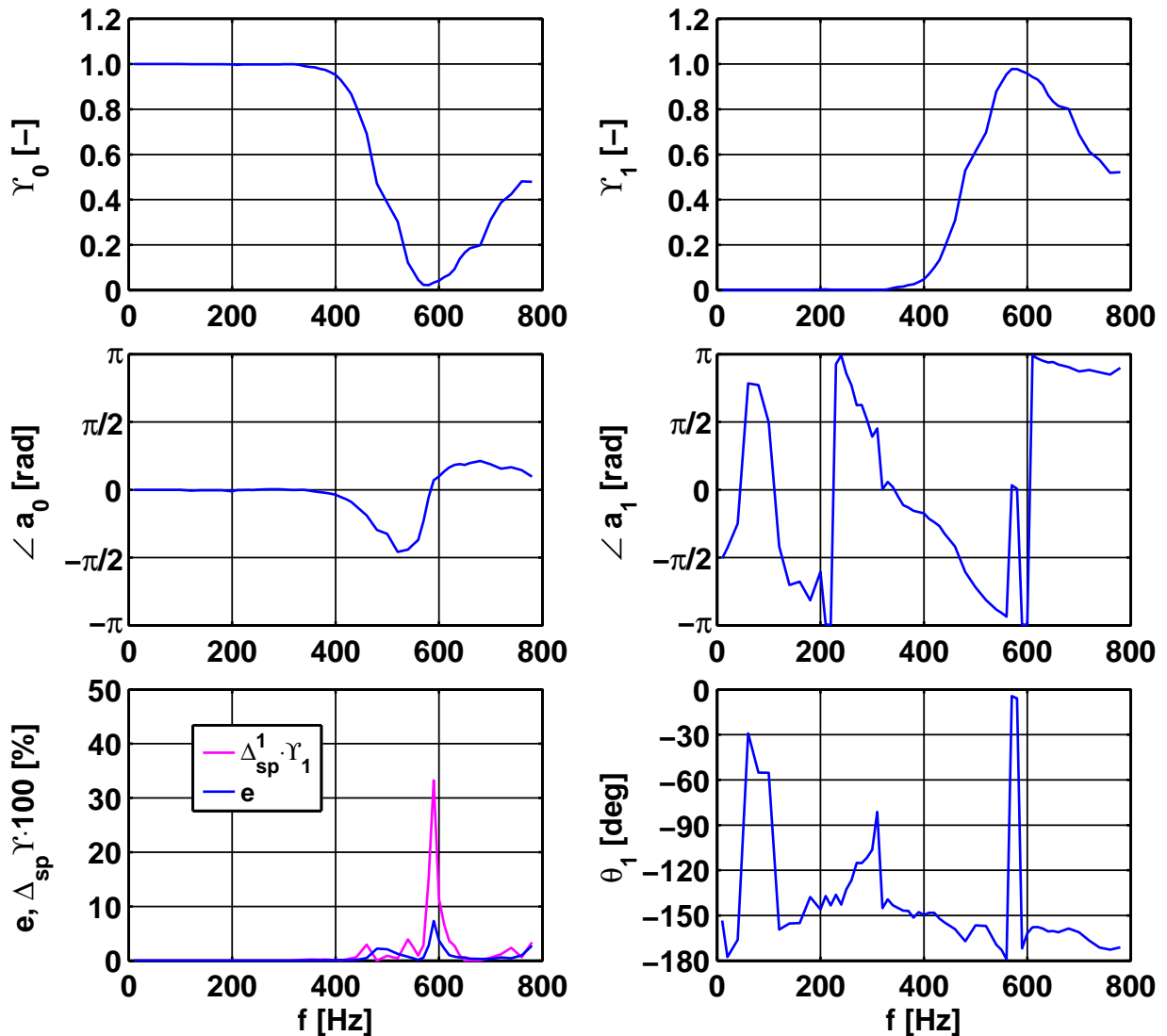


Figure 8.17: Modal decomposition in the combustion chamber for the IPM

variations are confirmed by the results of the modal analysis in the combustion chamber (Fig. 8.17) which show a dominant axial modal component a_0 until 400 Hz. For higher frequencies the acoustic field switches from the axial to the 1st order azimuthal component a_1 . Qualitatively seen, the development of the azimuthal component is similar to the PPM; in the first half of the frequency range the mode is strongly cut-off. Above 400 Hz, the amplitude rises strongly and records a maximum at the eigenfrequency of 570 Hz. Compared to the PPM case (see Fig. 8.12) the relative contribution of the azimuthal component γ_1

in the total signal power is much larger at the eigenfrequency. The measured acoustic field exhibits a high spinning tendencies in a relatively narrow domain around the eigenfrequency. This produces errors in the modal decomposition procedure.

Table 8.6: Simulation parameters for the IPM

Mode index m	0	1
$M_{pl}[-]$	0.006	0.006
$c_{pl}[m/s]$	480	480
$\rho_{pl}[kg/m^3]$	0.97	0.97
$M_b[-]$	0.05	0.05
$c_b[m/s]$	480	480
$\rho_b[kg/m^3]$	0.97	0.97
$M_{cc}[-]$	0.021	0.021
$c_{cc}[m/s]$	850	850
$\rho_{cc}[kg/m^3]$	0.3	0.3
$x_{pl}[mm]$	-220	-220
$x_{cc}[mm]$	110	110
Experiment	Tab. 8.5	Tab. 8.5

The parameters of the simulation for the IPM are given in Tab. 8.6. Note that in both PPM and IPM, a mean velocity of sound c_{cc} was chosen for the combustion chamber. In the IPM mode, this is slightly larger than in the PPM mode due to the fact that the equivalence ratio was higher as well. As in the case of the PPM, in the IPM the experimental data corresponding to the axial and the 1st order azimuthal modes were measured in one experimental campaign made with axial excitation only. The results of the modal based analysis are presented in Fig. 8.18 for the axial (left) and the 1st order azimuthal (right) modal components. The two modes are plotted only in the range where their contribution to the total signal power is dominant, i.e. frequencies below 400 Hz for the axial mode and between 400 Hz and 700 Hz for the 1st order azimuthal mode. The acoustic model reproduces the dynamic behaviour of the annular combustor very well at the lower frequency limit. In this frequency range the system oscillates in bulk mode and the amplitudes and phases in the combustion chamber and plenum are equal. For increasing frequency, the simulation captures well the falling amplitude and phase in the plenum rela-

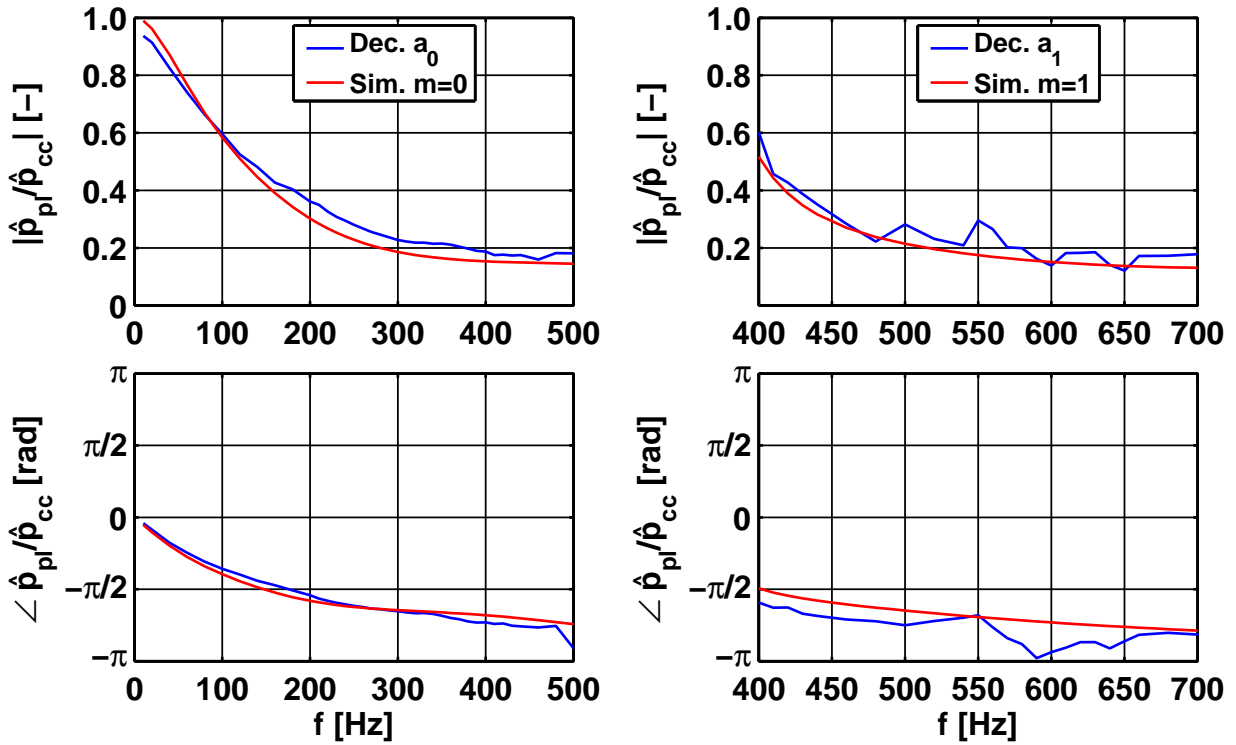


Figure 8.18: Relative amplitude of the measured (Dec.) and simulated (Sim.) axial (left) and 1st order azimuthal (right) components in the plenum with respect to the combustion chamber for the IPM

tively to the combustion chamber. A good agreement is achieved as well in the case of the azimuthal mode. Here, as in the PPM, the decomposed experimental data shows some scatter which is due to the relatively low amplitudes on the plenum side. This tends to increase the errors when calculating the complex amplitude ratio.

As the acoustic field exhibits a relatively large spinning azimuthal component around the eigenfrequency of 570 Hz, the capability of the acoustic model to reproduce correctly the dynamic behaviour of the annular combustor must be questioned in this frequency range.

The azimuthal distribution of the decomposed (Dec.) and simulated (Sim.) acoustic pressures for the axial and 1st order azimuthal components are presented in Fig. 8.19 at 300 Hz and in Fig. 8.20 at 570 Hz, respectively. Addition-

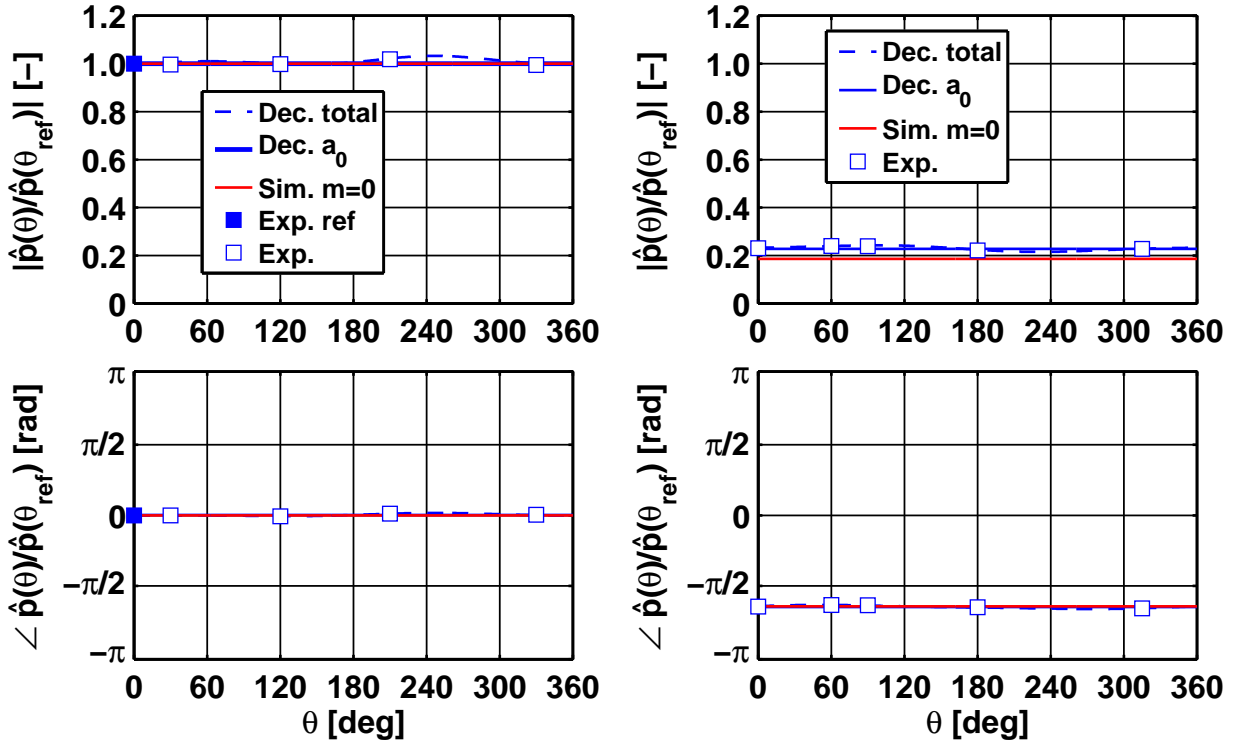


Figure 8.19: Azimuthal distribution of \hat{p} for the decomposed (Dec. a_0) and simulated (Sim. $m = 0$) axial modes in the combustion chamber (left) and plenum (right) at the frequency of 300 Hz. Additionally, data (Exp.) measured at 300 Hz is plotted

ally, the totally decomposed (Dec. total) acoustic field $\hat{p}(\theta)$ (Eqn. 7.2) and the directly measured data (Exp.) have been plotted as a reference. Similarly to the results for the PPM, the complex acoustic pressure of the simulation, decomposition and experiment are normalised with the corresponding values at the reference azimuthal position $\theta_{ref} = 0^\circ$. The perfect agreement between simulation, decomposition and measured data at 300 Hz (Fig. 8.19) confirms the dominant axial mode on both sides of the burner ring. In the case of the azimuthal mode at 570 Hz (Fig. 8.20), some discrepancies can be noticed especially in the phase plot on the plenum side. These large differences between the decomposed mode and the measured data (Exp.) are due to the presence of relatively large spinning components corresponding to the 1st order azimuthal mode around the eigenfrequency (see Fig. 8.17).

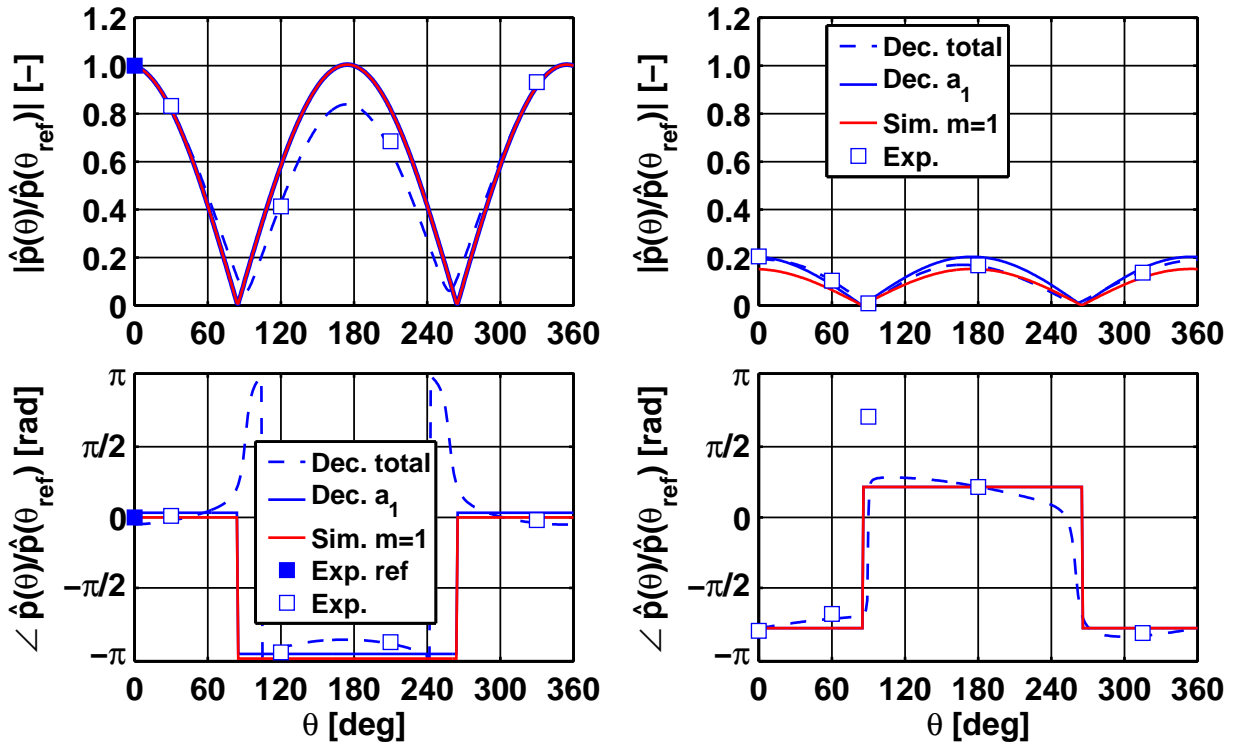


Figure 8.20: Azimuthal distribution of \hat{p} for the decomposed (Dec. a_1) and simulated 1st order azimuthal (Sim. $m = 1$) modes in the combustion chamber (left) and plenum (right) at the frequency of 570 Hz. Additionally, data (Exp.) measured at 570 Hz is plotted

8.3.3 Conclusions and Discussions

The results of the model based analysis presented in the previous sections demonstrate that the acoustic model is capable to reproduce well the dynamic behaviour of the annular combustor for both modal components considered. For some frequencies though, where the measurement analysis has shown higher spinning tendencies the acoustic model reaches its limitations. In general it can be concluded that the analytical models of the burner and flame transfer matrices are sufficient to represent the burner and flame dynamic behaviour in the annular combustor. The model parameters which were determined by the model based regression are presented in Tab. 8.7

Table 8.7: Burner and flame parameters for PPM and IPM

Operation mode	Burner model		Flame model					X_{OHmax}/d_0 [-]
	ζ [-]	l_{eff} [m]	n [-]	τ [ms]	σ [ms]	τ_ϕ [ms]	σ_ϕ [ms]	
PPM	14	0.06	2.2	2.3	0.57			0.94
IPM			2.6	0.88	0.31	2.13	0.55	0.72

The burner model is the same for both PPM and IPM, as it was determined from the acoustic investigations on the cold isothermal flow presented in Chapter 8.2. The pressure loss coefficient is $\zeta = 14$ and is related to the cross-section of the burner A_b with the nominal diameter d_0 (see Chapter 7.2). The value of the parameter l_{eff} describing the inertia effects in the burner is 0.06 m. The comparison of the burner parameters with the results obtained with the same method in the SCC are presented in Chapter 8.3.4.

For the flame, the model parameters thus obtained are clearly different for the two operational modes. For the PPM these are $\tau = 2.3\text{ms}$ and $\sigma = 0.57\text{ms}$. The normal distribution σ is plotted in Fig. 8.21 (cyan curve) together with the time averaged axial distribution (blue curve) of the OH*-chemiluminescence measured in stationary conditions. The directly measured time averaged distribution of the OH*-chemiluminescence is presented colour coded in Fig. 8.21 left. In the IPM, the mean convective time delay of the flow instabilities is $\tau = 0.88\text{ms}$ with the normal distribution $\sigma = 0.31\text{ms}$. The mean convective time delay of the equivalence ratio waves is much larger $\tau_\phi = 2.13\text{ms}$ with $\sigma = 0.55\text{ms}$. This agrees qualitatively with the results from the SCC measurements [5] where τ_ϕ was also larger than τ .

In the ACC, the values of the mean convective time delay τ is in the IPM smaller by a factor 0.38 than in the PPM (Tab. 8.7). This large difference cannot be fully explained by the higher equivalence ratio in the IPM with respect to the PPM (see Tab. 8.5 and Tab. 8.3), which results in more compact flames (see Fig. 8.22) and consequently shorter mean convective time delays. As it can be seen in Tab. 8.7 the X_{OHmax} in the IPM is only 0.77 of the value in the PPM. However, care must be taken when considering the OH*-chemiluminescence intensity for flames characterised by mixture inhomogeneities. As explained

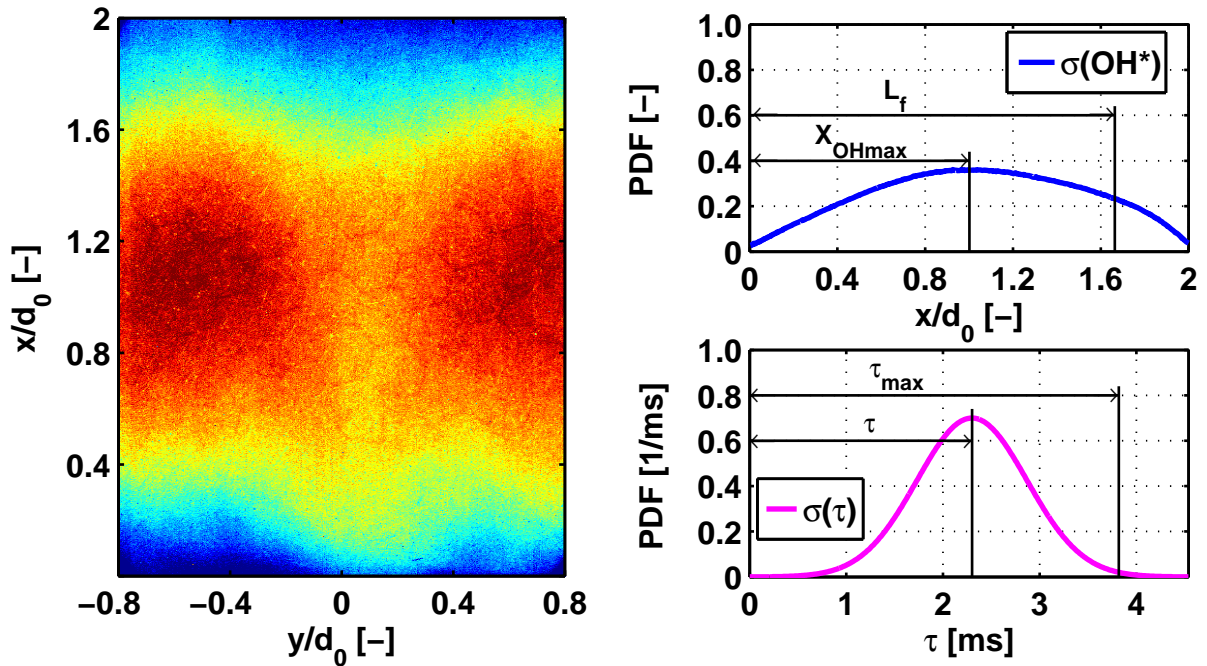


Figure 8.21: Left: time averaged distribution of the OH*-Chemiluminescence in the PPM. Right: PDF of the OH*-Chemiluminescence distribution and of the normal distribution σ in the PPM

in [7] and [55] the chemiluminescence signal of a flame with equivalence ratio fluctuations is over predicted. The difference between the values of τ in the IPM and PPM in the ACC is relatively large compared to the results from the SCC [5] where τ in the IPM is still smaller but much closer to τ in the PPM. Furthermore, in the work of Schuermans et al. [55], where the model $(n - \tau - \sigma - \phi)$ was introduced and applied for the EV burner, a similar construction with the EV5, the relation between the mean convective time delays in the IPM and PPM is similar to the results from the SCC [5].

An explanation for these inconsistencies can be found in the formulation of the flame model $(n - \tau - \sigma - \phi)$. The model presented in Eqn. 6.17 assumes the origin of the equivalence ratio waves and mass flow rate fluctuations to be at the same axial position, i.e. the burner exit plane where the input upstream acoustic parameters \hat{p}_u and \hat{u}_u are considered. For the EV5 burner though, this assumption may not necessarily correspond to the real operating con-

ditions. The equivalence ratio waves are generated in the conus of the EV5 burner where the fuel is injected and mixed with the air. The flow rate fluctuations are triggered more downstream at the burner exit, i.e. at the area expansion into the combustion chamber. Due to this, the flame parameters for the IPM cannot be physically related to the geometrical lengths characterising the burner and flame and also to the flame parameters in the PPM. Consequently, it is concluded here that the model presented in Eqn. 6.17 does not represent correctly the flame in the IPM.

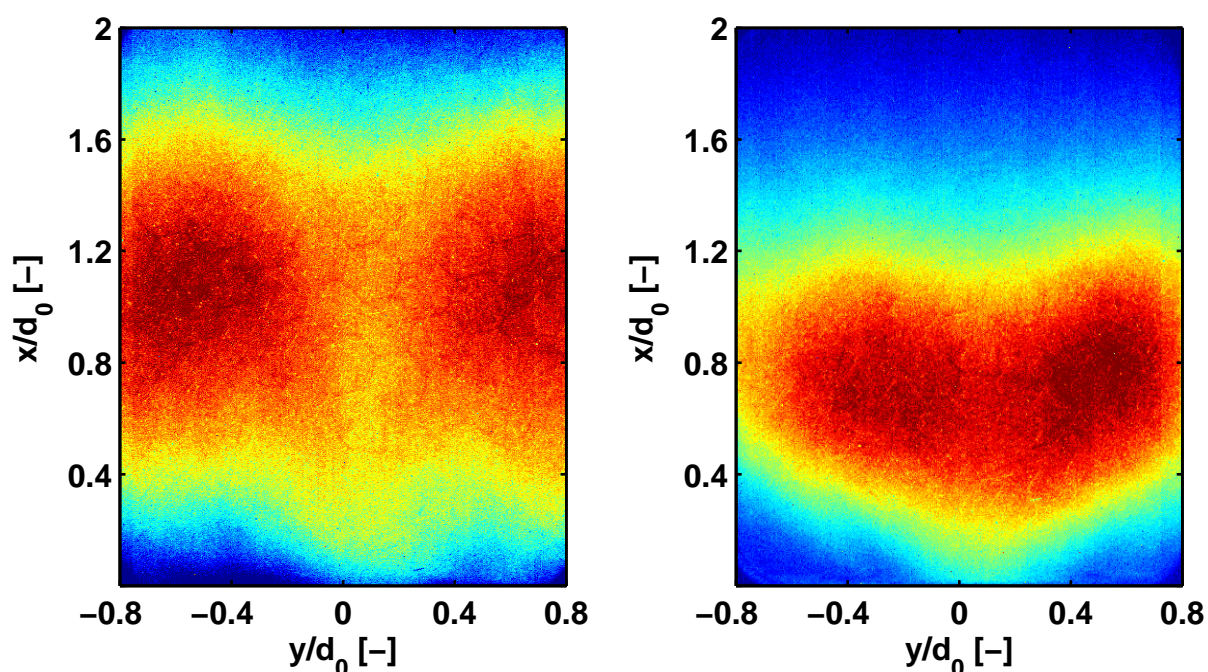


Figure 8.22: Left: time averaged distribution of the OH*-Chemiluminescence in the PPM. Right: time averaged distribution of the OH*-Chemiluminescence in the IPM

The interaction coefficient n is larger for the IPM ($n = 2.6$) than for the PPM ($n = 2.2$). This agrees qualitatively with the measurements as stable operation was achieved in the IPM at a higher equivalence ratio (Tabs. 8.3 and 8.5). A quantitative check of the absolute value of the interaction index n in both cases is given in Chapter 6.3.3. The theoretical value of n can be calculated with Eqn. 6.20, where the correction factor n_c is defined in Eqns. 6.21 and 6.22. Hereby, the ratio τ_{max}/τ has been approximated with the ratio L_f/X_{OHmax}

where L_f is the flame length and X_{OHmax} is the axial position of the maximum OH*-Chemiluminescence. The relation between these two parameters has been approximated by Wäsle [62] as

$$L_f \approx 1.5 \cdot X_{OH} \quad (8.2)$$

for single swirl stabilised premixed flames. If the determination of the X_{OHmax} is straight forward, for the flame length L_f the procedure is less accurate as it relies on the OH* intensity dropping under a certain arbitrary defined level. In the case of the annular combustor in the PPM, where the OH*-chemiluminescence exhibits a much flatter distribution (see Fig. 8.21 right, blue curve), X_{OH} lies at $0.98d_0$ and L_f has been approximated to $1.62d_0$. Therefore, the relation between X_{OH} and L_f writes

$$L_f \approx 1.65 \cdot X_{OH} \quad (8.3)$$

for the case presented in Fig. 8.21. This is slightly larger than in Eqn. 8.2. Hence, with having known the ratio L_f/X_{OHmax} for both cases, the factor n_c was evaluated for the PPM as well as IPM to be close to unity. This means that the values of the interaction index should be equal or close to the theoretical values. Indeed, when introducing the adiabatic flame temperature in Eqn. 6.20, a value of $n = 2.32$ for the PPM and $n = 2.75$ for the IPM were obtained. These are sensibly larger ($\approx 5\%$) than the values presented in Tab. 8.7. The adiabatic flame temperatures for the PPM and IPM were calculated with the correlation proposed by Peters [48], [47] for premixed methane flames and gave $T_{ad} = 1900\text{K}$ for the PPM and $T_{ad} = 2153\text{K}$ for the IPM, respectively.

With Eqn. 8.3, a maximum convective time delay of $\tau_{max} = 3.8\text{ms}$ was obtained for the PPM. This was plotted in Fig. 8.21 together with the standard deviation σ (magenta curve) for the PPM (Tab. 8.7). Fig. 8.21 left shows that the standard deviation σ lies almost within the range $[0, \tau_{max}]$ which, according to Eqn. 6.22, yields that the correction factor n_c should be close to unity.

8.3.4 Comparison of the BTM and FTF between SCC and ACC

The model based method described in Chapter 7 has been used in a similar manner to determine the dynamic characteristics of the EV5 burner and flame in the SCC. This work is presented in detail in [5]. Even if the topologies of the acoustic network models of the single and annular combustor test rigs differ due to the specific design, the dynamic characteristics of the burner and flame have been represented by the same analytical models. This represents a solid basis for comparing the results between the two combustion chamber configurations. The flame parameters determined in the SCC in the PPM are presented in Tab. 8.8 together with the corresponding results from the ACC. The operating points for the measurements in the two burner configurations have been set to be similar with respect to the preheating temperature, equivalence ratio ϕ and burner nominal velocity u_0 .

Table 8.8: Flame parameters and X_{OHmax} in the SCC and ACC for PPM

	Burner parameters		Flame parameters		X_{OHmax}/d_0 [mm]
	l_{eff} [m]	ζ [-]	τ [ms]	σ [ms]	
SCC	0.08	12	1.93	0.6	0.76
ACC	0.06	14	2.3	0.57	0.94

Tab. 8.8 shows that the l_{eff} of the interface burner-combustion chamber is larger in the SCC than in the ACC. As the geometry of the burner was the same in both test rigs, it can be concluded that this discrepancy is the effect of the larger area expansion (8%) in the ACC than in the SCC. The pressure loss coefficient ζ differs slightly between the two combustor configurations, being 14% larger in the ACC. The reference area for ζ is, in both cases, the upstream area of the burner A_b , which corresponds to the burner nominal diameter d_0 . According to the results of the pressure loss coefficient it can be concluded that the acoustic losses over the burner are similar in the two combustor configurations.

The comparison of the burner and flame parameters between the ACC and SCC, presented in Tab. 8.8, differs slightly from the previous results published

in [20]. The reason for these discrepancies is the improvement of the acoustic models of both ACC and SCC. Here, the interface plenum-burner, the burner element and the interface burner-combustion chamber were remodelled. The major improving effect came from the introduction of the area contraction element (Element 4, Fig. 7.2) between the plenum chamber and the burner section and the area expansion element with acoustic losses between the burner and the annular combustion chamber (Element 6, Fig. 7.2). Even though the modelling solutions were similar in both ACC and SCC, these considered the specific geometrical characteristics, i.e. different area contraction (interface plenum-burner) and expansions (interface burner-combustion chamber) in the ACC and SCC. After these changes were implemented, a major improvement was observed in the simulation results of the dynamic characteristics in cold isothermal conditions. Hence, the mean convective time delay τ is in the annular combustor slightly larger than in [20] whereas the standard deviation σ decreased. The new value of σ has more physical consistency as it represents 25% of τ whereas the value presented in [20] was 36%.

The mean convective time delay τ is in the ACC 16% larger than in the SCC. Concerning the normal distribution σ this represents 25% of τ in the ACC whereas in the SCC is 31%. A qualitative cross-check for the flame parameters is represented by the axial coordinate X_{OHmax} of the maximum OH*-Chemiluminescence. This is given for both, ACC and SCC in Tab. 8.8 and was determined from the time averaged OH*-Chemiluminescence distribution measured in stationary conditions which is presented in Fig. 8.23. Here, the intensity of the reaction zone is colour coded and ranges from blue for no reaction to dark red marking the areas with high reactivity. As the mean convective time delay τ is proportional to X_{OHmax} , according to

$$\tau \approx \frac{X_{OHmax}}{u_b}, \quad (8.4)$$

it can be expected that the X_{OHmax} is larger in the ACC than in the SCC. This assumption is confirmed in Fig. 8.23 which shows that the zones of highest reactivity (dark red) lie in the ACC (left) further downstream than in the SCC (right). Thus, the value of X_{OHmax} is 19% larger in the ACC (Tab. 8.8). The ratio

of X_{OHmax} is larger than the ratio of the mean convective time delays. This may be explained by the fact that the flow field characteristics downstream of the burner nozzle are different in the two combustion chambers with higher axial velocities in the ACC, which compensate the longer reaction zone.

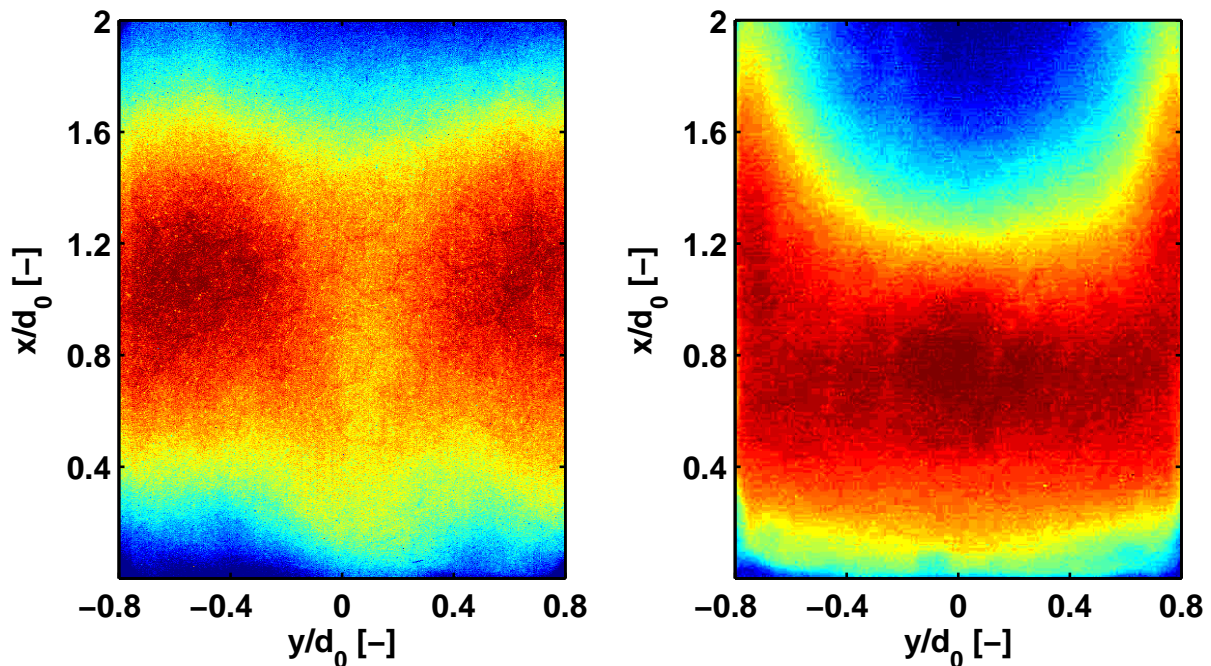


Figure 8.23: Time averaged OH^* -Chemiluminescence in the ACC (left) and SCC (right) without forcing in the PPM

Fig. 8.23 shows as well that a considerable discrepancy exists between the flame structures in the two burner configurations. In the ACC the main reaction zone is concentrated in two spots on either side of the central axis. In the SCC on the other side, the reaction zone indicates a wider expansion of the flame being visibly influenced by the surrounding walls of the combustor. To investigate the fluid dynamic effects, which cause the discrepancies in the stationary and dynamic flame behaviour, an extensive experimental investigation of the flow field characteristics in both ACC and SCC has been performed that is presented in Chapter 9.

8.4 Sensitivity Analysis of the Acoustic Network Model

The model based analysis of the experimental data presented in the previous chapters have been made through manual optimisation of the free model parameters in order to match the acoustic model computations with the measurement results for all modal components considered. In a first step, the free parameters of the burner model (l_{eff} , ζ) have been fixed by fitting the modal components calculated for the cold combustor to the correspondent experimental data measured in cold isothermal conditions. Then, the parameters of the flame model (n , τ , σ , τ_ϕ , σ_ϕ) have been determined as well by matching the simulation results for the axial and 1st order azimuthal components with the experimental data measured in the ACC with combustion. The similarity between simulation and experiment has been assessed based on the following qualitative and quantitative criteria:

- Identical eigenfrequencies for the modal components considered
- Similar modal amplitudes in the combustion chamber and plenum
- Comparable damping of the resonant acoustic modes

For a more effective matching of the simulation results with the experimental data, a sensitivity analysis of the acoustic model with respect to the variation of each free parameters was made for the axial and 1st order azimuthal components. The purpose of this was to assess quantitatively and qualitatively the influence of each parameter on the acoustic model simulations. The results of this study are presented for the PPM only. The range of variation was chosen between 0.6 and 1.6 of the optimal values given in Tab. 8.7. The results are presented in Figs. 8.24, 8.25, 8.26 and 8.27 for ζ , l_{eff} , τ and σ , respectively. The pressure loss coefficient ζ influences the acoustic damping in the burner and therefore has a direct effect on the amplitudes in the plenum with respect to the combustion chamber. Hence, the results of the sensitivity analysis for the variation of ζ are presented in Fig. 8.24 as relative amplitudes of the modal components in the plenum with respect to the combustion chamber. The variation of the parameters l_{eff} , τ and σ can be better visualised as spectra of

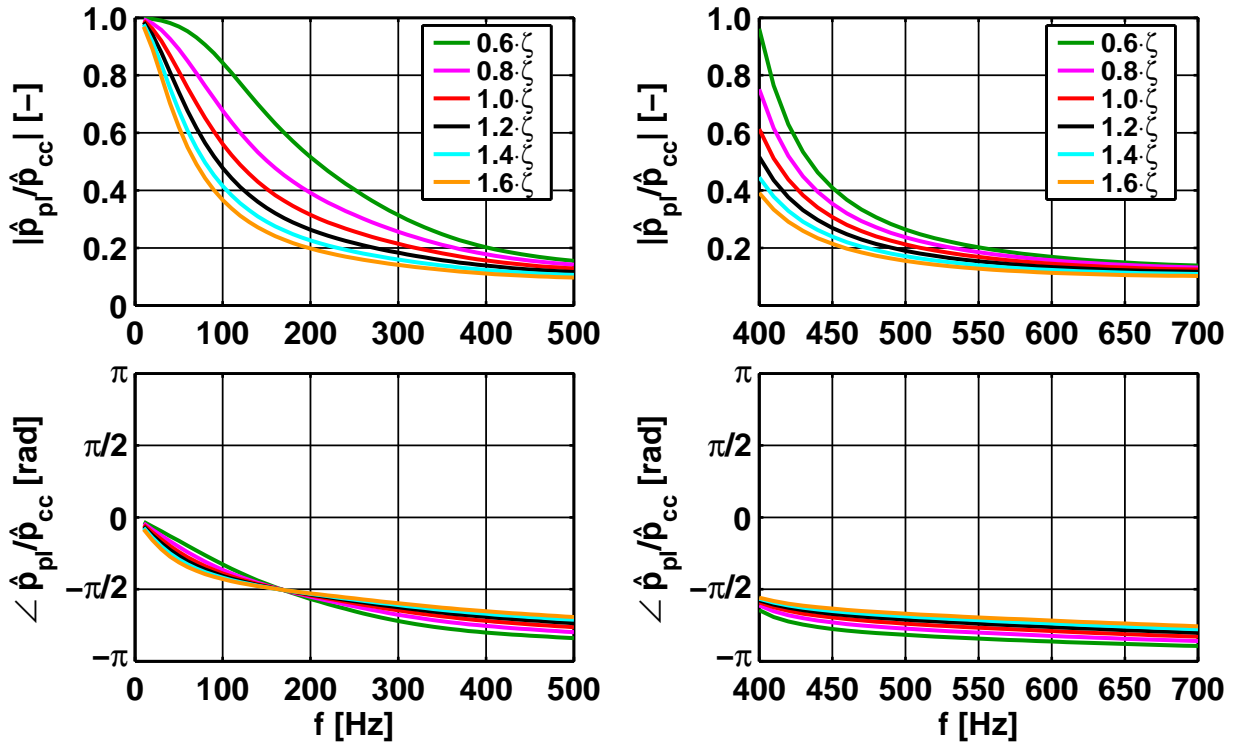


Figure 8.24: Simulation results for the axial (left) and 1st order azimuthal (right) components for the variation of the pressure loss coefficient ζ

the absolute acoustic pressure in the combustion chamber \hat{p}_{cc} . Therefore, the results of the acoustic model calculations, made with an arbitrary excitation level of the speaker element (Chapter 7.2) of 1 m/s, are presented for these parameters in Figs. 8.25, 8.26 and 8.27 as absolute values of the acoustic pressure in the combustion chamber \hat{p}_{cc} .

Fig. 8.24 shows clearly that the amplitude of the acoustic pressure upstream of the burner decreases steadily with higher values of ζ for both modal components, axial and 1st order azimuthal. With increasing the acoustic damping in the burner, the phase difference between the combustion chamber and plenum is becoming smaller. In the low frequency domain below 170 Hz though, the trend changes and the results do not depend on ζ .

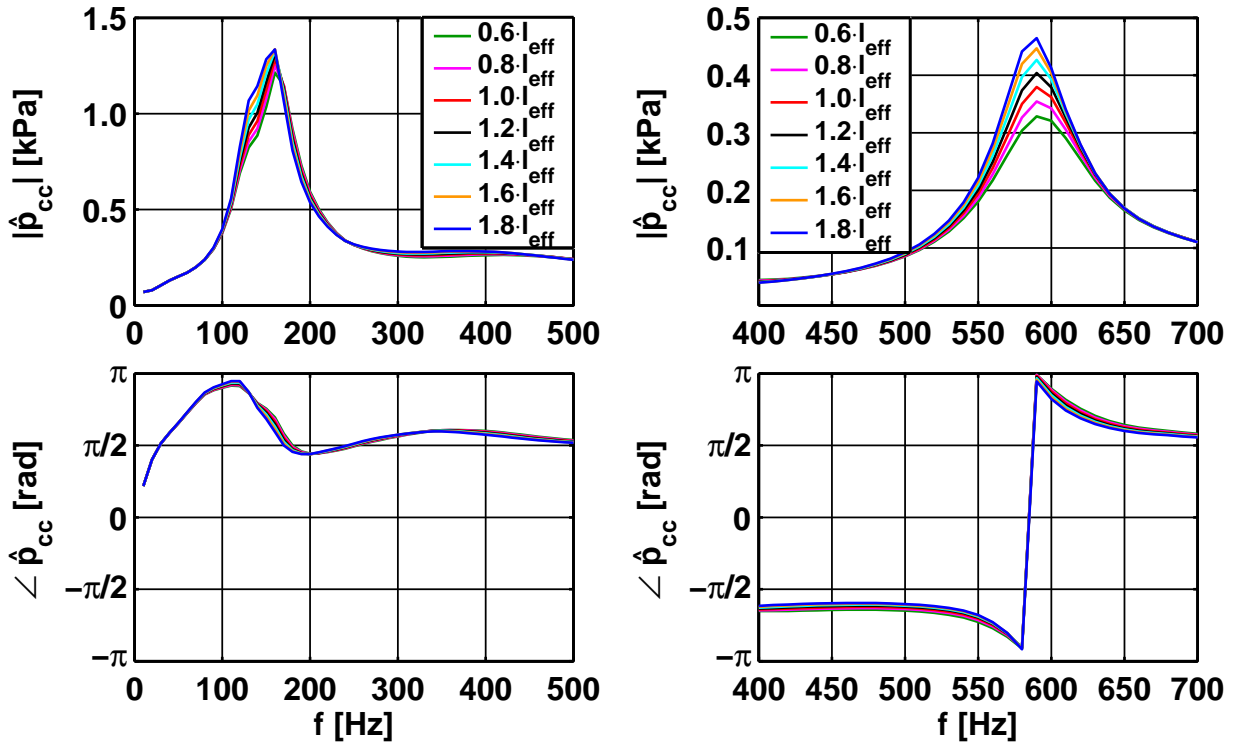


Figure 8.25: Simulation results for the axial (left) and 1st order azimuthal (right) components for the variation of the effective length l_{eff}

The parameter l_{eff} has an influence on the modal damping and eigenfrequencies. For the axial component, the increase of l_{eff} yields a rise of the amplitude especially in the resonance domain around 150 Hz (see Fig. 8.25). Simultaneously, a slight shift in the eigenfrequency towards lower values can be observed. For the 1st order azimuthal component, the variation of l_{eff} has a similar effect. The increase of l_{eff} yields a rise in the amplitude and the eigenfrequency shifts, as in the case of the axial component, slightly towards lower values.

The mean convective time delay τ influences significantly the eigenfrequencies of the system. For the axial component, the increase of τ over the optimal value shifts the eigenfrequency downwards whereas the decrease of τ has the effect of increasing the eigenfrequency. The variation of τ has been made keeping σ constant, which means that the acoustic damping decreased with

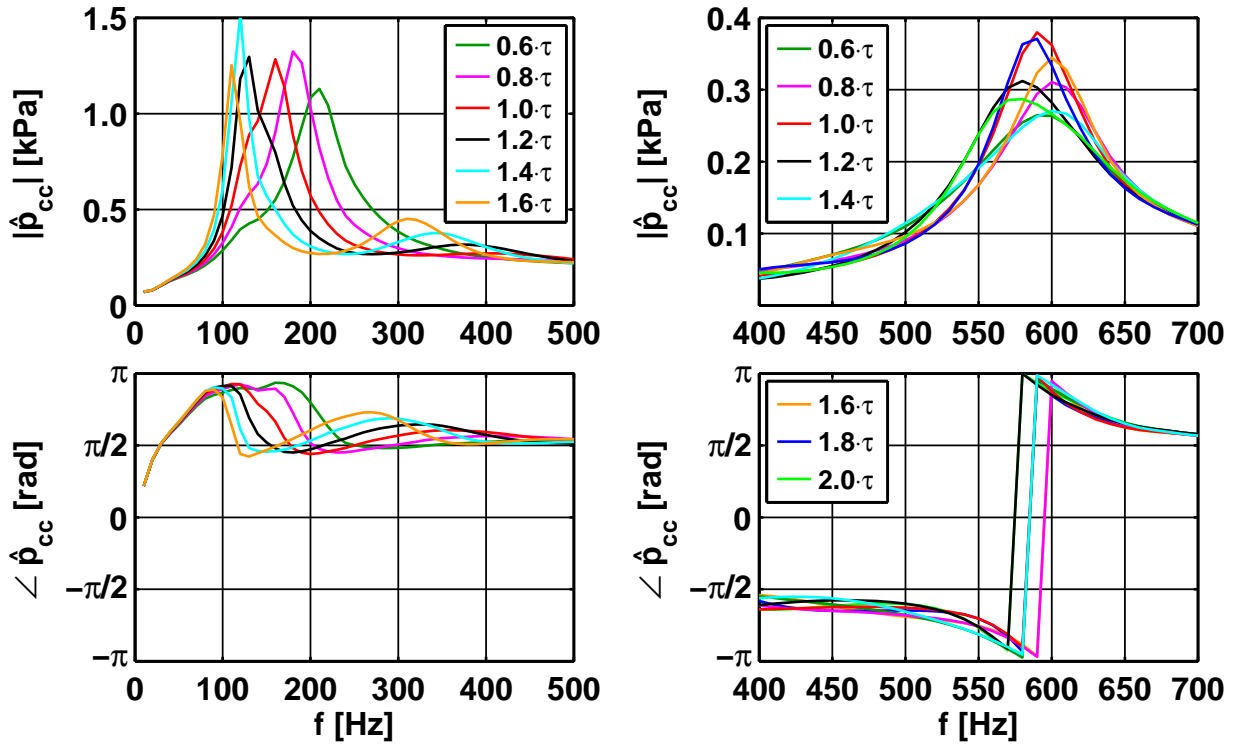


Figure 8.26: Simulation results for the axial (left) and 1st order azimuthal (right) components for the variation of the mean convective time delay τ

increasing τ . This can be seen in the much stronger resonance peaks for the higher values of τ ($1.4 \cdot \tau$, $1.6 \cdot \tau$) where, due to the lower damping, also the second axial eigenfrequency of the system rises around 300 Hz. For the optimal value of τ (red curve) the simulation does not exhibit resonance for the second axial mode, which was in agreement with the experimental results. In case of the 1st order azimuthal component, the variation of τ has a weaker effect. Here, the modal amplitude and the eigenfrequency change slightly in a narrow domain below 600 Hz.

The normal distribution σ influences only the modal damping and does not have a visible effect on the eigenfrequencies (see Fig. 8.27). For both, axial and the 1st order azimuthal components the increase of σ results in lower modal amplitudes.

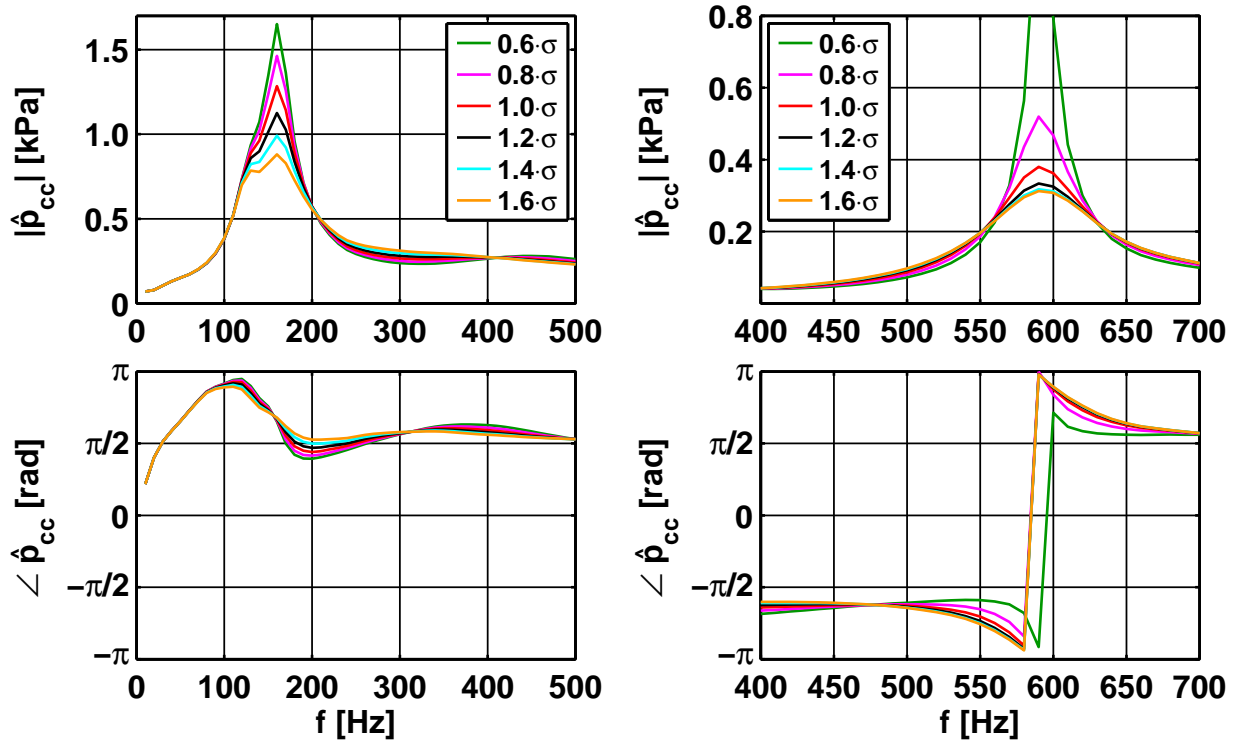


Figure 8.27: Simulation results for the axial (left) and 1st order azimuthal (right) components for the variation of the normal distribution σ

The results of the sensitivity analysis presented in this chapter show that the free model parameters influence significantly the acoustic model simulations and may have opposite effects on the modal components. Furthermore, the effect of the variation of the free model parameters is more pronounced in the resonance regime. In the rest of the frequency domain, the effect is much smaller or even insignificant. Consequently, for a more effective regression procedure of the free model parameters, including a least square fit, it would be more efficient to restrict the fitting region around the eigenfrequencies of the modal components considered.

9 Flow Field Investigations and Critical Confinement Theory

The flow field generated by the EV5 burner in the ACC and SCC has been investigated using PIV. The goal was to investigate, which effects cause the discrepancies in the FTF as well as in the static flame characteristics between the two combustor configurations (see Chapter 8). In the following, the experimental set-up for the PIV measurements is described. Then, the results for both ACC and SCC in cold isothermal conditions and for the ACC in the operation with flame are presented and discussed. In the last part of this chapter, a new theory is proposed, which explains the physical mechanism behind the different types of flow field in the ACC and SCC based on the confinement effect.

9.1 Experimental Set-up

The High-Speed PIV System consists of a ND-YAG double pulse laser unit with a wavelength of 532nm and a maximal repetition rate of 10kHz. The laser has been synchronised with a high speed camera equipped with a 85mm lens and an interference filter of wavelength $532 \text{ nm} \pm 20 \text{ nm}$. The sampling frequency of the PIV system has been set to 1000 Hz. The time delay between the laser pulses has been varied between 20 and $30 \mu\text{s}$ depending on the velocity range of the flow field to be resolved. Thereby, the energy of the laser pulses was approx. 10mJ for a time span of 180ns. The high sampling frequency of the PIV system has allowed the recording data within a short period of time before the windows get clogged with seeding particles. This aspect was a major advantage especially in the case of the annular combustor where the cleaning of the windows is relatively difficult.

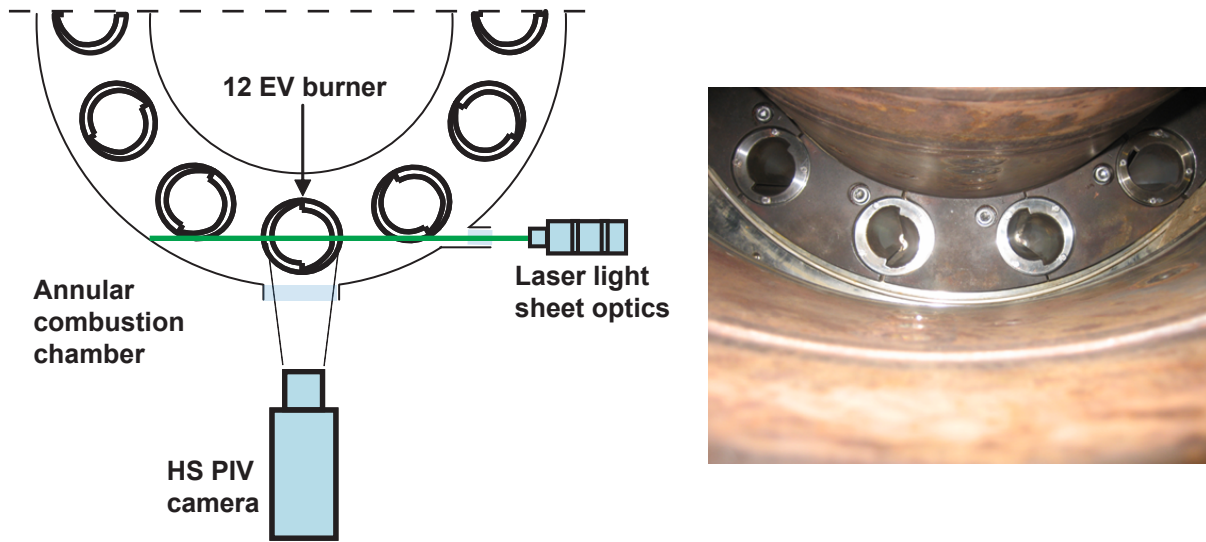


Figure 9.1: Schematic representation of the PIV set-up in the ACC

The PIV set-up in the ACC is presented schematically in Fig. 9.1. The laser sheet can be introduced in the combustion chamber with little diffraction losses through a specially designed adaptor mounted on the right window. The measurement plane cuts through the centre of the EV5 burner at 90° to the slot plane. Thus, the velocity data corresponds to the meridional section of one burner. The schematic representation of the PIV set-up in the SCC is presented in Fig. 9.2. The laser sheet enters the square $90 \times 90 \text{ mm}^2$ combustion chamber through specially designed slits mounted on the top wall and exits on the bottom side where a similar arrangement is provided. Hence, the light sheet cuts through the meridional plane of the EV5 burner at 90° to the slots.

The high speed camera was positioned, in both ACC and SCC, in front of the observation window at an angle of 90° with respect to the light sheet. The PIV set-up was completed with a TiO_2 seeding generator with the particle diameter of $5\text{-}10 \mu\text{m}$ as flow tracer. The post processing of the PIV data provides the 2D field of the instantaneous planar velocity components downstream of the burner exit. From this, the time averaged velocity fields were obtained and are presented in this section. A quantitative assessment of the averaged velocity fields has been made by calculating the mass balance of the isothermal flow

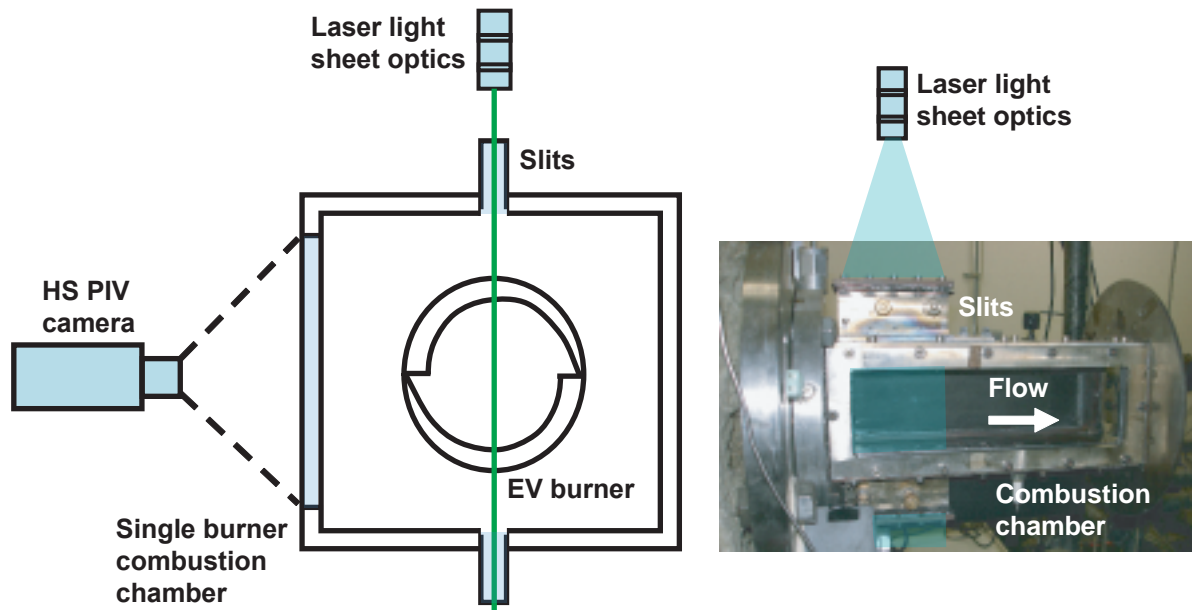


Figure 9.2: Schematic representation of the PIV set-up in the SCC

in both, SCC and ACC. In the ACC, the local integrals of the velocity profiles gave a mass flow rate within 98% of the metered value.

9.2 Results

The time averaged velocity fields for the cold isothermal conditions are presented in Figs. 9.3 and 9.4 for the ACC and SCC, respectively. Fig. 9.5 shows the time averaged velocity field in the ACC for the case with combustion (PPM). For the experiments presented here, the same pressure drop has been applied over the EV5 burner. The velocity field measurements with combustion have been performed in the ACC in atmospheric conditions (without exit nozzles) and without preheating. For this reason, the equivalence ratio is $\phi = 0.77$ much higher than in the preheated mode (Tab. 8.5) and corresponds to a thermal power of $P_{th} = 875\text{kW}$. On the left side of Figs. 9.3, 9.4 and 9.5 the axial velocity is plotted colour coded as fraction from the nominal burner velocity u_0 . This was calculated from the metered mass flow rate and the burner cross section A_b and is the same for all results presented. The local minima (min)

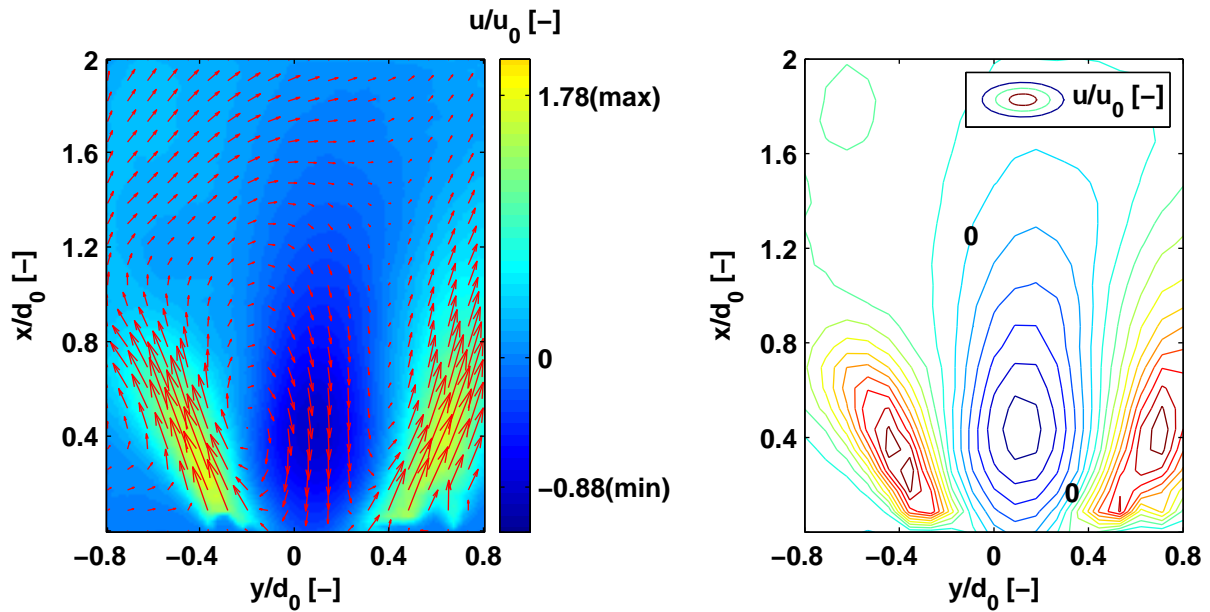


Figure 9.3: Time averaged absolute (arrows) and axial (colour) velocities in the ACC (left) for the isothermal flow. Right: contour plot of the axial velocity u with the isoline corresponding to the value zero

and maxima (max) are indicated on the legend of the colourmap plots. As expected, the maximum axial velocity corresponds to the measurements in the ACC with combustion ($1.96u_0$, Fig. 9.5). In the ACC with the cold flow, this is slightly lower ($1.78u_0$) and decreases even more in the SCC ($1.26u_0$). The right side of Figs. 9.3, 9.4 and 9.5 displays the contour plots of the axial velocity u . Here, the isoline corresponding to the value zero ($u = 0$) has been marked to illustrate the spatial extension of the IRZ.

As expected from OH^* -chemiluminescence (Fig. 8.23) as well as from the mean convective time delays in the PPM (Tab. 8.8), a large difference in the flow field is observed for the two burner configurations. Based on the findings presented recently by Fu et al. [24], the flow field in the ACC can be categorised in the *free jet regime* as it resembles the characteristics of a jet issuing into a quiescent environment. Here, a typical swirling flow with approx. 30° jet half angle and an IRZ of $0.5d_0$ width and $1.6d_0$ length can be seen. The inner recirculation axial velocity is about half the peak jet velocity which together

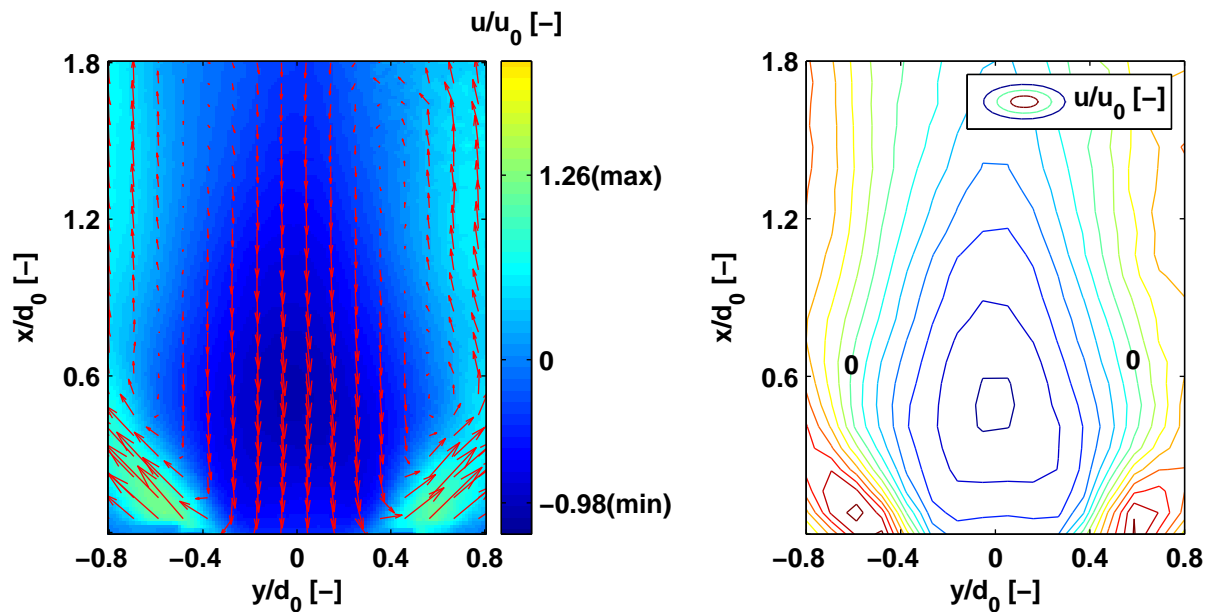


Figure 9.4: Time averaged absolute (arrows) and axial (colour) velocities in the SCC (left) for the isothermal flow. Right: contour plot of the axial velocity u with the isoline corresponding to the value zero

with the IRZ width results in about 15% recirculation rate that is common for this kind of flow. A slight asymmetry is seen in that the recirculation bubble and the jets are tilted to the right. Considering the swirl direction of the burners (see Fig. 9.1) and the induced azimuthal secondary flows in the annulus, which are clockwise at the inner and counter clockwise at the outer diameter of the annulus, this seems to indicate that the burner mid plane does not coincide with the zero velocity surface separating the inner and outer azimuthal secondary flow.

The flow field in the SCC, presented in Fig. 9.4, can be categorised in the *wall jet regime*. The swirling jet spreads quickly and high axial velocities are seen close to the combustor walls. For the same swirl number, the jet half angle is increased to 50° . The IRZ has a width of almost $0.8d_0$ and extends over $1.8d_0$, much higher than in the ACC. With this and with the fact that the backward axial velocities in the IRZ are increased, a recirculation almost double than in the ACC is achieved. The forward axial velocity has only 70% of the magnitude

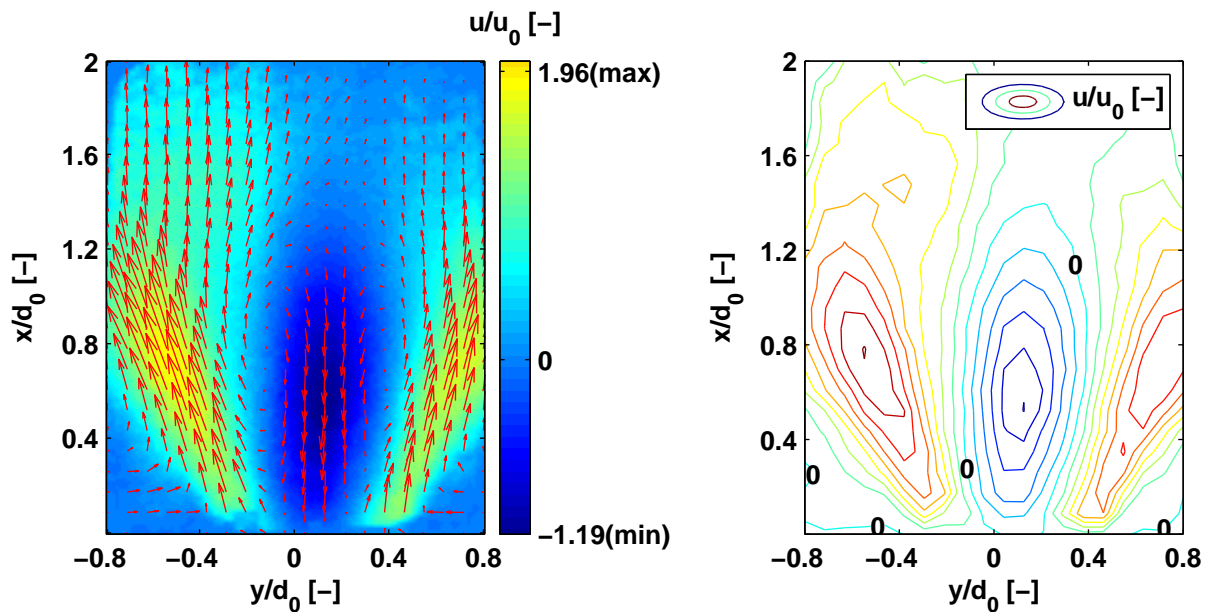


Figure 9.5: Time averaged absolute (arrows) and axial (colour) velocities in the ACC (left) for the case with combustion. Right: contour plot of the axial velocity u with the isoline corresponding to the value zero

of the ACC, which explains why the delay times given in Tab. 8.8 are quite similar in spite of the large difference in X_{OHmax} . Due to limitation of the window size in the SCC, the outer jet boundary could not be fully resolved.

Fig. 9.5 presents the flow field for the case with flame in the ACC. The air mass flow was kept the same as in the isothermal case (Fig. 9.3). The effect of volume expansion due to the heat input in the reaction zone can be recognized especially in the longer jet, stretching up to $1.3d_0$, whereas in the cold case it reaches only $0.9d_0$. However, the basic structure remains the same as in the isothermal case.

Summarizing the results of the flow field investigations, it can be stated that the different velocity profiles found in isothermal conditions in the two burner configurations, i.e. the *free jet regime* in the ACC and *wall jet regime* in the SCC, form a rather questionable basis for using in this case the dynamic flame data of the single burner flame for the analysis of the annular combustor.

9.3 Critical Confinement Theory

In the case of Fu et al. [24], the occurrence of either regime depended on the degree of confinement seen by the swirling jet, i.e. the area ratio between the burner exit and the combustion chamber. For the same burner and at fixed pressure drop and flow rate, Fu et al. found that the transition between the regimes took place at an area ratio of $A_{cc}/A_b = 5.88$. In the case presented here, where the area ratio between the combustion chamber and the burner is almost the same in the two configurations (1/12 of the ACC area is about 8% larger than the SCC area), the different flow regimes in the ACC and SCC are the result of the different properties of the confinement. In the ACC, the flames are only partially confined. This leads to burner-burner interactions, which generate substantial tangential secondary flows along the inner and outer combustor walls in the investigated co-swirling burner configuration. The interaction between the swirling flows of neighbouring burners in the ACC results in an exchange of angular momentum which, in the co-swirling arrangement, yields that the recirculated flow in the ORZ will carry less angular momentum than the burner flow. Hence, the angular momentum returned by the entrained flow is lower and reduces the swirl velocity of the swirling jet. Consequently, the centrifugal force which pulls the jet outwards is reduced. In contrast to this, in the SCC, where the jet is completely confined, the angular momentum of the recirculated flow in the ORZ is preserved. Thus, the entrained flow returns angular momentum, such that the decrease of swirl velocity due to entrainment will be considerably smaller. Therefore, the centrifugal force driving the jet flow outwards will be preserved longer, extending the jet core region. If the combustor diameter in the SCC is large enough such that the negative axial velocities associated with the ORZ are small, the axial pressure gradient needed to drive them is also small. In this case the swirling jet flow development, e.g. its expansion angle is dominated by the balance of inertia [27]. If the cross section area of the SCC is decreased, the recirculation velocities in the ORZ and the associated axial pressure gradient rise until at the critical confinement the jet angle increases significantly. Now the jet touches the combustor wall and effectively blocks recirculation from downstream. The inertia associated with the increased jet angle balances the axial pressure gra-

dient caused by entrainment flow and the new force balance creates the wall jet regime. A model which describes the decrease of the angular momentum of the recirculated flow in the ORZ as a result of the burner-burner interaction in the ACC was presented in [20] and will be given further in this chapter.

According to the model proposed in [21], the transition between the two flow regimes corresponds to a critical ratio between the specific axial momentum of the burner flow (u_0^2) and the specific axial momentum of the recirculated flow (u_r^2) in the ORZ

$$\left(\frac{u_0^2}{u_r^2}\right)_{\text{crit}} = \left(\frac{\dot{m}_0}{\dot{m}_r} \cdot \frac{A_{cc}}{A_b}\right)^2 \quad (9.1)$$

where the burner flow \dot{m}_0 and the recirculated flow \dot{m}_r have the same temperature ($T_0 = T_r$, $\rho_0 = \rho_r$). Eqn. 9.1 can be rearranged to get the critical area ratio as

$$\left(\frac{A_{cc}}{A_b}\right)_{\text{crit}} = C_{\text{crit}} \cdot \frac{\dot{m}_r}{\dot{m}_0} \quad (9.2)$$

where C_{crit} is the model constant. In Eqn. 9.2 \dot{m}_r is the recirculated mass flow defined as

$$\dot{m}_r = \dot{m}_x - \dot{m}_0 \quad (9.3)$$

where \dot{m}_x is the total mass flow of the swirling jet. An estimate for \dot{m}_x was obtained from the work of Meier [39] as

$$\frac{\dot{m}_x}{\dot{m}_0} = \left(0.32 \frac{x}{d_0} + 4.4 S_{\text{eff}}\right) \quad (9.4)$$

where S_{eff} is the effective swirl number. Eqn. 9.4 applies at axial positions downstream from the jet core region where, according to Meier, the mass flow entrained increases linearly with the axial coordinate. In the following, the re-

circulated mass flow will be calculated with Eqn. 9.4 at an axial position given by

$$\frac{x_m}{d_0} = 10 \cdot \exp(-0.3 S_{\text{eff}}) \quad (9.5)$$

which describes the axial extension of jet core as a function of the effective swirl number. When combining Eqs. 9.2, 9.3 and 9.4, the relation for the critical area ratio as a function of the effective swirl number S_{eff} is obtained:

$$\left(\frac{A_{cc}}{A_b}\right)_{\text{crit}} = C_{\text{crit}} \cdot \left(0.32 \frac{x_m}{d_0} + 4.4 S_{\text{eff}} - 1\right) \quad (9.6)$$

In Eqn. 9.6 the value of the model constant has been determined as $C_{\text{crit}} = 1.56$ by using the effective swirl number and the critical area ratio from the work of Fu et al. ($S_{\text{eff}} = 0.45$ and $(A_{cc}/A_b)_{\text{crit}} = 5.88$). The model from Eqn. 9.6 describing the critical area ratio as a function of the effective swirl number S_{eff} has been plotted in Fig. 9.7 together with the data from Fu et al. [24] (S_{eff} , $(A_{cc}/A_b)_{\text{crit}}$). Additionally, the data from Thring and Newby [59] for axial non-swirling jets ($S_{\text{eff}} = 0$) have been plotted and it can be seen that these correspond very well with the proposed theory.

To apply the proposed theory for a particular burner in order to analyse the flow regime in a single and an annular configuration requires to plot both configurations in Fig. 9.7. In [21] it was proposed that the critical area ratio of a particular combustor configuration scales with the entrainment mass flow rate of the swirling jet. Hence, the swirl number of the the recirculation flow S_r must be determined. A model for this has been proposed in [21] as

$$S_r = S_{\text{eff}} \frac{s_r}{s_0} \quad (9.7)$$

where s_r/s_0 is the ratio of the specific angular momentum of the recirculated flow to the burner flow, respectively. A quantitative assessment of this ratio has been derived based on the interaction between the co-swirling jets from

two neighbouring burners in an annular configuration. This is represented schematically in Fig. 9.6.

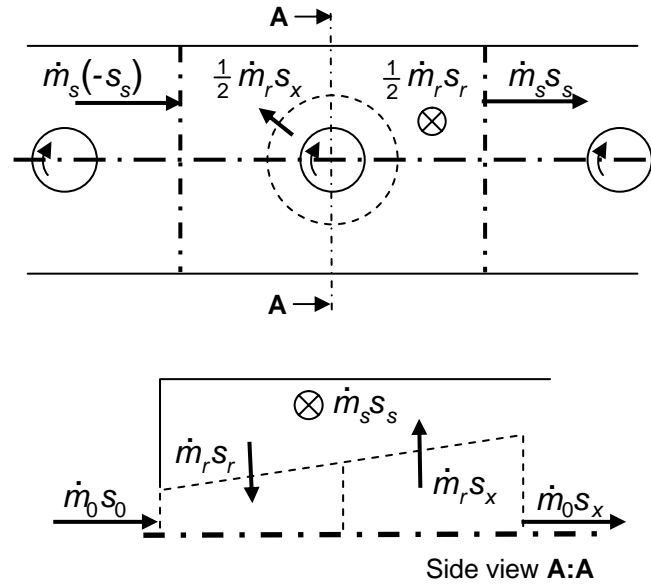


Figure 9.6: Schematic of jet swirl balance

The upper half of Fig. 9.6 shows a schematic view of the front panel of the ACC from downstream whereas the lower half presents a longitudinal cut which includes the burner axis. In the lower half of Fig. 9.6, the angular momentum flux of the burner flow $\dot{m}_0 s_0$ enters the control volume marked with dashed line. The jet expansion in the combustion chamber forms the ORZ and thereby the momentum flux $\dot{m}_r s_x$ of the swirling jet is transferred to the recirculated flow in the ORZ. Through entrainment, the angular momentum flux of the recirculated flow $\dot{m}_r s_r$ is returned to the swirling jet. Downstream of the burner near field, the angular momentum flux $\dot{m}_0 s_x$ of the swirling jet leaves the control volume. The balance of the angular momentum flux writes:

$$\dot{m}_0 s_0 + \dot{m}_r s_r - (\dot{m}_0 + \dot{m}_r) s_x = 0 \quad (9.8)$$

In case of a co-swirling burner arrangement, where the recirculated flow inter-

acts with the swirling flow of the neighbouring burner and with the side flow along the circumference, the angular momentum of the recirculation s_r becomes lower than the angular momentum of the burner flow s_0 . The balance of the angular momentum flux can be deduced from the scheme presented in the upper half of Fig. 9.6, which includes the effect of the side flow for the jet considered. Here, the assumption is made that the variation of the angular momentum of the swirling jet s_x along the x axis is linear, which yields that $s_s = 0.5(s_r + s_x)$. If only the upper half of the annular ring is considered, the balance of the angular momentum flux writes:

$$-\dot{m}_s \cdot \frac{1}{2}(s_r + s_x) + \frac{1}{2}\dot{m}_r s_x - \dot{m}_s \cdot \frac{1}{2}(s_r + s_x) - \frac{1}{2}\dot{m}_r s_r = 0 \quad (9.9)$$

where s_s is the specific angular momentum of the side flow along the circumference. The minus sign of the first term in Eqn. 9.9 indicates that the jets from the burner considered and from the burner lying to the left interact in opposite swirl directions [21]. By eliminating s_x and solving after the specific angular momentum of the recirculated flow s_r yields:

$$s_r = \frac{s_0(1 - 2\frac{\dot{m}_s}{\dot{m}_r})}{1 + 2\frac{\dot{m}_s}{\dot{m}_r} + 4\frac{\dot{m}_s}{\dot{m}_0}} \quad (9.10)$$

The model presented in Eqn. 9.10 shows that in the case of the SCC where the side flow is zero ($\dot{m}_s = 0$) the specific angular momentum of the entrained flow s_r equals the specific angular momentum of the burner flow s_0 and consequently, the entrained flow has the same swirl number as the burner ($S_r = S_{\text{eff}}$). In the case of the ACC with a co-swirling burner arrangement, where the side flow is non-zero, the specific angular momentum of the entrained flow s_r is smaller and therefore the swirl number of the entrained flow S_r is smaller than the swirl number of the burner flow S_{eff} . For a quantitative assessment of Eqn. 9.10, the mass flow rates of the side and entrainment flows need to be known. As presented above, the entrained mass flow can be determined with Eqn. 9.4 [39]. An estimate for the side mass flow rates was given in Eqn. 9.11 [21].

$$\dot{m}_s \approx 0.28 \cdot \left(\frac{A_{cc}}{A_b} \right)^{0.5} \cdot S_{eff} \cdot \dot{m}_0 \quad (9.11)$$

With this model, the values for the EV5 burner corresponding to the ACC and SCC have been determined and plotted in Fig. 9.7. The data point corresponding to the SCC lies well within the wall jet regime. For the ACC, where the estimated swirl number S_r of the entrainment is much lower, the flow moves into the free jet regime. These findings are in very good agreement with the experimental results presented before (see Figs 9.3 and 9.4).

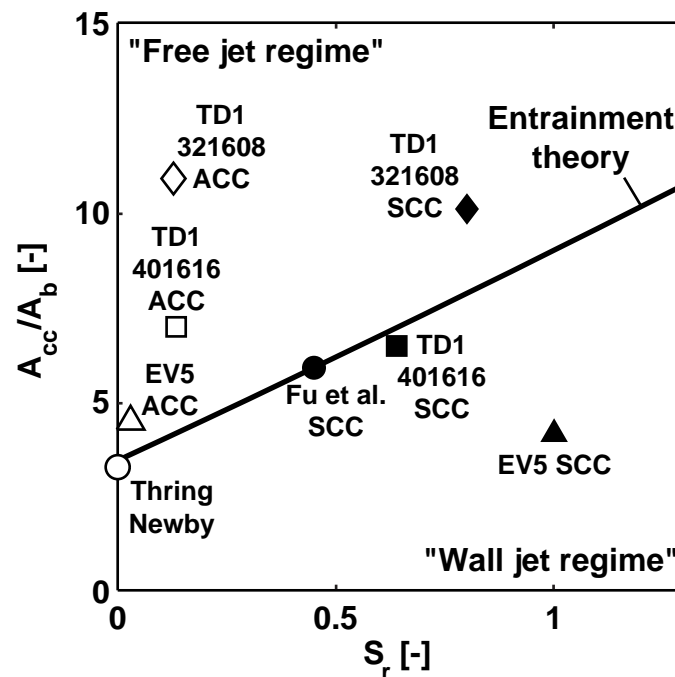


Figure 9.7: Comparison of confinement theory with experimental data from various burner configurations in the SCC and ACC

After the EV5, the ACC was equipped with the TD1 burner for doing optical flame characterisations with the method described in Chapter 4.3.2. The TD1 is a generic swirl stabilised burner with central flame holder (lance) developed at Lehrstuhl für Thermodynamik of TU München. Its modular configuration allows the variation of the parameters swirl number and nozzle diameter. The burner configuration is encoded in the notation "xxyyzz" where "xx" denotes

the diameter of the exit nozzle and "yy" the length of the swirler slot indicating the swirl strength. The part "zz" is the diameter of the flame holder (lance). A schematic representation of the burner is presented in [5]. The configurations TD1-401616 and TD1-321608 were investigated in the ACC and SCC. The first configuration was predicted to be in the wall jet regime in the SCC and free jet regime in the ACC. The configuration TD1-321608, which has a lower nozzle diameter and thereby a higher effective area ratio $(A_{cc}/A_b)_{eff}$, was predicted to be in the free jet regime in both SCC and ACC. Thus, for the configuration TD1-321608 similar flame geometries are expected. This is confirmed by Fig. 9.8 which presents the time averaged OH^* -Chemiluminescence distribution for the TD1-321608 burner in the PPM in the ACC (left) and SCC (right). Here, the flame structures are almost identical and the regions of highest reactivity (colour coded dark red) lie in both cases at approximately the same axial position.

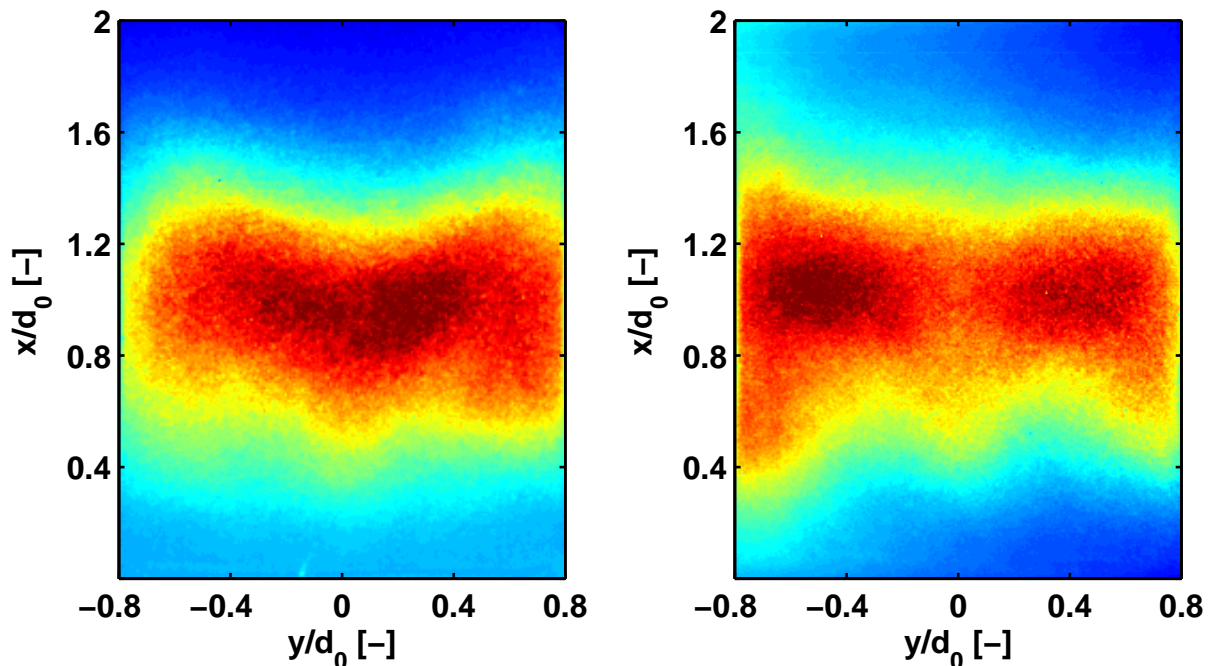


Figure 9.8: Time averaged OH^* -Chemiluminescence distribution with the TD1-321608 burner in the PPM in the ACC (left) and SCC (right)

9.4 Conclusions

The different flow field characteristics of the EV5 burner in the ACC and SCC do not allow the transfer of the dynamic characteristics of the flame between the two combustor configurations. To achieve this, similar flow regimes in both cases must exist. With the theory proposed in [21], it is possible to estimate the flow regime on the basis of the area ratio between the combustion chamber and the burner, the operating temperature and the burner swirl number. In a much wider sense, this theory can be used in the so called "predictive mode". Here, the single burner experiments can be designed with respect to choosing a proper area ratio such that the flow regime is similar to the multi burner annular configuration.

10 Summary

The BTM and FTF of a swirl stabilised premixed burner have been measured successfully in an annular combustor. In this context a new method called *model based method* has been developed, which is a combination of acoustic network theory and experimental investigations. The main advantage of the new method is that it allows the determination of the BTM and FTF with less dynamic pressure sensors than the classical approaches, which rely only on experiments. Hence, the *model based method* reduces considerably the experimental effort and the cost for the measurement technique.

In the acoustic model of the annular combustor, the burner has been modelled analytically as a compact element with losses and the flame as a classical $(n-\tau)$ formulation with a spatially distributed reaction zone. The analytical models of the burner and flame have a set of free parameters, which have been determined through regression on the experimental data. The good agreement between the model computations and the experimental data has shown that the acoustic model is able to simulate the 2D acoustics of the annular combustor for both PPM and IPM. Hence, the classical $(n-\tau)$ formulation, which is an "axial" FTF, expressing the heat release fluctuation of the flame as a result of the acoustic velocity fluctuation in the burner, is adequate for describing the dynamic flame characteristics in an annular combustor with axial and azimuthal modes. As a limitation though, the *model based method* can be used only when the 2D acoustic field of the annular combustor is characterised by azimuthal modes with a predominantly standing character. Experimental results have shown that this condition was fulfilled in the work presented here. The case when the azimuthal modes exhibit a pronounced spinning character cannot be investigated. Therefore, an important aspect to be considered for further development of this method is the extension to include also spinning azimuthal modes.

The BTM and FTF determined in the ACC have been compared with the results obtained in the SCC for the same operating conditions. This was made to check the transferability of the burner and flame dynamic characteristics between the two combustor configurations. The parameters ζ and l_{eff} of the burner model are similar and thus, it can be concluded that the BTM is the same in the ACC and SCC. In case of the flame model in the PPM, the results have shown discrepancies. Here, the mean convective time delay is larger in the ACC than in the SCC. This finding was in agreement with the results of the static flame characterisations, which showed that the zones with the highest reactivity, determined as the axial position where the measured OH*-chemiluminescence distribution is maximum, were in the ACC further downstream than in the SCC.

In addition, an extensive experimental investigation of the flow field characteristics of the EV5 burner has been performed with using PIV. This work was aiming to identify the aerodynamic effects which cause the discrepancies in the FTFs. The results have shown significant differences of the flow field in the two combustor configurations. In the ACC, the burner flow has exhibited a free jet regime whereas in the SCC a wall jet regime could be seen. The different flow regimes were responsible for the deviations in the FTF and thus, represented a improper basis for the transferability of the FTF results between the ACC and SCC. The wall jet regime in the SCC is an effect of the confinement, i.e. the burner flow is enclosed from all four sides. The transition from the free jet to the wall jet regime occurs at a critical ratio between the cross-sections of the burner and the combustion chamber. In the ACC, due to the missing side walls in transversal direction, this effect does not occur and consequently, the flow is in the free jet regime. After the physical mechanism was explained a new correlation was proposed which serves to estimate the critical confinement where the transition between the flow regimes occurs in SCC. This new theory allows to design single burner experiments such that the aerodynamic similarity with the multi burner configuration is achieved. For the conical premixed burner investigated in this work, the analysis made with the new theory has given that a single burner test rig with a larger cross-section of the combustion chamber is required for achieving flow structures and dynamics that are representative for annular configurations.

Bibliography

- [1] M. Abom. Modal decomposition in ducts based on the transfer function measurements between microphone pairs. *Journal of Sound and Vibration*, Vol. 135(1):95–114, 1989.
- [2] M. Abom. Measurement of the scattering matrix of acoustical two ports. *Mechanical Systems and Signal Processing*, Vol. 5(2):89–104, 1991.
- [3] M. Abom. A note on the experimental determination of acoustical two-port matrices. *Journal of Sound and Vibration*, Vol. 3:185–188, 1992.
- [4] S. Akamatsu and A. Dowling. Three dimensional thermoacoustic oscillation in a premix combustor. 2001-GT-0034 in Proc. of ASME Turbo Expo 2001 Power for Land, Sea and Air, New Orleans, Louisiana, USA, 2001.
- [5] P. R. Alemela. Measurement and Scaling of Acoustic Transfer Matrices of Premixed Swirl Flames. PhD thesis, TU München, 2009.
- [6] P. R. Alemela, D. Fanaca, F. Ettner, C. Hirsch, T. Sattelmayer, and B. Schuermans. Flame transfer matrices of a premixed flame and a global check with modelling and experiments. GT2008-50111 in Proc. of ASME Turbo Expo 2008 Power for Land, Sea and Air, Berlin, Germany, 2008.
- [7] M. P. Auer. Einfluss fluktuierender Brennstoff- und Luftmassenströme auf die Dynamik einer Drallflamme. PhD thesis, TU München, 2005.
- [8] H. Büchner. Experimentelle und theoretische Untersuchungen der Entstehungsmechanismen selbsterregten Druckschwingungen in technischen Vormisch-Verbrennungssystemen. PhD thesis, Universität Karlsruhe (TH), 1992.

- [9] V. Bellucci, D. Nowak, W. Geng, and C. Steinbach. Using thermoacoustic analysis for robust burner design. GT2007-27329 in Proc. of ASME Turbo Expo 2007 Power for Land, Sea and Air, Montreal, Canada, 2007.
- [10] V. Bellucci, C. O. Paschereit, P. Flohr, and F. Magni. On the use of Helmholtz resonators for damping acoustic pulsations in industrial gas turbines. 2001-GT-0039 in Proc. of ASME Turbo Expo 2001 Power for Land, Sea and Air, New Orleans, Louisiana, USA, 2001.
- [11] V. Bellucci, B. Schuermans, D. Nowak, P. Flohr, and C. O. Paschereit. Thermoacoustic modeling of a gas turbine combustor equipped with acoustic dampers. GT2004-53977 in Proc. of ASME Turbo Expo 2004 Power for Land, Sea and Air, Vienna, Austria, 2004.
- [12] P. Berenbrink and S. Hoffmann. Suppression of dynamic combustion instabilities by passive and active means. 2000-GT-0079 in Proc. of ASME Turbo Expo 2000 Power for Land, Sea and Air, Munich, Germany, 2000.
- [13] B. T. Chu. On the generation of pressure waves at a plane flame front. *4th Symp (Int.) on Combustion*, 1953.
- [14] L. Crocco and S. Cheng. Theory of combustion instability in liquid propellant rocket motors. Butterworths Science Publication, note: AGARDOGRAPH N 8, 1956.
- [15] K. Döbbeling, J. Hellat, and H. Koch. 25 years of BBC/ABB/Alstom lean premix combustion technologies. GT2005-68269 in Proc. of ASME Turbo Expo 2005 Power for Land, Sea and Air, Reno-Tahoe, Nevada, USA, 2005.
- [16] F. Ettner. Analysis of the acoustic field in an annular combustor. Master's thesis, TD, TU München, 2007.
- [17] S. Evesque. Modelling of combustion instabilities in annular combustors. Technical Report ENK5-CT2001-50032, TU München, July 2003.
- [18] S. Evesque and W. Polifke. Low-order acoustic modelling for annular combustors: Validation and inclusion of modal coupling. GT-2002-30064 in Proc. of ASME Turbo Expo 2002 Power for Land, Sea and Air, Amsterdam, The Netherlands, 2002.

- [19] S. Evesque, W. Polifke, and C. Pankiewitz. Spinning and azimuthally standing acoustic modes in annular combustors. AIAA 2003-3182 in 9th AIAA/CEAS Aeroacoustics Conference and Exhibit, Hilton Head, SC, 2003. AIAA.
- [20] D. Fanaca, P. R. Alemela, F. Ettner, C. Hirsch, T. Sattelmayer, and B. Schuermans. Determination and comparison of the dynamic characteristics of a perfectly premixed flame in both single and annular combustion chambers. GT2008-50781 in Proc. of ASME Turbo Expo 2008 Power for Land, Sea and Air, Berlin, Germany, 2008.
- [21] D. Fanaca, P. R. Alemela, C. Hirsch, T. Sattelmayer, and B. Schuermans. Comparison of the flow field of a swirl stabilised premixed burner in an annular and a single burner combustion chamber. GT2009-59884 in Proc. of ASME Turbo Expo 2009 Power for Land, Sea and Air, Orlando, Florida, USA, 2009.
- [22] A. Fischer. Hybride, thermoakustische Charakterisierung von Drallbrennern. PhD thesis, TU München, 2004.
- [23] E. Freitag, H. Konle, M. Lauer, C. Hirsch, and T. Sattelmayer. Pressure influence on the flame transfer function of a premixed swirling flame. GT2006-90540 in Proc. of ASME Turbo Expo 2008 Power for Land, Sea and Air, Barcelona, Spain, 2006.
- [24] Y. Fu, J. Cai, S. M. Jeng, and H. Mongia. Confinement effects on the swirling flow of a counter-rotating swirl cup. GT2005-68622 in Proc. of ASME Turbo Expo 2005 Power for Land, Sea and Air, Reno-Tahoe, Nevada, USA, 2005.
- [25] A. Gentemann, A. Fischer, S. Evesque, and W. Polifke. Acoustic transfer matrix reconstruction and analysis for ducts with sudden change of area. AIAA-2003-3142 in 9th AIAA/CEAS Aeroacoustics Conference and Exhibit, Hilton Head, SC, USA, May 12-14 2003.
- [26] L. C. Haber, U. Vandsburger, W. R. Saunders, and V. K. Khanna. An examination of the relationship between chemiluminescent light emissions and heat release rate under non-adiabatic conditions. 2000-GT-0121 in

- Proc. of ASME Turbo Expo 2000 Power for Land, Sea and Air, Munich, Germany, 2000.
- [27] C. Hirsch, D. Fanaca, P. R. Alemela, W. Polifke, and T. Sattelmayer. Influence of the swirler design on the flame transfer function of premixed flames. GT2005-68195 in Proc. of ASME Turbo Expo 2005 Power for Land, Sea and Air, Reno-Tahoe, Nevada, USA, 2005.
- [28] J. J. Keller. Thermoacoustic oscillations in combustion chambers of gas turbines. *AIAA Journal*, Vol. 33(12):2280–2287, 1995.
- [29] G. Kirchhoff. Ueber den einfluss der wärmeleitung in einem gase auf die schallbewegung. *Annalen der Physik und Chemie*, 1868.
- [30] J. Kopitz, A. Huber, T. Sattelmayer, and W. Polifke. Thermoacoustic stability analysis of an annular combustion chamber with acoustic low order modeling and validation against experiment. GT2005-68797 in Proc. of ASME Turbo Expo 2005 Power for Land, Sea and Air, Reno-Tahoe, Nevada, USA, 2005.
- [31] W. Krebs, P. Flohr, B. Prade, and S. Hoffmann. Thermoacoustic stability chart for high-intensity gas turbine combustion systems. *Combust. Sci. and Tech.*, Vol. 30:99–128, 2002.
- [32] U. Krüger, J. Hüren, S. Hoffmann, W. Krebs, P. Flohr, and D. Bohn. Prediction of thermoacoustic instabilities with focus on the dynamic flame behaviour for the 3A-series gas turbine of Siemens KWU. 99-GT-111 in Int. Gas Turbine & Aeroengine Congr. & Exh., Indianapolis, Indiana, 1999.
- [33] K. Kunze. Untersuchung des thermoakustischen Flammenübertragungsverhaltens in einer Ringbrennkammer. PhD thesis, TU München, 2004.
- [34] K. Kunze, C. Hirsch, and T. Sattelmayer. Transfer function measurements on a swirl stabilized premix burner in an annular combustion chamber. GT2004-53106 in Proc. of ASME Turbo Expo 2004 Power for Land, Sea and Air, Vienna, Austria, 2004.

- [35] T. Lieuwen and T. Zinn. Application of multipole expansions to sound generation from ducted unsteady combustion processes. *Journal of Sound and Vibration*, Vol. 10:405–414, 2000.
- [36] M. Lohrmann and H. Büchner. Scaling of stability limits in lean-premixed gas turbine combustors. GT2004-53710 in Proc. of ASME Turbo Expo 2004 Power for Land, Sea and Air, Vienna, Austria, 2004.
- [37] F. E. Marble and S. M. Candel. Acoustic disturbance from gas non-uniformities convected through a nozzle. *Journal of Sound and Vibration*, Vol. 55(2):225–243, 1977.
- [38] M. Mastrovito, S. M. Camporeale, A. Forte, and B. Fortunato. Analysis of pressure oscillations data in gas turbine annular combustion chamber equipped with passive damper. GT2005-69056 in Proc. of ASME Turbo Expo 2005 Power for Land, Sea and Air, Reno-Tahoe, Nevada, USA, 2005.
- [39] P. Meier. Untersuchung isothermer drallbehafteter freistrahlen. *Forschung im Ingenieurwesen*, Vol. 34(5):133–140, 1968.
- [40] M. L. Munjal. Acoustics of ducts and mufflers. New York: Wiley-Interscience, 1987.
- [41] M. L. Munjal and A. G. Doige. Theory of a two source-location method for direct experimental evaluation of the four-pole parameters of an aeroacoustic element. *Journal of Sound and Vibration*, Vol. 141(2):323–333, 1990.
- [42] H. Najm, P. Paul, C. Mueller, and P. Wycker. On the adequacy of certain experimental observables as measurements of flame burning rate. *Combustion and Flame*, Vol. 113:312–332, 1989.
- [43] C. Pankiewitz. Hybrides Berechnungsverfahren für thermoakustische Instabilitäten von Mehrbrennersysteme. PhD thesis, TU München, 2004.
- [44] C. Pankiewitz, S. Evesque, W. Polifke, and T. Sattelmayer. Stability analysis of annular gas turbine combustors. LECT Workshop on Instabilities in Aero-Engine Combustors, Stuttgart, Germany, Dec 4-5 2001.

- [45] C. O. Paschereit, B. Schuermans, W. Polifke, and O. Mattson. Measurement of transfer matrices and source terms of premixed flames. 99-GT-133 in Int. Gas Turbine & Aeroengine Congr. & Exh., Indianapolis, Indiana, 1999.
- [46] M. C. A. M. Peters, A. Hirschberg, A. J. Reijnen, and A. P. J. Wijnands. Damping and reflection coefficient measurements for an open pipe at low Mach and low Helmholtz numbers. *J. of Fluid Mech.*, Vol. 256:499–534, 1993.
- [47] N. Peters. Kinetic foundation of thermal flame theory. *American Institute of Aeronautics and Astronautics*, 1997. Institut of Technische Mechanik.
- [48] N. Peters. Turbulent Combustion. Cambridge University Press, 2000. ISBN 0-521-66082-3.
- [49] W. Polifke, J. Hoek, and B. Verhaar. Everything you always wanted to know about f and g. Technical report, ABB Switzerland, 1997.
- [50] W. Polifke, B. Verhaar, and K. Döbbeling. On thermo-acoustic stability analysis of gas turbines. Technical report, ABB Corporate Research, 1997.
- [51] L. Rayleigh. The explanation of certain acoustic phenomena. *Royal Institute Proc. III*, paper IS-153, 1878.
- [52] M. Sallikudin and R. Ramakrishnan. Acoustic power measurement for single and annular stream duct-nozzle systems utilizing a modal decomposition scheme. *Journal of Sound and Vibration*, Vol. 113(3):441–472, 1987.
- [53] T. Sattelmayer. Influence of the combustor aerodynamics on combustion instabilities from equivalence ratio fluctuations. 2000-GT-0082 in Proc. of ASME Turbo Expo 2000 Power for Land, Sea and Air, Munich, Germany, 2000.
- [54] T. Sattelmayer, J. Grünwald, and S. Steinbach. Wirbelmischer für SCR-verfahren im PKW. *MTZ* 1/2005:44-48, 2005.

- [55] B. Schuermans, V. Bellucci, F. Guethe, F. Meili, P. Flohr, and O. Paschereit. A detailed analysis of thermoacoustic interaction mechanisms in a turbulent premixed flame. GT2004-53831 in Proc. of ASME Turbo Expo 2004 Power for Land, Sea and Air, Vienna, Austria, 2004.
- [56] B. Schuermans, V. Bellucci, and C. O. Paschereit. Thermoacoustic modeling and control of multi burner combustion systems. GT2003-38688 in Proc. of ASME Turbo Expo 2003 Power for Land, Sea and Air, Atlanta, Georgia, USA, 2003.
- [57] B. Schuermans, W. Polifke, and C. O. Paschereit. Modeling transfer matrices of premixed flames and comparison with experimental results. 99-GT-132 in Int. Gas Turbine & Aeroengine Congress & Exhibition, Indianapolis, Indiana, USA, 1999.
- [58] S. R. Stow and A. P. Dowling. Thermoacoustic oscillations in an annular combustor. 2001-GT-0037 in Proc. of ASME Turbo Expo 2001 Power for Land, Sea and Air, New Orleans, Louisiana, 2001.
- [59] M. Thring and M. Newby. Combustion length of enclosed turbulent jet flames. *4th Symp (Int.) on Combustion, Baltimore*, 789-796, 1953.
- [60] C. W. S. To and A. G. Doige. A transient testing technique for the determination of matrix parameters of acoustic systems, I: Theory and principles. *Journal of Sound and Vibration*, Vol. 62(2):207–222, 1979.
- [61] C. W. S. To and A. G. Doige. A transient testing technique for the determination of matrix parameters of acoustic systems, II: Experimental procedures and results. *Journal of Sound and Vibration*, Vol. 62(2):223–233, 1979.
- [62] H. Wäsle. Vorhersage der Lärmemission turbulenter Vormischflammen. PhD thesis, TU München, 2008.